Cláudio Roberto Fernandes de Góis Cardoso

Eddies of the Cape Verde Archipelago

Universidade do Algarve

Faculdade de Ciências e Tecnologia

Faro, 2017

Cláudio Roberto Fernandes de Góis Cardoso

Eddies of the Cape Verde Archipelago

Master in Marine and Coastal Systems

Work performed under the supervision of:

Dr. Rui Caldeira

Dr. Paulo Relvas

Universidade do Algarve

Faculdade de Ciências e Tecnologia

Faro, 2017

Eddies of the Cape Verde Archipelago

Declaração de autoria de trabalho

Declaro ser o(a) autor(a) deste trabalho, que é original e inédito. Autores e trabalhos consultados estão devidamente citados no texto e constam da listagem de referências incluída.

_____

Cláudio Roberto Fernandes de Góis Cardoso

Copyright

Acknowledgments

It has been a long journey, which (contradictorily) passed by in a blink of an eye. This thesis was challenging in every way, academically and personally. Since the very beginning, several important decisions had to be made, but luckily for me, I had the support of one very important person, to whom I am greatly thankful. Alexandra Rosa, my life partner, you were always there even when at 933 km distance. This path was shared by both of us, because I know that these times weren't a walk in the park for you neither. To think that this thesis was hard only on me would be extremely selfish, and for all your support, your strength, your joy, and many more other things (the list is quite big), I thank you from all my heart.

To my family, you are the ones to whom I dedicate this work. Without your patience and your support for all my decisions, this would only be an "if". The truth is that every step and direction I took lead me here, and you always had my back. For that, I am internally thankful. An especial message to my mom, who gave me strength in all ways possible – even with a simple cup of tea when working in the middle of the night. Sometimes, every small gesture counts. To my father, who despite all things, always gave me company. To my brother, your wise words gave me serenity during stressful times. You had a different approach than mine when you were in my place, and it worked pretty well!

To my supervisors, I thank Dr. Rui Caldeira for the orientation, the motivation, the wise words and of course for the opportunity to study the Cape Verde Archipelago at the Oceanic Observatory of Madeira (OOM). To Dr. Paulo Relvas, who opened the first door of the project, many thanks for your revision, your comments, your attention and your good will.

To the staff of the OOM, many thanks for the insights (in colormaps and many other things!) and more importantly for the moments of laughter.

To Prof. Joaquim Luís for the insights in handling the Wind datasets, to Prof. Alexandra Cravo for the wise advises and to Prof. José Jacob for the good conversations.

Finally, to all my friends who always provided me kind words and motivation along the way, an especial thanks to Cátia Freitas, André Silva, Élvio Escórcio, Mauro Gama, Gustavo Vieira, Ricardo Correia, Rúben Gouveia and many others.

Abstract

The characterisation of the mesoscale eddy field within and around the Cape Verde Archipelago is presented. Special attention is regarded towards the far-field (incoming) and the near-field (island-induced) eddies, along with the mechanisms and processes influencing their generation and evolution. Consequent implications in the local biological primary production (Island Mass Effect, or IME) are also assessed. This is achieved by combining remote-sensing satellite observations for wind, ocean surface currents, ocean surface topography, clorophyll *a* surface concentrations and sea surface temperature. Results show that the interaction between far-field eddies and the archipelago is a recurrent phenomenon, which results in eddy transformation, eddy termination, eddy splitting, and eddy deflection. Local island-induced disturbances are also significant, mainly by atmospheric effects. Such processes result in the generation and confinement of mesoscale eddies, more often observed in the leeward group. However, the distinction between island-induced and far-field processes is hindered by the complex interaction between both fields. Thus, it is strongly suggested that many of the near-field eddies are a direct product or a by-product of such interaction. This is even more obvious in the assessment of the IME. Far-field eddies are often associated with enhanced Clh*a* concentrations. However, nutrient-injection by island-induced cyclonic eddies also gives rise to phytoplankton blooms. As the remote and island-driven biological enhancement are remarkably intertwined, such observations challenge the idea that local biological productivity in deep oceanic islands are exclusively driven by island-induced mechanisms.

Key Words: Cape Verde, Mesoscale Eddies, Eddy-island interaction, Island Mas Effect, Remote Enrichment.

Resumo

O arquipélago de Cabo Verde é um sistema de oceano profundo constituído por 10 ilhas, localizado no Oceano Atlântico Nordeste a ~600 km da costa ocidental Africana. O arquipélago divide-se em dois grupos principais: as ilhas de Barlavento, são aquelas localizadas mais a norte; e as ilhas de Sotavento, localizadas mais a sul. Esta região é caracterizada por um sistema oceânico altamente dinâmico, em que as correntes de superfície são regidas pelo deslocamento sazonal da Zona de Convergência Intertropical (ZCIT). Para além disso, a costa ocidental Africana é caracterizada como uma das áreas biologicamente mais produtivas do mundo, como consequência do afloramento costeiro, que por sua vez segue o mesmo comportamento sazonal atmosférico. A interação destes dois sistemas faz com que o arquipélago esteja consideravelmente exposto a processos remotos, que não são gerados no arquipélago, mas ainda assim podem ter implicações na oceanografia local. Embora estes processos tenham sido extensivamente estudados no passado, a integração do arquipélago no contexto regional foi raramente alcançada. O arquipélago pode também induzir perturbações no ambiente, principalmente pelo efeito de barreira na circulação atmosférica provocado pela topografia de alta altitude. Consequentemente, estas perturbações podem provocar processos oceânicos localizados, muitas vezes na forma de vórtices oceânicos – conhecidos na gíria cientifica como *eddies*. Por sua vez, estes *eddies* são conhecidos por induzir impactos a nível biológico, sendo até responsáveis por impulsionar a produtividade primária local. Este fenómeno tem como designação "Efeito de Massa de Ilha". A geração de *eddies* induzidos pelas ilhas e consequente impacto biológico têm sido cada vez mais alvo de estudo um pouco por todo o mundo, principalmente no Havai, na Ilha da Madeira e nas Canárias. Curiosamente, estas ilhas partilham muitas das características que são favoráveis para a ocorrência deste fenómeno com o arquipélago de Cabo Verde. No entanto, e tendo em conta o conhecimento existente sobre Cabo Verde, o acontecimento de tais processos tem sido visto apenas como especulativo. É também extremamente importante notar que os *eddies* de campo distante – aqueles que são criados fora da área de Cabo Verde, mas que intersectam esta mesma área durante o seu tempo de vida – podem ter implicações significativas na geração de *eddies* de campo próximo – aqueles que são criados dentro da área do arquipélago – (supostamente) induzidos pelas ilhas. Porém, tal interação nunca foi tomada em consideração em estudos desta natureza.

Posto isto, duas hipóteses são propostas para o presente estudo: podem os *eddies* de campo distante ter implicações nos processos físicos e biológicos de ilhas oceânicas, que até à data foram negligenciados? E, se for o caso, de que forma podem as ilhas impactar estes *eddies* de campo distante? De modo a responder a estas perguntas, a caracterização do campo de *eddies* ao redor e na área de Cabo Verde é apresentado, dando especial atenção aos *eddies* de campo distante e aos *eddies* de campo próximo. Para tal, foram utilizados vários parâmetros ambientais, tais como o vento, correntes oceânicas de superfície, topografia da superfície do oceano, concentrações de superfície de clorofila *a* (Chl*a*)*,* e temperatura da superfície do oceano. Estes dados foram medidos por deteção remota, a partir de sensores a bordo de vários satélites, que são de acesso livre. Após a sua obtenção, os dados foram processados a partir de scripts desenvolvidos no MatLab. Tendo em conta a natureza exploratória do estudo, foi primeiro realizada uma análise preliminar com o objetivo de determinar processos regionais que possam ter um impacto direto no arquipélago, e assim delinear o seguimento das análises a serem realizadas, assim como a estrutura do trabalho. Subsequentemente, foi adotado um procedimento mais detalhado, de modo a evidenciar os mecanismos e processos a uma escala local. Para além da classificação dos *eddies* de acordo com a origem, foi também designada uma classificação com base no tempo de vida, em que: *eddies* de curta vida são aqueles que não ultrapassam os 30 dias; *eddies* de média vida são aqueles que não ultrapassam os 60 dias; e *eddies* de longa vida são aqueles que ultrapassam os 60 dias.

De acordo com o conhecimento existente, os resultados demonstraram consistentemente que o arquipélago se enquadra numa região oceânica extremamente complexa, altamente influenciada pela dinâmica atmosférica induzida pelo comportamento sazonal da ZCIT. Como esperado, este comportamento reflete-se tanto a nível regional, bem como local. Os locais de maior geração de *eddies* de média e longa vida foram identificados a sul das ilhas com maior altitude do arquipélago (Fogo e Santo Antão), reforçando o papel dos efeitos atmosféricos na geração de *eddies*. No entanto, foi também demonstrado que o arquipélago está exposto a um número considerável de *eddies* de campo distante, que interagem com as ilhas e com os processos induzidos pelas mesmas. Este tipo de interação traz implicações significativas, não só para os *eddies* de campo próximo, mas também para a propagação e evolução dos *eddies* de campo distante. Desta forma, observou-se que os possíveis cenários de tal interação foram (do mais recorrente para o menor): deformação dos *eddies* incidentes; destruição dos *eddies*; divisão dos *eddies* incidentes e consequente geração de novos *eddies* de campo próximo; e deflexão dos *eddies* induzida pela topografia das ilhas.

Considerando a quantidade substancial de evidências que suportam a ocorrência sistemática desta interação entre *eddies* de campo distante e as ilhas de Cabo Verde, concluiu-se que grande parte dos *eddies* de campo próximo sejam um produto ou subproduto deste processo. Por esta razão, é muito difícil determinar a natureza dos *eddies* gerados no arquipélago, i.e., se são gerados por mecanismos físicos induzidos pelas ilhas, pela interação entre *eddies* de campo distante com as ilhas, ou até mesmo interação de *eddies* de campo distante com *eddies* de campo próximo.

Este tipo de interação é ainda mais óbvio na caracterização biológica do arquipélago. Foi possível observar que os *eddies* de campo distante estão frequentemente associados a níveis de Chl*a* elevados, que por sua vez está relacionado com o local de origem – a costa ocidental Africana. À medida que estes *eddies* intersectam as ilhas, a concentração superficial de Chl*a* aumenta consideravelmente, atuando assim como enriquecimento remoto. Além disso, os *eddies* ciclónicos criados pelas ilhas são capazes de injetar água rica em nutrientes de camadas profundas para a zona eufótica, favorecendo assim comunidades fitoplânctónicas e originando o aparecimento de concentrações elevadas de Chl*a* junto às ilhas. No entanto, estes dois mecanismos distintos são na maior parte das vezes vistos a atuar simultaneamente, o que dificulta a diferenciação entre enriquecimento remoto do enriquecimento local. Estes resultados desafiam a ideia de que a produtividade biológica em ilhas oceânicas profundas é exclusivamente induzida por mecanismos associados às perturbações das ilhas no ambiente ao seu redor.

Assim sendo, o presente estudo demonstra que a combinação de processos de campo distante e de campo próximo são as principais causas na geração de *eddies* de mesoescala no arquipélago, que por sua vez têm implicações importantes a nível biológico. Tais observações fazem com que o Arquipélago de Cabo Verde seja um local perfeito para o estudo deste tipo de interação, motivando assim futuros estudos.

Palavras Chave: Cabo Verde, *Eddies* de Mesoescala, Interação *Eddy*-ilha, Efeito de Massa de Ilha, Enriquecimento Remoto.

Index

Figure Index

Table Index

List of Acronyms and Abbreviations

ADT	Absolute Dynamic Topography
AVISO	Archiving Validation and Interpretation of Satellite Data in Oceanography
CC	Canary Current
Chl*a*	Chlorophyll *a*
CVFZ	Cape Verde Frontal Zone
CV	Cape Verde area
DO	Dissolved Oxygen
EKE	Eddy Kinetic Energy
GD	Guinea Dome
GMF	Geophysical Model Function
HLCC	Hawaiian Lee Counter Current
IME	Island Mass Effect
ITCZ	Intertropical Convergence Zone
MC	Mauritanian Current
NACW	North Atlantic Central Water
NEC	North Equatorial Current
NECC	North Equatorial Counter Current
Re	Reynolds Number
RMS	Root Mean Square
SACW	South Atlantic Central Water
SLA	Sea Level Anomaly
SSH	Sea Surface Height
SST	Sea Surface Temperature

1. Introduction

Oceanic islands are common geological features in the world's oceans and are of considerable scientific interest in the present days. They can be found in shallow waters – known as continental islands, or in deep waters – known as oceanic islands (Wallace, 1892). Normally of volcanic origin and far from the nearest continent, oceanic islands contrast from continental islands in the sense that the latter type are an integrated element of the continental shelf and, as a consequence, are commonly found near the continent of origin. Naturally, the environment in which islands are involved determine with great significance its geomorphology and its biological patterns. On the other hand, an island can induce significant physical perturbations in the background atmospheric or oceanic flow, which in turn must have direct impacts in the biological realm (Barton, 2001; Basterretxea *et al.,* 2002).

Continental islands are more susceptible to coastal oceanic processes than oceanic islands due to its proximity to the coast. Thus, one may expect that isolated oceanic islands are not so biologically productive as continental islands. This is not entirely true, as there are several cases of isolated islands – mainly in the pacific – that exhibit enhanced levels of primary production and an exceptional number of endemic species (e.g., Doty and Oguri, 1956; Seki *et al.,* 2001; Palacios *et al.,* 2006, Andrade *et al.,* 2014; Gove *et al.,* 2016). The specific reasons for why waters surrounding isolated islands are so productive in presumably oligotrophic waters has been subject to a lot of debate over the years. After sailing for weeks in the vast open ocean aboard the HMS Beagle, Darwin was perplexed when he came across what he believed to be one of the most diverse ecosystems on the planet – coral reefs (Darwin, 1842). How could such a dynamic ecosystem teeming with life exist in a seemingly unproductive environment? This is now well known in the scientific community as Darwin's paradox. Since then, several studies have focused on the investigation of the unexpected biological productivity in such systems, giving rise to the concept of Island Mass Effect (IME).

IME was first introduced by Doty and Oguri (1956) as an increase in Chlorophyll concentration in the Hawaiian archipelago. Subsequently, this concept was generalized to include bathymetry-induced island effects on the local oceanography (Hamner and Hauri, 1981) and its consequent impact on the biological domain (Caldeira *et al.,* 2005). Many studies managed to create a valid physical - biological relationship, and island-induced flow perturbations can be as

diverse as: the formation of island wakes that result from the blocking of atmospheric or current inflow and can extend several island diameters downstream (e.g. Barkley, 1972; Hernández-León, 1991; Caldeira and Marchesiello, 2002; Chérubin and Garavelli, 2016); geophysical vortices – known as eddies – that stir and enhance vertical mixing in the wakes (e.g. Hamner and Hauri, 1981; Seki *et al.* 2001; Coutis and Middleton, 2002; Hasegawa *et al.* 2009); fronts and filaments (e.g. Caldeira *et al.,* 2002; Barton *et al.,* 2004); upwelling processes – other than eddies – that bring nutrients to the euphotic zone (e.g. Aristegui *et al.,* 1994; Rissik *et al.*, 1997; Palacios *et al.,* 2002; 2004; Hasegawa *et al.* 2004); among others (Elliot *et al.,* 2012). Whilst these processes are thought to be the major contributors for IME, the latter can still be fuelled by several land-born factors, namely: the input of macro and micronutrients from island runoff (Sander and Steven, 1973; Dandonneau and Charpy, 1985; Bell, 1992; Elliot *et al.,* 2012) and groundwater discharges (Hwang *et al.,* 2005; Tait *et al.,* 2014; Gove *et al.*, 2015; Moosdorf *et al.,* 2015); contributions from benthic processes (Doty and Oguri, 1956; Dandonneau and Charpy, 1985); or even the combination of oceanic mechanisms with land-born factors (Signorini *et al.*, 1999; Palacios, 2002; Martinez and Maamaatuaiahutapu, 2004). For this reason, it is very important to clarify the nature of the mechanisms that drive the IME, but more importantly, one should not neglect the regional context and the far-field impacts to which an island may be exposed to.

From the physical point of view, IME has been extensively reported in the most various places (e.g., Jones, 1962; Arístegui *et al.,* 1997; Heywood *et al.,* 2000; Perissinotto *et al.,* 2000; Caldeira *et al.,* 2002; Seki *et al.,* 2001; Andrade *et al.,* 2014). Such studies are remarkably consistent between each other, in the sense that similar methods follow similar patterns and usually arrive to similar conclusions. However, the integration of islands in the regional context was seldom achieved, as very few studies successfully linked local island effects to remote enrichment through far-field features (e.g. Barton *et al.,* 1998, 2004; Palacios, 2004, Caldeira and Jesus, 2017). Hence, two hypotheses are proposed: can far-field features have considerable implications on oceanic islands and associated physical/biological processes, that have been neglected to present date? And if so, to what extend can islands impact such far-field features?

Cape Verde is a typical group of deep ocean islands disposed in a non-linear orientation, located near the north-western African coast (~600 km) in a hydrographically complex region, strongly affected by seasonal atmospheric dynamics (Lázaro *et al.,* 2005). In its vicinity, the Canary Current Upwelling System is one of the four large systems of Eastern Boundary Currents (Hagen,

2001, Chaigneau *et al.,* 2009) and is considered one of the biologically most productive oceanic regions in the world (Pradhan *et al.,* 2006; Pastor *et al.,* 2008; Löscher *et al.,* 2015). The latter is marked by the presence of several mesoscale features that can possibly have a profound effect on the regional oceanography, such as: filaments, that extend out to hundreds of kilometres from the adjacent coast to offshore (Van Camp *et al.,* 1991; Gabric *et al.,* 1993; Kostianoy and Zatsepin, 1996; Lange *et al.,* 1998); and eddies, that can have considerable impacts in the ocean (e.g., Chaigneau *et al.,* 2009; Karstensen *et al.,* 2015; Löscher *et al.,* 2015; Fiedler *et al.,* 2016; Hauss *et al.,* 2016; Schütte *et al.,* 2016a; 2016b). Several other studies strived to identify and explain the nature of many oceanic features in the region (e.g. Zenk *et al.,* 1991; Löscher *et al.,* 2015; Hauss *et al.,* 2016), but all failed to integrate the Cape Verde Archipelago in the regional context, as well as the archipelago's impact on the far-field incoming features.

In what concerns the near field, Chavanne *et al.* (2002) were able to demonstrate for the first time theoretical evidences of a shadow effect induced by the islands topography, when a wake of weak winds, flanked by strong winds, was observed in the lee of all the major islands. It is now well established that this mechanism may drive the generation of cyclonic and anticyclonic eddies in the island(s) wake (Calil *et al.,* 2008; Jiménez *et al.,* 2008; Yoshida *et al.,* 2010; Jia *et al.,* 2011; Couvelard *et al.,* 2012; Caldeira *et al.,* 2014), which in turn must have direct implications in the biological realm (e.g., Arístegui *et al.,* 1997; Barton *et al.*, 2000; Seki *et al.*, 2001; Coutis and Middleton, 2002). Yet, the archipelago lacks empirical observations that support such phenomenon. Most likely as a consequence of the wind shadowing effect, Lázaro *et al.* (2005) identified a nearly permanent anticyclonic eddy south-southwest of the islands, which was more pronounced during the periods of strongest wind intensity (Varela-Lopes and Molion, 2014). The far-reaching implications of the archipelago were also introduced by Chavanne *et al.* (2002), as the authors suggested that the island-induced blocking of atmospheric flow could originate a zonal counter-current, following the same nature as the thoroughly described Hawaiian-Lee Counter Current (HLCC) (Qiu *et al.,* 1997; Lumpkin, 1998; Xie *et al.,* 2001). Other similar observations conducted at a regional scale further reinforce such hypothesis (e.g. Chelton *et al.* 2004; Chaigneau *et al.,* 2009), though none had the specific objective of investigating the archipelago.

All things considered, one may arrive to the conclusion that the archipelago's exposure to regional dynamics, as well as the interaction between atmospheric and oceanic processes at a local scale, are important factors that to the present date are very poorly understood. Hence, the

investigation of such mechanisms is of utmost importance. The current study aims to fill this gap and thus better comprehend the relation between the far and near-field which affect the Cape Verde Islands. Special attention is regarded towards the nature and the interaction between the incoming and locally-generated eddies and, as a complementary investigation, the biological implications of such physical mechanisms are assessed, focusing in the analysis of surface Chlorophyll *a* (Chl*a*) concentrations in the vicinity of the islands.

This project is organised as follows: In the next sub-chapters, a brief introduction to the mechanisms in study is presented, in which eddies (in general), island-wakes and island-induced eddies are described. In Chapter 2, a literature review concerning the geographical setting is conducted, elucidating the reader to the physical background which affects the archipelago. In Chapter 3, the description of the datasets characteristics and processing methods is conducted. In Chapter 4, the best-suited results are presented and are subsequently discussed in Chapter 5. Lastly, the final conclusions are discussed in Chapter 6.

1.1. Oceanic Eddies

It has been well established that oceanic eddies (hereinafter referred as eddies) are ubiquitous features in the world's oceans (Robinson, 2010). Basically, an eddy is defined as a self-rotating coherent body of water (Talley *et al.,* 2011), which propagates through the ocean mostly from self-advection and planetary vorticity effects (Cushman-Roisin *et al.,* 1990; Chelton *et al.,* 2011), though several other factors can influence their propagation (e.g., Simmons and Nof, 2000; Cenedese *et al.,* 2005; Andres and Cenedese, 2013). These features can range between a few kilometres, to tens (sub-mesoscale) or even hundreds (mesoscale) in diameter, and are categorised according to their rotational flow (Talley *et al.,* 2011). In the northern (southern) hemisphere, cyclonic eddies flow in the counterclock (clockwise) direction, while anticyclonic eddies flow in the clockwise (counterclockwise) direction (Tomczak and Godfrey, 1994). Due to the effect of earth's rotation (also known as the Coriolis force), cyclonic eddies are characterised by a depression and negative sea surface anomaly at its core, while anticyclonic are associated with an elevation and consequent positive sea surface anomaly. With the advent of new technologies – especially satellite-based remote-sensing instruments – these features have been increasingly focus of investigation (Robinson, 2010), and it is now common knowledge that they can have profound implications in the physical, chemical and biological properties of the ocean (Robinson, 2010).

Such features are reported to be the one of the major sources of kinetic energy in the oceans (Richardson and Walsh, 1986). Furthermore, they can transport water in their cores for long distances (Alpers *et al.,* 2014, Romero *et al.,* 2016), being even able to go across frontal zones (Barton, 1987). Depending on its nature (cyclonic or anticyclonic) and place of origin, these waters can have considerably different properties in relation to the surrounding waters. In that sense, eddies are able to create and sustain their own distinct environment, which can be characterised by: nutrient-rich waters from upwelling regions, that under favourable condition enhance biological productivity even in presumably oligotrophic regions (Löscher *et al.,* 2015, Romero *et al.,* 2016), and are thus potentially favourable for fish larval survival which in turn can act as a medium for transportation and colonization (Condie and Condie, 2016); oxygen-depleted waters that create "dead-zones" in the middle of the ocean (Karstensen *et al.,* 2015, Hauss *et al.,* 2016; Schütte *et al.,* 2016b); among many others.

Apart from the horizontal advection of water, eddies can induce vertical fluxes in their interior (Arístegui *et al.,* 1997; Gaube *et al.,* 2013). As such, upwelling (downwelling) occurs in cyclonic (anticyclonic) eddies due to the divergent (convergent) movement of water at the surface because of the Coriolis force, which uplifts (deepen) the thermocline and thus enhances (decrease) nutrient availability through self-induced Ekman-suction (pumping) mechanisms (Lin *et al.,* 2010; Gaube *et al.,* 2013). For cyclonic eddies, this mechanism is an important source of cold, nutrient-rich water to the euphotic zone (Gaube *et al.,* 2013), which in turn benefits the primary production and drives the local increase of Chl*a* at the surface (Alpers *et al.,* 2014, Romero *et al.,* 2016). Subsequently, the latter favours the gathering of grazers and predators, acting as an "oases" in the open ocean (Lévy *et al.,* 2001; Lin *et al.,* 2010; Hauss *et al.,* 2016). In contrast, anticyclonic eddies do exactly the opposite, as they inject water from surface to deeper layers. Eddies generation can be induced by the most diverse physical mechanisms in the ocean, such as: topography effects (Barkley, 1972; Heywood *et al.,* 1990; Alpers *et al.,* 2014); current shear (Chelton *et al.,* 2011; Schütte *et al.,* 2016a); ocean-atmosphere interaction (Calil *et al.,* 2008; Jiménez *et al.,* 2008; Coulevard *et al.,* 2012; Hogg *et al.,* 2016); or even eddy-eddy interaction (Sangrà *et al.,* 2009; Chelton *et al.,* 2011). However, one of the most interesting mechanisms in the generation of eddies is the island-induced processes, which deserve especial attention in the current study.

1.2. Island Wakes and Island-induced Eddies

An island, or a group of islands, can produce distinctive signatures in the environment around them. One of the most characteristic features are known as island wakes and the subsequent eddy generation, typically streaming away in a dominant direction concomitant to the background wind or current flow (Robinson, 2010). It is important to note, however, that there are different ways to perceive such features.

From the oceanographic point of view, there are two types of islands disturbances (Tomczak, 1998). One occurs in shallow stratified shelf seas, where the current is clearly dominated by a tidal regime that moves water in both directions and gets blocked by the island bathymetry, generating a wake in the opposite side of the impinging flow (e.g., Pingree and Maddock, 1980; Hamner and Hauri, 1981; Heywood *et al.,* 1990). Another takes place both in shallow and deep water, when a clear dominating flow passing an island generates a wake or zone of flow disturbance that can extend several island diameters, ultimately leading to the generation of eddies (e.g., Barton *et al.,* 2000; Caldeira *et al.,* 2005). The scale of the eddies at their initial phase is normally not far from the diameter of the island which provoked it (Dong and McWilliams, 2007; Sangrá *et al.,* 2009), with the exception when two identical vortices merge and create one eddy with the double diameter and rotation velocity of the original (Barton, 2001). Barkley (1972) introduced the first empirical case study of an island wake and consequent island-induced eddies through observations of fishing gear drift and surface currents measurements at Johnston Atoll in the Pacific Ocean, where the data showed a vortex-like drifting pattern. Subsequently, several other studies were conducted worldwide, providing a broader understanding and improving the scientific knowledge on this issue.

Current wakes arise from the friction experienced by the flow field when the ocean currents intercept and get deflected by the island. This physical barrier forces the water to depart from a straight path inducing an acceleration perpendicular to the original direction, known as the inertial force (Tomczak, 1998). Another important force that must be taken into account is the frictional force associated with the boundary layer around the island. The balance of these two forces plays a crucial role determining the behaviour of the flow. If the frictional force dominates over the inertial force, the water transport gets dragged along the island's coasts, but if the dominant forces are reversed the water flow is therefore thrown off its path and gets separated from the island. This balance is very closely related with the Reynolds number (*Re*), which takes into account the original

flow velocity, the width of the obstacle (in this case, an island) and the horizontal molecular viscosity.

In an ideal case, Batchelor (1967) demonstrated that the *Re* is a good method for determining the turbulence in a fluid. The author found that by increasing the flow velocity or the obstacle diameter, the turbulence of the flow would equally increase, leading to the generation of a vortex pair with opposite rotation attached to the obstacle, periodic oscillation of the wake, eddy shedding and eventually to a Von Karman Vortex Street. Nonetheless, it is a proven fact that the ocean is far from being an ideal case, given that: it is rare to find a perfectly cylindrical and isolated island in deep ocean; the upstream flow velocity and direction is not constant, as it is under the influence of a variety of factors; and the molecular viscosity in the equation must be replaced by the eddy viscosity in the ocean, which is poorly understood (Barton, 2001). The application of such theory in a complex system – particularly Cape Verde Archipelago, which is dispersed in a non-linear orientation and under a non-laminar incident flow – is not a straightforward process. Thus, it is not considered in the current study.

As from the atmospheric point of view, it is well known that the atmosphere-ocean interaction is responsible for a high transfer of energy. Surface wind stress is the principal factor forcing basin-scale ocean circulation (Stewart, 2008; Talley *et al.,* 2011) and is responsible for inducing local currents and turbulent features (Elken, 2016). Albeit the significant lower density in relation to the ocean, the atmosphere is subjected to the same kind of fluid dynamics when intercepting an obstacle. Hence, oceanic islands topography can – as for oceanic flow – disturb the atmospheric flow, ultimately generating one of the most remarkable and distinct island-induced features in the adjacent environment. The atmospheric effect occurs when the incident wind flow gets blocked by an island high topography and creates extended sheltered regions in the lee zone downwind with an occasional vortex-like trail of clouds (Figure 1.1), previous referred as a Von Karman Vortex Street (e.g., Chopra and Hubert, 1964; Caldeira *et al.,* 2002; Couvelard *et al.,* 2014; Spedding, 2014).
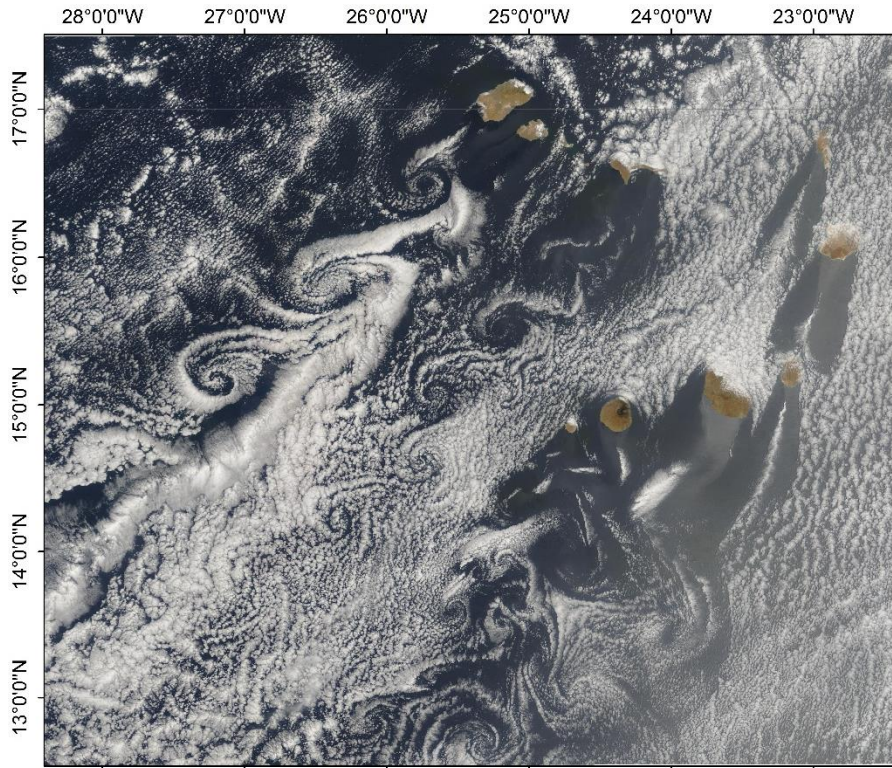
Figure 1.1 – Atmospheric shedding effects induced by the Cape Verde Archipelago: Von Karman Street in the lee of Santo Antão, São Nicolau and Fogo Islands, and wind wakes in the lee of Sal, Boavista, Maio and Santiago Islands. Source: Nasa. Georeferenced in ArcGIS.

This wind wake normally extends a few thousand kilometres from the island in the prevailing wind direction. The local response may be superficial, with the development of a diurnal thermocline in the sheltered region (e.g., Barton *et al.,* 2000; Basterretxea *et al.,* 2002; Caldeira, 2002; Caldeira *et al.,* 2005). In the case of persistent steady winds, however, the implications are more significant. Sharp horizontal wind shear lines may form on the edges of the island wake, resulting in rapid variations of the Ekman transport in the ocean (Barton, 2001; Robinson, 2010). At the western boundary of the lee, the upwelling of deeper waters must compensate the divergence - elevating the pycnocline closer to the surface - while at the eastern boundary, sinking of surface water through Ekman pumping must occur as a product of the convergence – deepening the pycnocline (Figure 1.2). Some authors argue that these processes are enhanced when the steady wind is capped by an atmospheric inversion layer (e.g., Barton et al., 2000; Hafner and Xie, 2003). According to Chavanne *et al.*, (2002), this condition is well meet in the Cape Verde Islands, where it is possible to find strong and steady winds ($\sim$8 m.s^{-1}) generated by the Azores High – Saharan Low system, with the addition of high altitude topography (1500-2800 m) which in turn is well above the inversion layer (500-700 m).
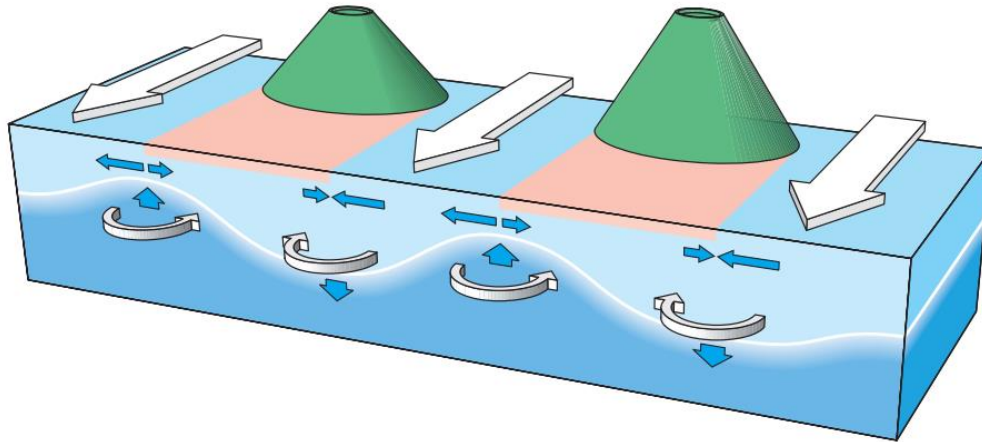
Figure 1.2 – Representation of the eddy generation mechanism induced by wind shear. Red area represents warm stratified surface water in the lee of the island; white line corresponds to the pycnocline; big white arrows represent the wind; curved arrows represent the eddy cyclonic and anticyclonic movement which lead to upwelling and downwelling (vertical blue arrows), respectively. Retrived from Chavanne *et al.* (2001).

For islands with high mountains where the prevailing wind is parallel to the dominant ocean current, it is difficult to access the nature of the eddies that are generated downstream, i.e. from current or wind induced processes (Barton, 2001). In Hawaii, Patzert (1969) concluded that the impinging flow was too weak for eddy generation, thus attributing the main cause to the local wind blowing through the narrow passage between the islands of Maui and Hawaii. In Canary Islands, Arístegui *et al*. (1994) noticed the presence of cyclonic and anticyclonic eddies downstream of Gran Canaria. The authors suggested that these are more likely to be provoked by the island's impact on the oceanic flow rather than by the influence of the wind, since eddies are recurrent even during periods of low wind intensity. The latter was further confirmed by Ródrigues *et al.* (1999) and more recently by Jiménez *et al.* (2008), who presented strong theoretical evidences (model results) that supports the previous hypothesis. Still, one must consider the possibility that wind and current island-induced disturbances may act as coupled mechanisms and thus enhance the production of eddies in such systems, especially when the two are not capable of acting alone (Barton *et al.,* 2000; Basterretxea *et al.,* 2002).

In some extraordinary cases, the wind blocking effect can have a regional impact over the ocean, as it is the case of Hawaii. Xie *et al.* (2001) detected a wind wake induced by the islands sheltering of the north-easterly steady trade winds, extending 3000 km westward in the lee zone of the archipelago. The authors suggested that this feature is responsible for the existence of the Hawaiian Lee Counter Current (HLCC) that flows eastward in the opposite direction of both the trade winds and the westward Pacific North Equatorial Current (Sasaki *et al.*, 2010), leaving a

warm surface and subsurface water signature stretching 8000 km away from the Asian coast (Xie *et al.*, 2001). Following the same nature of Hawaii, Chavanne *et al.* (2002) introduced the possibility that similar (but weaker) features to the HLCC are likely to happen in Cape Verde, thus justifying additional studies in the region.

2. Geographic Settings

To better understand the nature of the ocean circulation and features, one must initially construct knowledge regarding the geographic details of the region – including the regional bathymetry/topography, the wind field and its seasonality, among several other relevant factors for the study (Tomczak and Godfrey, 1994). As such, a brief literature review about the oceanic and atmospheric characteristics for the region of Cape Verde is presented in this chapter.

2.1. Cape Verde Archipelago

The Republic of Cape Verde is an island country composed by ten islands and thirteen islets arrayed in a west-facing horseshoe disposition, being all of them from volcanic origin (Ramalho, 2011). Along with the Azores, Madeira and the Canary Islands, the Cape Verde Archipelago is the southernmost group of islands which form the Macaronesia (EC, 2017). It is located in the North Atlantic and lies 450 – 600 km off the western coast of Africa, in a geographical area between the latitudes and longitudes of 14º40' – 17º30'N and 21º30' – 25º30'W, respectively. It occupies a total area of 4033 km^2 unevenly distributed among the islands, with a significant total coast line of approximately 1020 km^2 (DGA, 2004).
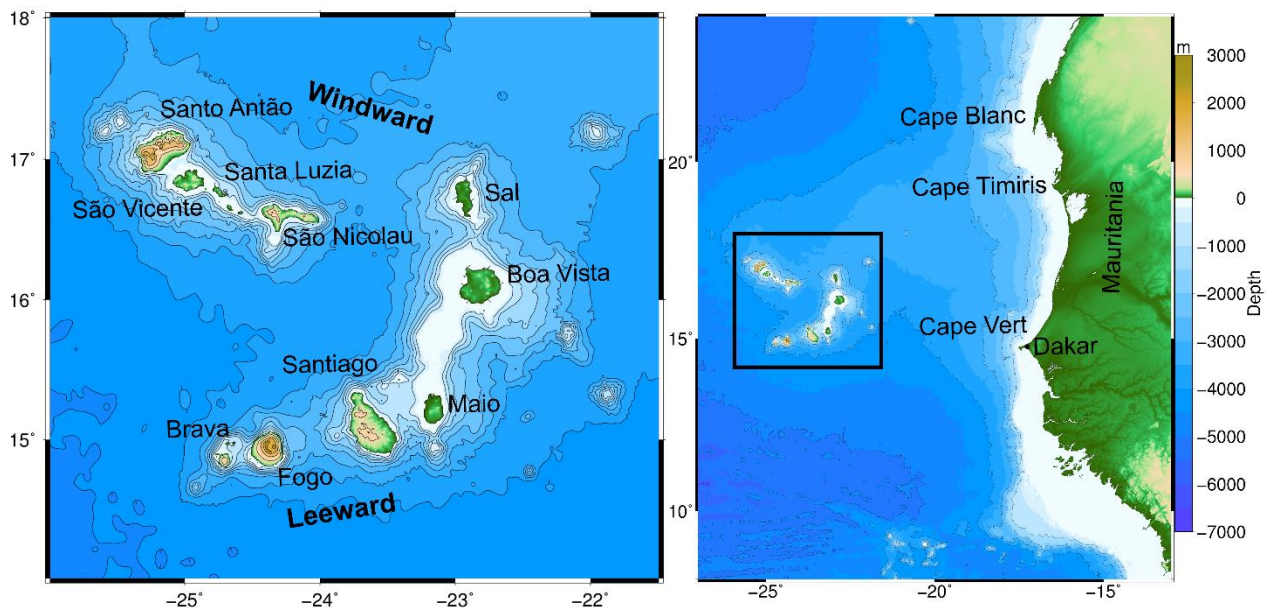
Figure 2.1 – (a) Topography and bathymetry of the Cabo Verde islands, with the identification and grouping of the islands. Isolines have a 500-m interval. (b) Regional setting of the archipelago, with the identification of the main coastal features. Isolines have a 1000-m interval. Datasource: SRTM 30 m. Created in GMT, edited in Inkscape.

The islands are divided into two main groups (Figure 2.1): The Windward group, comprising the islands of Santo Antão, São Vicente, Santa Luzia, São Nicolau, Sal, and Boa Vista; and the Leeward group, comprising Maio, Santiago, Fogo, and Brava. However, in terms of geomorphology and accordingly to the regional bathymetry, the archipelago can be divided in two distinct groups: the northern chain, with a west-east orientation from Santo Antão to São Nicolau, probably constitutes a single elongated edifice; and an east-to-southern chain, starting in Sal and ending in Brava. Despite this division it is possible to consider Brava and Santiago as a detached edifice, since they are separated by a considerable depth of 3000 m. Between Boa Vista and Maio islands the bathymetry reveals a shallow area, known as João Valente bank with the highest summit having 14 m depth (Ramalho, 2011). The regional bathymetry also indicates the presence of several seamounts near the islands.

The origins of the archipelago are attributed to the long-term mid-plate volcanism associated with the Cape Verde hotspot which rests upon the Cape Verde Rise. The volcanic activity was not continuous – meaning that there were different periods of activity –, leading to different formation ages. By the surface geomorphology one may conclude that the eastern group of islands (Sal, Boa Vista and Maio), which are characterized by long beaches and flat topography – evidences of erosion – were formed first. The other mountainous islands with higher peaks (Figure 2.2, Annex A.1) and sharper coastline are more recent.
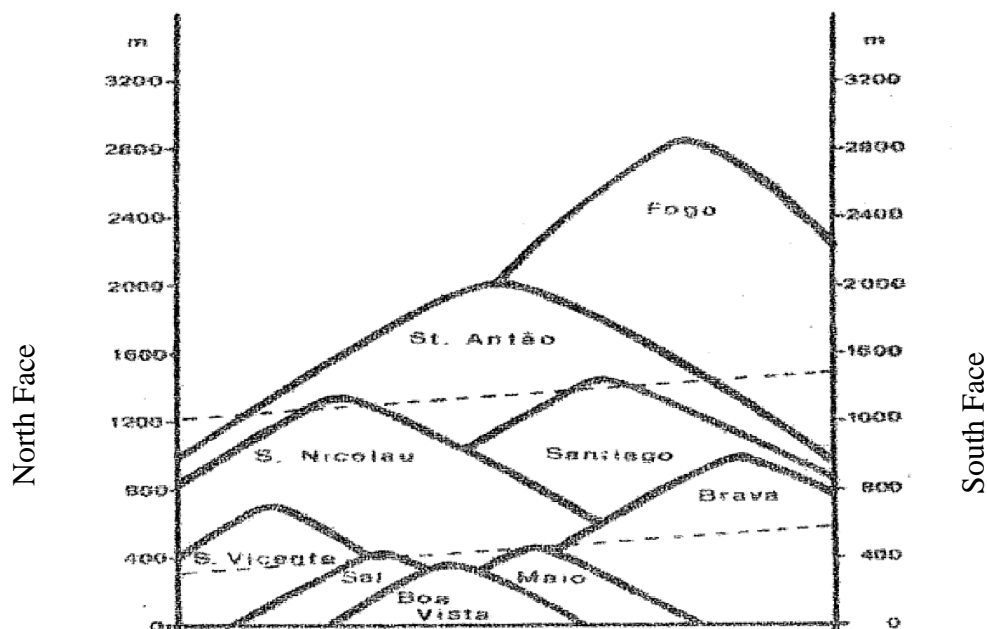
Figure 2.2 – Schematic representation of the highest altitude of every island in the Cape Verde Archipelago. Adapted from Saraiva (1961).

2.2. Climate

The islands are characterized by a tropical oceanic climate, with a small annual temperature amplitude in the range from 19 to 29 ºC (Ramalho, 2011). Due to its location in the Sahelian arid belt, the islands are exposed to very low precipitation levels – varying from ≤ 300 mm.yr^{-1} in low altitudes to ≥ 700 mm.yr^{-1} in higher altitudes (DGA, 2004) –, and a seasonal rainfall regime characterized by dry (November - June) and wet (July - October) seasons (DGA, 2004; Varela-Lopes and Molion, 2014). The archipelago's climate is under the direct influence of the Intertropical Convergence Zone (ITCZ) and subjected to prevailing northeast trade winds occurring throughout the year (Figure 2.3), with a higher intensity in winter and spring (9 m.s^{-1} maximum mean speed; NCAS, 2017) (Fernandes *et al.,* 2005; Lázaro *et al.,* 2005; Varela-Lopes and Molion, 2014; Faye *et al.,* 2015). These are responsible for the intensity and direction of local wave and surface currents – which have asymmetrical characteristics between coastlines facing north and south (Ramalho, 2011) –, as well as for the sea level height (Gomes *et al.,* 2015). Higher wind speeds are more frequent in the Leeward Islands than in the Windward Islands (DGA, 2004).
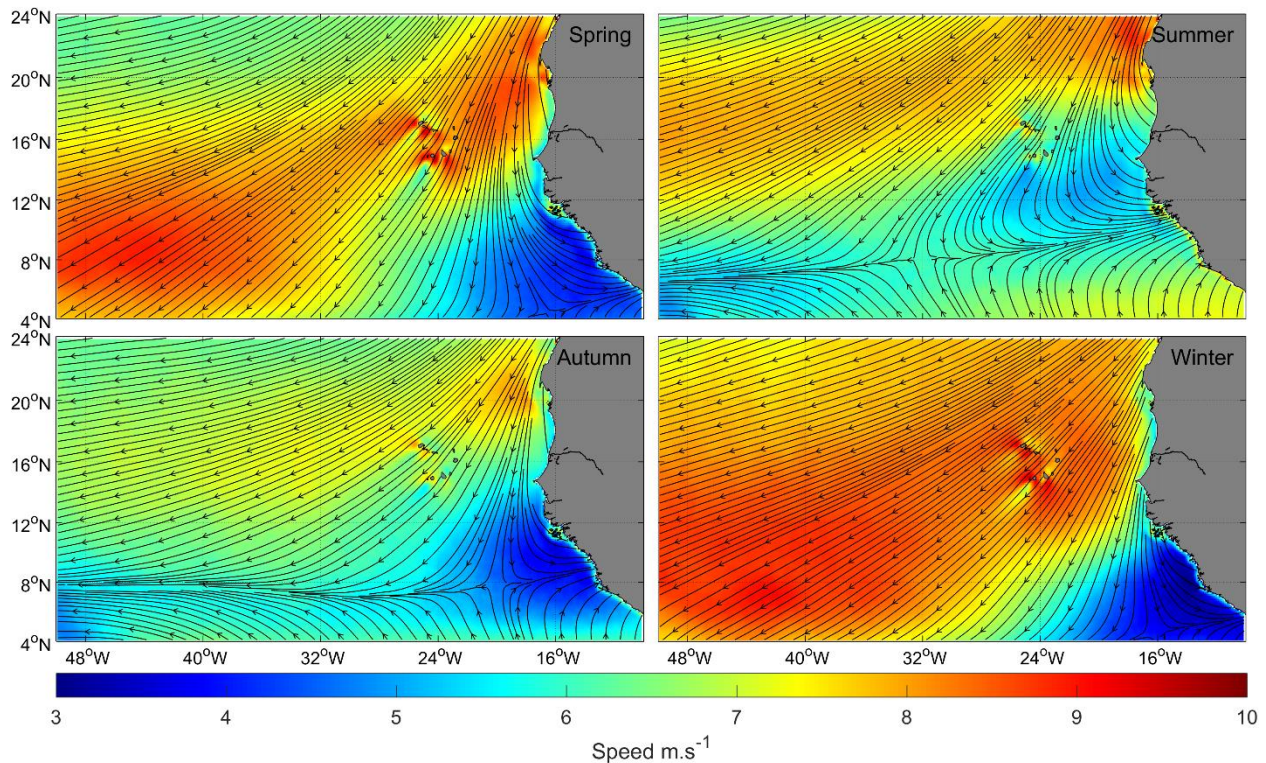
Figure 2.3 – Representation of the seasonal mean wind speed and direction in the region of Cape Verde, between the years of 2003 to 2014. The presence of the ITCZ can be easily identified as a wind confluence zonal region at lower latitudes. Data: QuikSCAT and ASCAT.

The ITCZ lies in the equatorial band and can be identified as a tropical belt of minimum wind speeds (Molinari *et al.,* 1986), where deep convective clouds (Waliser and Gautier, 1993) lead to a maximum regional mean precipitation (Philander *et al.,* 1996), and conversely to a regional solar radiation minimum (Tomczak and Godfrey, 1994). The latter results from the convergence of the southward and the northward warm and moist lower branches of the Hadley cell (from the northern and southern hemisphere, respectively) – known as the trade winds (Schneider *et al.,* 2014). In the regional context, the ITZC follows the sun's zenith point (Soares, 2015) and migrates between 9ºN in summer and 2ºN in winter (Schneider *et al.,* 2014), also in response to the northward shift and weakening of the Azores High–Saharan Low system (Barton *et al.,* 1998), thus governing the large-scale surface currents (Stramma and Schott, 1999).

2.3. Oceanographic setting

The Cape Verde sea is a deep oceanic region, where the density stratification of the water column determines the hydrodynamics of the region (Gomes *et al.*, 2015). This area is located at the eastern boundary of the North Atlantic subtropical gyre at the southern limit of the Canary Current (CC) (Fernandes *et al.*, 2005). It can be regarded as a region of large-scale interactions (Figure 2.4) between the CC, the North Equatorial Current (NEC), the North Equatorial Counter-Current (NECC) and the seasonal Mauritanian Current (MC) (Mittelstaedt, 1991). Also in its vicinity, two different water masses meet between Cape Blanc and the northernmost Cape Verde Islands, forming a large-scale frontal system coined by Zenk *et al.* (1991) as the Cape Verde Frontal Zone (CVFZ), which extends zonally across the entire length of the Atlantic Ocean from the Caribbean Sea do the African coast (Emery and Meincke, 1986; Lozier *et al.,* 1995). It is marked by substantial thermohaline (Zhang *et al.,* 2003) and even larger inorganic and dissolved oxygen gradients (Pelegrí and Peña-Izquierdo, 2015), separating the warmer and saltier North Atlantic Central Water (NACW) from the cooler, fresher and richer in nutrients South Atlantic Central Water (SACW) (e.g., Mittelstaedt 1983, 1991; Péres-Rodriguez *et al.,* 2001; Meunier *et al.*, 2012). Albeit strong temperature and salinity gradients ($\geq$ 3 ºC per 40 km and 0.9 psu per 10 km, respectively), the front is density-compensated (Zenk *et al.,* 1991; Pastor *et al.,* 2008). Thus, it cannot be seen in the density field (Tomczak, 1998). Within this transition zone, an important eddy-field exists (Barton, 1987; Meunier *et al.,* 2012). The latter is more likely to arise from the kinetic energy associated with the currents interaction and topography effects at Cape Blanc, or by the

offshore advection developed along the upwelling front (Pastor *et al.,* 2008) – since density-compensated fronts are characterised by strong layering and intrusion, and only density fronts are associated with strong geostrophic jets and eddy formation (Tomczak, 1998). As such, this feature also acts as a source of offshore transport and lateral mixing, producing subsurface intrusions along the front (Zenk *et al.,* 1991; Martínez-Marrero *et al.,* 2008). Finally, its existence is – as for the interaction of the large-scale current system (Lázaro *et al.*, 2005) – potentially favourable for the aggregation of large pelagic highly migratory fish species, being thus of great socio-economic importance (Fernandes *et al.,* 2000). Given the complexity of the regional surface circulation, a detailed description of the main current systems follows.
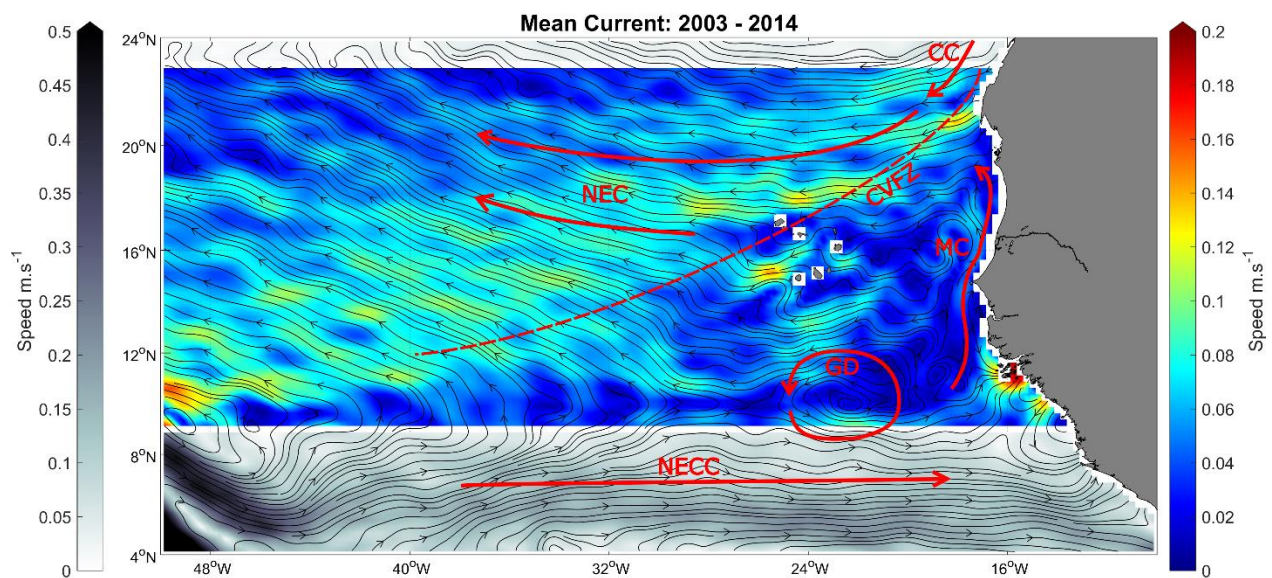
Figure 2.4 – Representation of the mean surface ocean currents and features: CC - Canary Current; NEC - North Equatorial Current; NECC - North Equatorial Counter-Current; MC - Mauritania Current; GD - Guinea Dome; CVFZ – Cape Verde Frontal Zone. Note the different colormaps. Data: GlobCurrent Geostrophic + Ekman.

Canary Current (CC) – In its southern limit, this current transports cold water from north to south off the African coast, being stronger in summer near the African coast while in winter it is stronger west of the Canary Islands (Stramma and Siedler, 1988). At latitudes near Cape Blanc (20º – 25ºN in spring and autumn, respectively) it turns south-westward, leaving the African coast to become the NEC (Mittelstaedt, 1983, 1991; Stramma *et al.,* 2005). The location of such departure from the coast is extremely relevant for the position of the CVFZ (Stramma and Siedler, 1988). Since it does not have a direct impact on the archipelago, this current is only pertinent because of the latter statements.

North Equatorial Current (NEC) – The southern part of the Atlantic tropical gyre – where subduction takes place (e.g., Schott *et al.,* 2004; Stramma *et al.,* 2005) – is characterised by a 10-15 cm.s^{-1} mean speed with a dominant west/north-westward direction (Richardson and Walsh, 1986; Stramma and Siedler, 1988; Zhang *et al.,* 2003), although some authors argue that it has a predominant south-westward direction visible throughout the year (Lázaro *et al.*, 2005). As past studies demonstrated (Arnault, 1987; Zhang *et al.,* 2003; Lumpkin and Garzoli, 2005; Lumpkin and Pazos, 2007), this difference in current direction is entirely related with the nature of the method determining it, i.e. from purely geostrophic derivation (the latter) to the incorporation of the Ekman transport (the former). According to the Ekman theory, the wind-driven component of transport in the surface boundary layer is directed perpendicularly to the right (left) of the mean wind stress in the northern (southern) hemisphere (Ekman, 1905). Thus, it is reasonable to assume that wind-driven Ekman transport has a significant impact in the region, as it is further demonstrated by the representation of the Ekman volume transport (Figure 2.5).
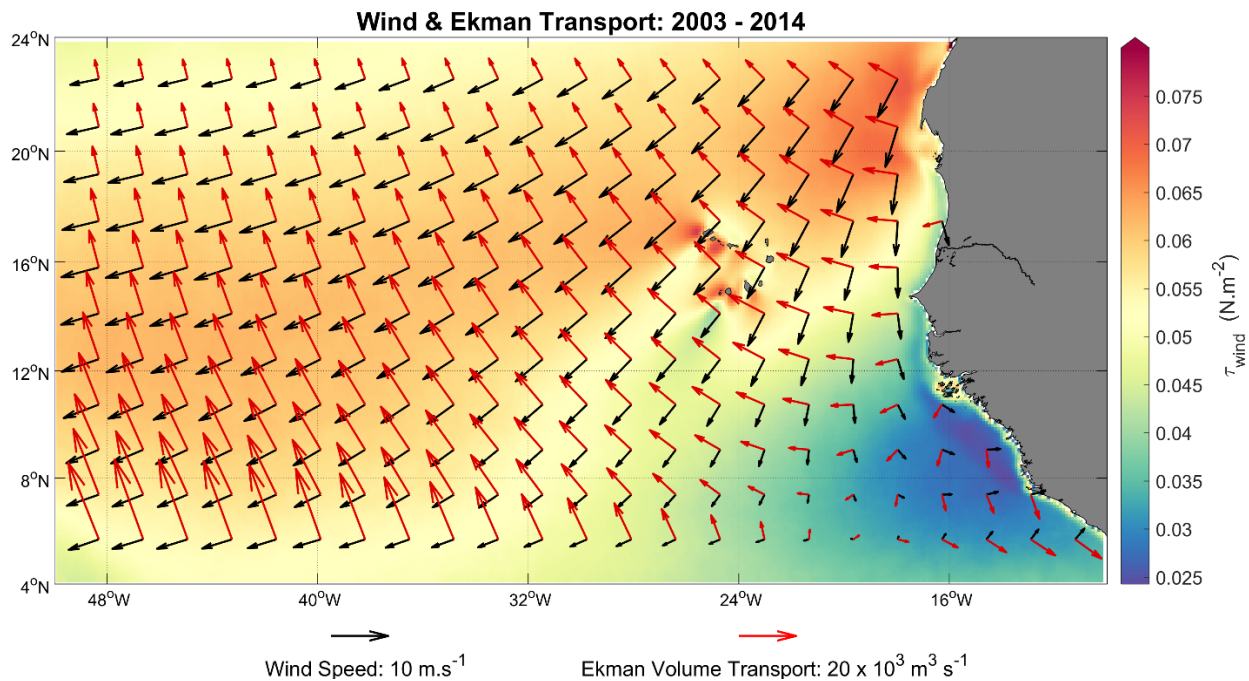
Figure 2.5 – Wind (black arrows) velocity and estimated Ekman volume transport per meter width (red arrows) represented over wind stress. Data: QuikSCAT and ASCAT.

When NEC reaches the archipelago's latitude it is divided in two branches (Figure 2.6), one turning south-westwards north of Cabo Verde islands and the other becoming a southwest flow south of the islands, both appearing to join at lower latitudes (Lázaro *et al.*, 2005). This is more evident during the first half of the year whereas in the other half the flow migrates northwards,

following the identical displacement of the NECC - both forced by the ITCZ northward migration (Stramma and Schott, 1999). The current intensity follows an identical seasonal pattern, weakening and reaching its maximum speed in summer and in spring and fall, respectively (Arnault, 1987).

North Equatorial Counter-Current (NECC) – With an eastward mean and maximum flow speed of approximately 42 cm.s^{-1} and 147 cm.s^{-1}, respectively (Frantantoni, 2001), this current is particularly strong in summer and early fall (Arnault, 1987; Mittelstaedt, 1991) – when the ITCZ reaches its northernmost position (Lázaro *et al.* 2005; Schütte *et al.,* 2016a). It is during this period that the current is most likely to have an influence in the southern side of the Cape Verde Archipelago (Fernandes *et al.,* 2005). In the western part, however, the current does not follow a continuous advective pathway, as some parcels are carried to the southern edge of NEC through Ekman drift (Zhang *et al.,* 2003; Lumpkin and Garzoli, 2005). During winter and spring the strong trade winds are responsible for the weakening of this current, being forced to migrate to the equator (Mittelstaedt, 1991). Regions of high Eddy Kinetic Energy (EKE) are clearly associated with this current (Lázaro *et el.,* 2005).

Mauritania Current (MC) – It is a result from the interception of NECC with the African coast. Part of its flow is derived northward, carrying warm oligotrophic equatorial water to the tropical eastern Atlantic (Mittelstaedt, 1991). Thus, the strength of this current is strongly related to the seasonal varying NECC, with about 1-month time lag (Lázaro *et al.,* 2005). MC only reaches the latitude of approximately 14ºN during winter and early spring, but due to the relaxation of the trade winds and the consequent northward displacement and strengthening of NECC, it reaches latitudes of approximately 20ºN during summer and early autumn (Figure 2.6) and it is partly responsible for the suppression of the regional costal upwelling (Mittelstaedt, 1991). Schütte *et al.* (2016a) suggested that this current is strongly associated with the formation of eddies that propagate westward in the direction of Cape Verde.

The Guinea Dome (GD) – Located southwest of the archipelago, this geostrophic cyclonic feature is defined by a (cold) dome of the isotherms, and low hydrostatic pressure (Faye *et al.,* 2015), developed due to the Ekman suction (upwelling) driven by the local wind stress curl (Richardson and Walsh, 1986; Siedler *et al.*, 1992; Yamagata and Iizuka, 1995). It exists permanently during the year and it is a constituent of the large-scale near-surface flow fields associated with the NEC, the NECC and the North Equatorial Undercurrent (Siedler *et al.*, 1992). The NECC is responsible for the variability of the position, shape, and intensity of the such feature

(Lázaro *et al.,* 2005). Thus, its signal is more evident between May and December, following a similar displacement as the NECC when it moves north-westward.
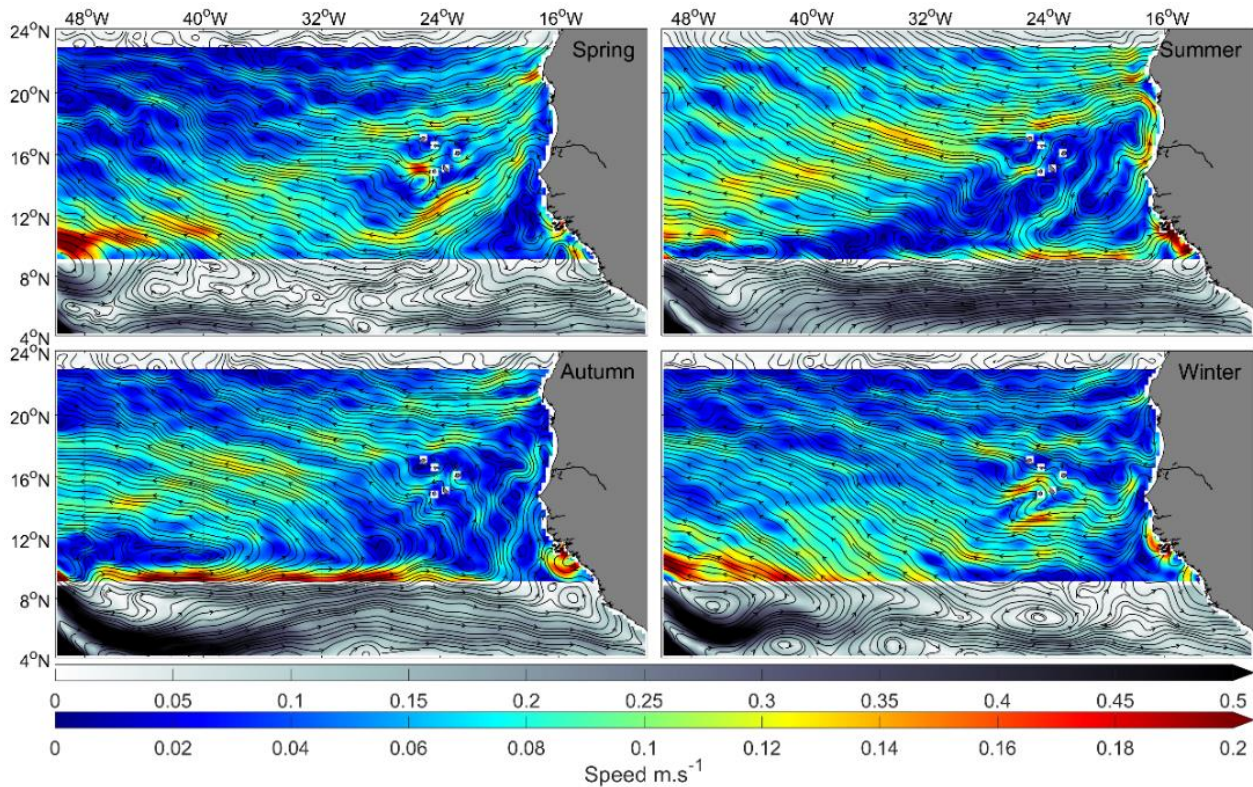
Figure 2.6 - Representation of the seasonal mean surface currents, from 2003 to 2014. Note the different colormaps. Data: GlobCurrent Geostrophic + Ekman.

Following the main large-scale surface currents description, a conspicuous seasonal signal has been documented (Figure 2.6) as the dominant aspect in the region (Mittelstaedt *et al.,* 1991; Lázaro *et al.* 2005), being mainly induced by the variability of the trade winds (Stramma and Schott, 1999).

Trade winds and the ITCZ generate large scale divergent Ekman transports along the western African coast (Faye *et al.,* 2015), leading to one of the strongest and most productive upwelling systems in the world (Ould-dedah *et al.,* 1999). Costal upwelling is permanent between 20º – 25ºN, reaching its maximum intensity during spring and autumn (Figure 2.7, Mittelstaedt, 1991; Ould-dedah, *et al*., 1999). South of 20ºN this phenomenon is conspicuous during winter and early spring (Van Camp *et al.,* 1991; Nykjær and Van Camp, 1994; Lázaro *et al.*, 2005) and is associated with a significant enhancement of biological productivity (Pelegrí *et al.,* 2006; Lathuilière *et al.,* 2008, Demarcq and Somoue, 2015), which is also partially driven by the southward transport of cold, nutrient-rich water from the CC (Mittelstaedt, 1991). The strength and seasonal oscillation of the coastal upwelling depends mainly on the alongshore wind-stress and wind-stress curl seasonal

patterns (Hagen, 2001; Pradhan *et al.*, 2006), and in the seasonal variation of the MC extension (Mittelstaedt, 1991; Siedler *et al.*, 1992; Lázaro *et al.*, 2005).
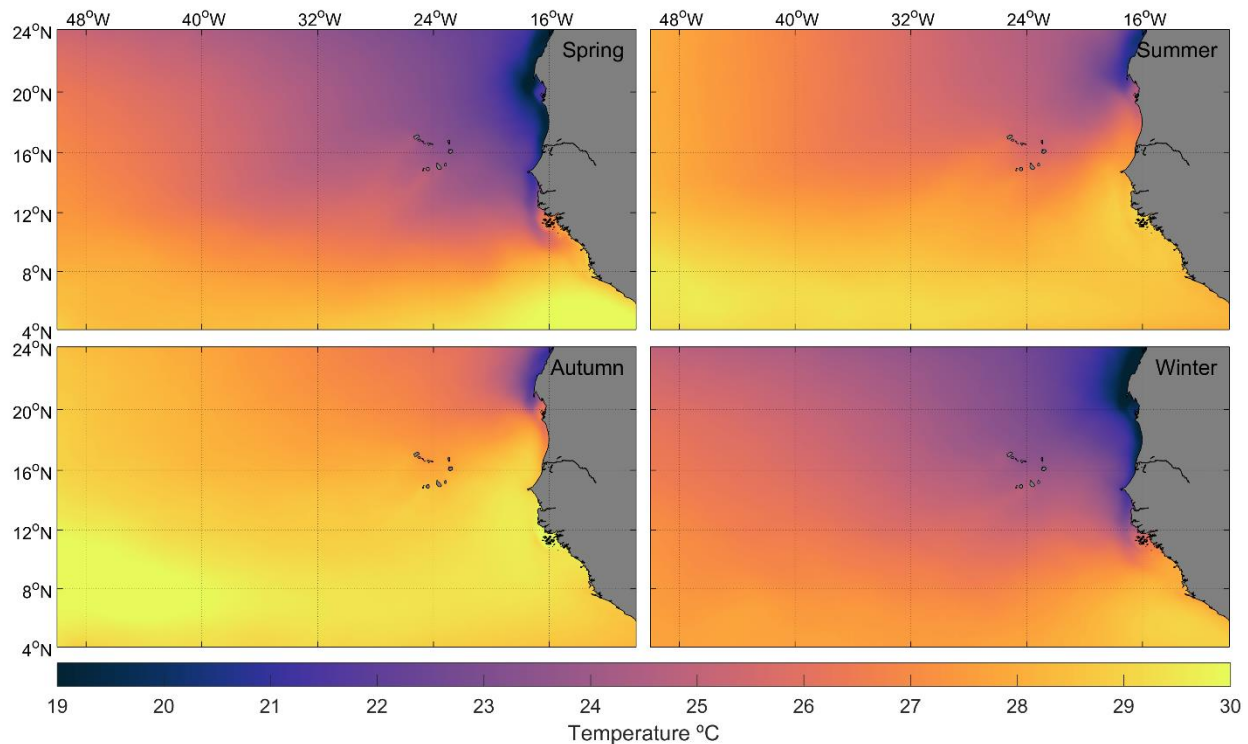
Figure 2.7 - Sea Surface Temperature seasonal means from 2003 to 2014. It is worth noting the apparent warm wake in the lee of Santo Antão and Fogo Islands.

This region experiences on of the largest Sea Surface Temperature (SST) cycles in the tropics (Faye *et al.*, 2015). The SST variation has a considerable lower amplitude in offshore waters than in coastal waters (Figure 2.8), a fact that is conspicuously related to the coastal upwelling seasonal cycle (e.g., Mittelstaedt, 1991; Van Camp *et al.*, 1991; Ould-dedah *et al.*, 1999; Marcello *et al.*, 2011). In the area of Cape Verde Islands, maximum values (29 ºC) are achieved from July to November (Figure 2.7) – coincidently with higher pigment concentrations near Cape Verde (Fernandes *et al.*, 2005) –, whilst minimum values (21 – 22ºC) are conversely seen between December and May (DGA, 2004).
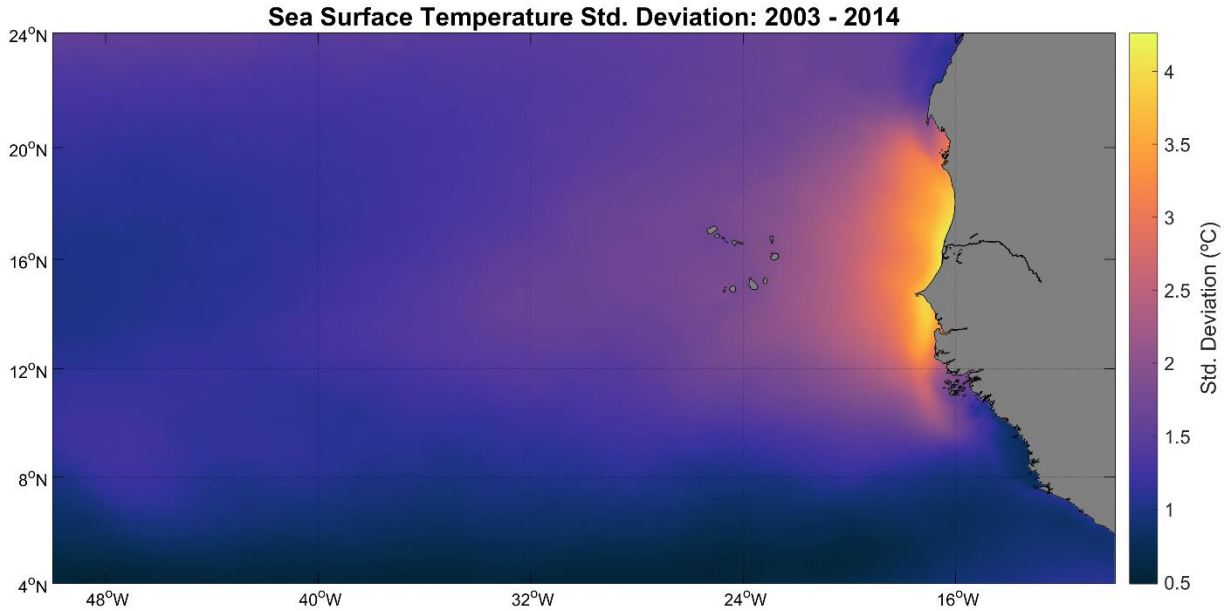
Figure 2.8 – Sea Surface Temperature standard deviation showing the effect of the seasonal variability associated with upwelling off the western African coast.

Acting as a source of organic matter, inorganic nutrients and phytoplankton in the region, it has been consistently reported the generation of giant filaments off Cape Blanc (e.g., Gabric *et al.,* 1993; Kostianoy and Zatsepin, 1996; Lange *et al.,* 1998; Pastor *et al.,* 2008; Meunier *et al.,* 2012; Pelegrí and Peña-Izquierdo, 2015). The filament can have a significant impact on the archipelago's biological productivity (Fernandes *et al*., 2005), acting as remote enrichment. This feature results from the intersection of the Mauritanian coastal upwelling system and the very complex and dynamic CVFZ, as intrinsically unstable upwelling currents interact with the Cape Verde front eddy field (Meunier *et al.*, 2012). This phenomenon seems to be responsible for the transport of cold nutrient-rich water offshore and plays a crucial part in the generation of the Cap Blanc filaments (Meunier *et al.*, 2012), which have reportedly increased their offshore spreading during the last years (Marcello *et al.,* 2011). Lastly, it is important to note that the atmospheric deposition of Saharan dust is an important source of essential and limiting nutrients (Gelado-Caballero, 2015) – such as silicon, phosphorus, nitrogen, and iron. However, only 5% of the Chl*a* variability in the region was related to the dust input (Ohde and Siegel, 2010).

3. Data Acquisition and Processing

Taking into account the inherent complexity and variability associated to eddies and other pertinent mesoscale processes, the coupling of several satellite-based remote-sensing products is considered to be the most efficient approach for the study of the Cape Verde Archipelago. It is important to note that, given the exploratory nature of such investigation, the planning and structure of the current project is directly dependent on the preliminary results. Therefore, a behaviour-oriented approach is executed, first by performing an initial characterisation of the regional setting. This preliminary investigation is defined at 10 – 50ºW and 4 – 24ºN, extending almost the entire zonal length of the Atlantic Ocean, from the western African coast to the eastern South American coast. It is important to note, however, that part of this characterisation was already described in the previous chapter. Then, the representation and analysis of sequential 8-day averages was performed, considering the recurrent period of most satellites and datasets being used (~4 days). Subsequently, simple statistical procedures were applied, along with the computation of 12-year and seasonal means. The seasonal grouping refers to the northern hemisphere (i.e., boreal seasons), such that: winter goes from January to March; spring goes from April to June, summer goes from July to September; and Autumn goes from October to December.

Once the preliminary analysis was concluded, special attention was regarded towards the eddy field around and within the archipelago. Hence, two groups of eddies were defined: the far-field eddies – those that were created outside the Cape Verde Area (hereinafter referred as CV area) but at some point intersected the delimited CV area; and the near-field eddies – those created inside CV area, whether by island-induced mechanisms or by far-field eddy-island interaction. The statistics of these two groups of eddies were further described, along with the representations of their geographical distribution and associated kinematic properties. Then, a more detailed analysis of the far and near-field eddy dynamics was conducted. Lastly, the final focus of the study was directed to the biological implications of the such physical processes.

The study period was set from 2003 to 2014 based the data availability of the selected variables (Table 3.1). Furthermore, MatLab was used for most the data download, subsampling and processing. The "cmocean" tool for MatLab was used for some plots, enabling a more realistic and effective representation of the data (Thyng *et al.,* 2016). When necessary, plots were edited in Inkscape.

Table 3.1 – Data availability from 1993 to 2016. Green and empty cells represent available and non-available data, respectively. Study period is delimited by black thick lines and represented in dark-green.

	Dataset	Year																						
		1993	1994	1995	1996	1997	1998	1999	2000	2001	2002	2003	2004	2005	2006	2007	2008	2009	2010	2011	2012	2013	2014	2015	2016
Wind	QuikScat								■	■	■	■	■	■	■	■	■	■							
	ASCAT															■	■	■	■	■	■	■	■	■	■
Currents	OSCAR	■	■	■	■	■	■	■	■	■	■	■	■	■	■	■	■	■	■	■	■	■	■	■	■
	GlobCurrent	■	■	■	■	■	■	■	■	■	■	■	■	■	■	■	■	■	■	■	■	■	■	■	■
Eddies	OpenEddy	■	■	■	■	■	■	■	■	■	■	■	■	■	■	■	■	■	■	■	■	■	■		
	Chelton and Schlax	■	■	■	■	■	■	■	■	■	■	■	■	■	■	■	■	■	■	■	■	■	■		
ADT	AVISO	■	■	■	■	■	■	■	■	■	■	■	■	■	■	■	■	■	■	■	■	■	■	■	■
Chl*a*	Aqua MODIS											■	■	■	■	■	■	■	■	■	■	■	■	■	■
SST	GHRSST											■	■	■	■	■	■	■	■	■	■	■	■	■	■

3.1. Wind

The importance of the wind as a driver for oceanic surface currents has long been well established (Pond and Pickard, 1983; Tomczak and Godfrey, 1994; Talley *et al.,* 2011). Given the nature of the mechanism in study and all that was mentioned before, wind data is undoubtedly an essential tool for the regional oceanographic characterisation at a large scale and for the investigation of the archipelago's impact in the wind dynamics at a local scale.

As such, wind speed and direction was provided by the QuikSCAT scatterometer-derived dataset (SeaPAC, 2016), considered to be an accurate representation of oceanic winds (Couvelard *et al.,* 2012). It was produced by NASA/Jet Propulsion Laboratory and distributed by the NASA Physical Oceanography Distributed Active Archive Center (PO.DAAC). This instrument was part of a "quick recovery" mission (hence the naming of the project) designed to fill the gap created by the premature loss of the NASA Scatterometer (NSCAT) aboard the ADEOS-1 satellite in June 1997 (Lungu, 2001). The scatterometer measured the wind roughened ocean surface – which is highly correlated with the near-surface wind field (Hoffman and Leidner, 2005) – through microwave pulses emitted by the rotating dish antenna at Ku-band (13.4 GHz) (Spencer *et al*., 2000). The power of the "backscattered" signal is then used for inferring the wind speed and direction. The usage of a microwave radar (an active sensor) implies that data can be retrieved under all weather and cloud conditions (Moroni *et al.,* 2013). However, there are some limitations, such as rain contaminations and high wind speed measurements. The satellite has a recurrent period

of approximately ~4 days (57 orbits) and the capacity for collecting an 1800 km-wide band. The combination of the orbital period (14.25 orbits/day) and inclination (98.62º) resulted in a remarkable 90% daily coverage of the global ice-free ocean (Moroni *et al.,* 2013).

Despite the original spatial resolution of the sensor, higher resolution is achieved through a slice composite technique from level 1 data (PO.DAAC, 2017). Thus, QuikScat data is available at 12.5 km and 25 km spatial resolution, yet with distinct levels of processing. The sparser resolution (25 km) is distributed at processing level 3, which means that the data is available at a daily or time averaged spatially fixed and uniform grid. However, the higher-resolution data (12.5 km) is only available at level 2, meaning that the data is mapped over an along-track/cross-track non-uniform swath grid (i.e. organized by swath rows perpendicular to satellite path), and each file contains data of a single satellite orbit. Despite the advantage of a high processing level, one must consider that the Cape Verde Islands are relatively small and higher pixel size (wind vector cell) results in a lower resolution. The algorithm behind the 12.5 km resolution data processing was subjected to significant improvements recently, tackling issues such as rain contaminations, sampling limitations and ambiguous direction retrievals (Fore *et al.*, 2014). Moreover, by incorporating an enhanced coastal processing method, the near-shore wind variations is now more accurate than ever before (PO.DAAC, 2017). That being said, the reprocessed QuikSCAT Level 2B Version 3.1 product is considered to be the best suited dataset for the current study. The data subsampling and download was made through the "High-level Tool for Interactive Data Extraction" website (https://podaac-tools.jpl.nasa.gov/hitide/). After download, the data was projected into a spatially uniform 12.5 km (~0.1º) resolution grid and averaged over 8 days, so that the gaps created by the satellite tracks could be minimised. This way, every place in the study area was covered at least two times. Albeit it exceeded its operational time expectancy, QuikSCAT data is only available until November 2009. Taking into consideration that most variables availability are overlapped from 2003 to 2014 (Table 3.1), a different dataset should be incorporated.

The Advanced Scatterometer (ASCAT) is a real aperture radar based instrument aboard the MetOp-A and MetOp-B polar satellites, which became fully operational in May 2007 and September 2011, respectively, and remain active to date. The satellites were launched by the European Space Agency (ESA) and are operated by the "European Organisation for the Exploitation of Meteorological Satellites" (EUMETSAT, 2015). It uses a similar system as the QuikSCAT instrument, in the sense that it measures near-surface wind properties (at 10-m above

23

the sea surface) by inferring the sea surface roughness by microwave radar. Nonetheless, this sensor differs from the QuikSCAT in technical specifications and configuration. It is composed by two sets of three fixed antennas with 45° inclination, which pulsate radar beams at a frequency of 5.26 GHz (C-band) – more robust in terms of rain contamination – on both sides of the satellite ground track, covering two 550 km-wide swaths separated by ~700 km (OSI SAF, 2016). The version 2.1 of the ASCAT (MetOp-A) wind product is provided by the Remote Sensing System organisation (RSS, 2017), which underwent a reprocessing procedure by applying a new the Geophysical Model Function (GMF), based on the Ku-band GMF (QuikSCAT) methodology. As such, ASCAT is now in better agreement with the QuikSCAT dataset (Ricciardulli, 2016), being thus the best option to fulfil the purpose of the current study. The swath files at 12.5 km spatial resolution (Ricciardulli and Wentz, 2016) were downloaded from the company's FTP server and processed with MatLab routines, made available by RSS (2017). After this, and following the same methodology as for the QuikSCAT, the data was gridded and time averaged, so that the two datasets could be merged.

- **Data Processing**

The wind itself can only have an influence in the ocean as a frictional force, which arises from the relative motion between the atmosphere and the ocean (Stewart, 2008). As such, the transfer of momentum is due to the input of energy (N.m^{-2}) by the wind in the form of wind stress. However, wind retrievals from scatterometer instruments are calibrated against the equivalent 10-m neutral wind rather than wind stress, because the latter is difficult to measure directly (Chavanne *et al.,* 2002). Thus, the wind stress (τ_{wind}) is calculated based on Gill (1982):

$$\tau_{wind} = \rho_{air} C_D W^2 \tag{1}$$

where ρ_{air} is the density of the air (1.2 kg.m^{-3}), C_D is the non-linear wind-drag coefficient – based on Large and Pond (1981), modified for low wind speeds (Trenberth *et al.*, 1990) –, and W is the wind speed at 10 m above sea surface, which in turn is calculated by the metric:

$$W = \sqrt{u^2 + v^2} \tag{2}$$

where u and v are the zonal and meridional wind components (m.s^{-1}), respectively. Another valuable parameter is the wind stress curl ($\nabla \times \tau_{wind}$). It is calculated by the Equation 3:

$$\nabla \times \tau_{wind} = \frac{\partial \tau_v}{\partial x} - \frac{\partial \tau_u}{\partial y} \tag{3}$$

where τ_u and τ_v are the zonal and meridional wind stress components, respectively. This parameter is directly proportional to the vertical water displacement in ocean's interior. Thus, for the northern hemisphere, upwelling results from positive (divergent/cyclonic) wind stress curl and downwelling results from negative (convergent/anticyclonic) wind stress curl (Talley *et al.,* 2011). Furthermore, upwelling is referred to Ekman suction, while downwelling is referred to as Ekman pumping. Lastly, the horizontal component of the wind-driven Ekman (volume) transport (M_{ek}) is calculated according to Smith (1968) and Bakun (1973):

$$M_{ek} = \frac{1}{\rho_{sw}f}\tau_{wind} \tag{4}$$

where ρ_{sw} is the reference seawater density (1024 kg.m^{-3}) and f is the Coriolis parameter, in which:

$$f = 2\Omega \sin\varphi \tag{5}$$

where Ω is the earth rotation rate (7.2921×10^{-5} rad.s^{-1}) and φ is the latitude (Stewart, 2011).

3.2. Ocean Surface Currents

Ocean surface currents are the horizontal movement of water at the oceans mixed layer, which is the upper boundary layer (or Ekman layer) and a zone of momentum exchange from the atmosphere to the sea (Tomczak and Godfrey, 1964). The varying temporal and spatial scales, in conjunction with the countless number of factors which drive the motion of the ocean's surface, makes the ocean currents to behave in a very complex manner. *In-situ* measurements are reliable but limited in spatial coverage and regularity. Satellite remote sensing, however, is an ideal tool for studying ocean surface dynamics at a large scale (Dohan and Maximenko, 2010), since it provides global observations at a regular basis. In order to assess the nature and behaviour of the oceanic currents at a regional and local scale, two similar datasets were considered.

Ocean Surface Current Analyses Real-time (OSCAR) is a NASA funded research project – operated by Earth & Space Research institute (ESR) – that provides surface current velocities (averaged over the top 30 m of the ocean) calculated from the combination of several satellite sensed datasets, these being Sea Level Anomaly (SLA)[1], Winds[2] and SST[3] (Dohan and

---

[1] Altimetry data from the AVISO multi-mission product.
[2] Special Sensor Microwave Imagers, QuikSCAT and ASCAT (MetOp-A).
[3] Weekly Reynolds Smith O.I. v2.

Maximenko, 2010). On the top of providing a near real-time global coverage of the ocean surface currents, one of the project's main objective is to improve the knowledge of the mechanisms behind the transfer of momentum between the atmosphere and the ocean (ESR, 2017a). To that end, the model calculations take into account the principles of geostrophy – calculating the pressure gradient from the SLA – and the wind driven velocity components – calculating Ekman-Stommel equations, as well as thermal wind induced currents (Hausman *et al.*, 2009). With a 5-day temporal resolution, this product extends from 1992 to present day and is spatially distributed over a 1/3º resolution grid. Substantial calibration and validation of the modelled data is regularly performed by ESR using drifter and mooring data (ESR, 2017b). The correlation coefficient between model and drifter data (for the period of 2005 to 2009) is ~0.55 for the area of Cape Verde (Annex B.1). Furthermore, the visual comparison between OSCAR's and moored zonal and meridional velocities near to the archipelago (Annex B.2) indicates a similar general pattern, though far from being identical.

GlobCurrent is another reliable product, based on the same processing principles of OSCAR. Funded by ESA Data User Element, this project relies on advanced processing tools and simulation models that used satellite[4] and in-situ[5] data for producing an optimized approximation of the global surface ocean circulation (ESA, 2015). Covering the period from 1993 to 2016, several datasets are provided, such as individual Geostrophic, Ekman and Stokes Drift current components, as well as the combined Geostrophic and Ekman currents at the surface and 15 m depth. All the datasets are available at a daily interval and at 1/4º resolution. However, one must consider that the effective temporal and spatial resolution for the combined Geostrophic and Ekman currents is of the order of 5-10 days and 50-100 km, respectively (ESA, 2015), which in turn is related with the sensor limitations of the altimetry product being used. Despite this, it remains to be a valid option, since mesoscale eddies and strong ocean currents are found at spatial scales that vary between tens to several hundred kilometres and timescales of days to years (Talley *et al.,* 2011).

Quantitative comparisons between the combined GlobCurrent, OSCAR and SVP-type drifter data[6] were performed for the period ranging from September 2012 to September 2013 at a global

---

[4] Altimetry, gravimetry, synthetic aperture radar (SAR), scatterometry and optical/passive microwaves.

[5] Drifting and moored buoys, coastal high-frequency radar, Argo floats, gliders and ship observations.

[6] This dataset is not part of the in-situ variables used for the calculation of GlobCurrent, so that the validation remains fully independent.

scale (Table 3.2). The 3-day low pass filter was applied to eliminate high-frequency ageostrophic signals which cannot be reproduced in the modelled data (ESA, 2015). Despite the minor differences in correlation, GlobCurrent is in better agreement with SVP data.

Table 3.2 - Root Mean Square (RMS) and Correlation coefficients between in-situ SVP velocities and the two current products. Adapted from ESA, 2015.

	RMS		R^2		R^2
	U	V	U	V	
Unfiltered drifter velocities					
GlobCurrent	15.1	14.9	0.67	0.62	0.65
OSCAR	16.3	15.8	0.67	0.59	0.64
3-days filtered drifter velocities					
GlobCurrent	11.3	10.9	0.75	0.76	0.73
OSCAR	12.8	11.8	0.73	0.76	0.70

Taking all things into consideration, the GlobCurrent combined currents proved to be the best option for this study for two main reasons: higher temporal and spatial resolution (even though it is achieved by interpolation); and higher scores in the correlation between *in-situ* data. The data subset and download was performed in Matlab through GlobCurrent's OpenDAP server (http://www.ifremer.fr/opendap/cerdap1/globcurrent/). These files were already provided at processing level 4, which means that no further data mapping or compilation was required.

- **Data Processing**

The Eddy Kinetic Energy (EKE) for surface currents is a valuable measurement for the estimation of mesoscale variability, since it is directly linked to the input of kinetic energy exclusively induced by eddies (e.g., Lázaro *et al.,* 2005; Calil *et al.,* 2008; Chaigneau *et al.,* 2008; Lathuilière *et al.,* 2008; Yoshida *et al.,* 2010; Jia *et al.,* 2011; Caldeira *et al.,* 2017). EKE was first derived from ship drift observations, but in current times it is easily constructed from surface drifter velocities (Richardson*,* 1983; Frantantoni, 2001) and from surface velocities derived from altimetry products (Talley *et al.,* 2011) – as it is the case for the current dataset. As such, this parameter was computed using the following Equation (6):

$$EKE = \frac{1}{2}(u^2 + v^2)$$

(6)

where u and v correspond to the zonal and meridional current velocity components, respectively.

3.3. Eddies

Given the fact that mesoscale eddies have distinctive characteristics that can be used for this purpose – such as temperature anomalies (Caldeira *et al.,* 2002; Sangrà *et al.,* 2004; Caldeira *et al.,* 2014), surface roughness signature (Fu and Holt, 1983; Yamaguchi and Kawamura, 2009; Karimova, 2009), enhanced levels of primary production (Arístegui *et al.,* 1997; Basterretxea *et al.,* 2005; Gaube *et al.,* 2013), sea surface elevation/depressions (Chelton *et al.,* 2011; Schütte *et al.,* 2016a), among others (Munk *et al.,* 2000; Calil *et al.,* 2008; Jia *et al.,* 2011) – one may arrive to the false assumption that autonomous methods for eddy detection and tracking are easily achieved. The fact is that only altimetry can provide a regular and reliable monitoring capability for mesoscale eddies, since it performs well regardless of the cloud cover and oceanic conditions (Robinson., 2010). Still, altimetry-based tools are susceptible to errors, because it attempts to detect the presence of three-dimensional features using sea surface information that is subjected to a variety of processes other than eddies (Faghmous *et al.,* 2015a). That being said, two very similar altimetry-based products were considered and are further discussed.

The "Mesoscale Eddies in Altimeter Observations of SSH" dataset (hereinafter CSS11) was produced by Dudley Chelton and Michael Schlax at the Oregon State University (Chelton and Schlax, 2017). It relies on the usage of a SLA dataset (DT-2014 MSLA) provided by the Archiving Validation and Interpretation of Satellite Data in Oceanography (AVISO) to identify and determine eddy parameters, such as its nature (cyclonic/anticyclonic), swirl speed, amplitude and radius (Chelton *et al.,* 2011). It is based on the premise that an eddy must be a propagating, compact and coherent structure in the space-time Sea Surface Height (SSH) fields (Schlax and Chelton, 2016). The latest version of this product is based on Williams *et al.* (2011) method, which defines an anticyclonic (cyclonic) eddy by first finding the local SLA maximum (minimum) and then connecting all the adjacent pixels that satisfy a set of five conditions[7] (Chelton *et al.,* 2011) and in which the corresponding SLA lies above a sequence of successively decreasing (increasing) thresholds (Schlax and Chelton, 2016). Despite its reliability, only eddies with a minimum amplitude and lifetime of 1 cm and 4 weeks, respectively, are retained. This is a big disadvantage since, according to Schütte *et al.* (2016a), the average eddy lifetime in the study area varies between

---

[7] SLA values for each pixel must be above or below a given threshold; The delimited area of an eddy must be comprised between a minimum of 8 and a maximum of 1000 pixels; A local maximum/minimum must exist; The amplitude (SLA gradient) must be at least 1 cm; The distance between any pair of points cannot exceed a specified maximum.

24 and 32 days. The latter authors also suggest that some eddies may disappear from one timestep to another – due to the separation of satellite ground tracks – driving this kind of algorithms to falsely identify lost eddies as new. Nonetheless, the most limiting factor of this dataset is the occasional large jumps in eddy locations associated to the changing of a 7-day to daily SSH sampling frequency (Chelton and Schlax, 2017). Such jumps make eddy trajectories to be inaccurate, making this product unreliable.

Keeping that in mind, an alternative dataset should be considered. Faghmous *et al.* (2015a) presented and made publicly available the OpenEddy tool. It differentiates from most of the eddy detection products in the sense that, besides providing a daily dataset containing eddy features and trajectories, the authors also provide the eddy detection and tracking source code (in Python and MatLab) so that the procedure can be carried based on the user's research purpose. Similarly to CS11, Faghmous *et al.* (2015a) product relies on daily SLA maps from AVISO. Nevertheless, it strives to be as threshold-free as possible, since the only obvious limitation is related to the minimum eddy size (4 pixels, which corresponds to ~30 km radius), which in turn is intrinsically related to the SLA product's resolution. Another (and possibly the biggest) advantage of this algorithm is the ability to search and find prematurely terminated eddies. This is achieved by searching for eddies with the same characteristics (size, amplitude, etc.) for a user-specified number of time-steps before terminating the track. Then, the search radius is attributed to the maximum translation distance of that eddy, by estimating its expected propagation speed (Faghmous *et al.,* 2015a). Nonetheless, it should be noted that the susceptibility to error in associating supposedly terminated eddies to interpolated tracks increases with the number of associated time-steps (Faghmous *et al.,* 2015a).

The biggest disadvantage of this tool is related with the eddy detection method. Considering that the geostrophic flow around eddies follows the closed contours of SLA, this algorithm identifies an eddy by determining the outermost closed contours of SLA containing a single maximum or minimum extreme (Figure 3.1). This can contribute to an overestimation of the eddy's size and may also lead to the cancelling of small features that are close to each other, making the eddy identification less robust than CSS11 latest version. Despite this, the algorithm is still capable of recovering 96.4% of features identified by domain experts (Faghmous *et al.,* 2015a).

All things considered, the eddy tracking was performed using the OpenEddy MatLab scripts (https://github.com/jfaghm/OceanEddies) and an already processed dataset containing all

mesoscale eddy features that were at least 4 grid cells large (Faghmous *et al.,* 2015b). The tracking procedure was constrained to the following conditions: every eddy, regardless of the lifetime, was included in the analysis; the minimum area was set to the lowest possible (radius of ~30 km); no threshold was set regarding the amplitude; and the tolerance number of timesteps in which a terminated eddy can be traced was set to 3 days – built on the assumption that an island-induced eddy takes on average 3 days to fully rotate on itself (Sangrà *et al.,* 2005; 2007, Barton, 2001). Lastly, the final dataset was transformed into a CS11-like format to simplify further analysis.
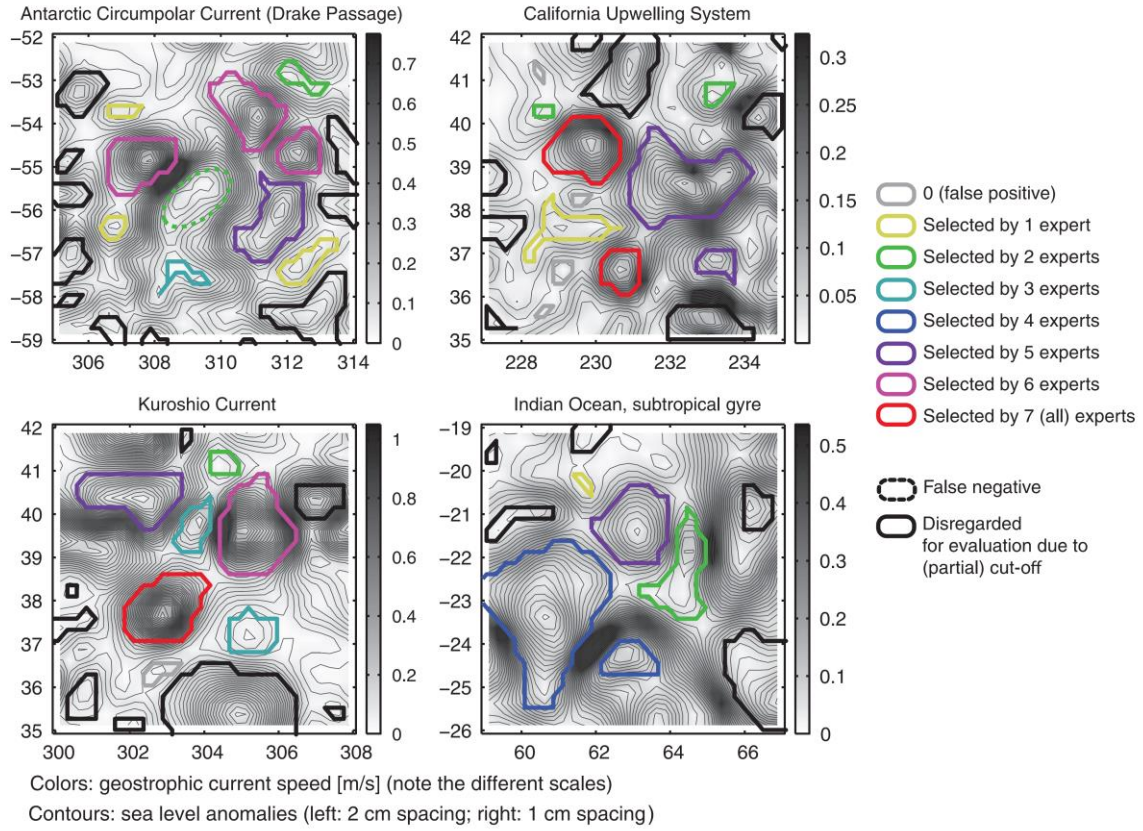
Figure 3.1 - The mesoscale eddies contours identified by the OpenEddy algorithm. Colors represent the number of experts that validated each feature. Retrieved from Faghmous *et al.* (2015a).

From Figure 3.1 one may observe that most eddies detected by the algorithm do not necessarily have a perfectly circular shape to be considered as such. Thus, the algorithm determines the eddy radius (R) as a function of the area (A) – i.e., the radius of a circle with area equal to that within the closed contour of SSH – following Equation (2):

$$R = \sqrt{\frac{A}{\pi}} \qquad (7)$$

The eddy amplitude is also determined by the algorithm as the difference in height between the SLA extremes and is always given has an absolute value. The combination of the two previous parameters is then used for the determination of the geostrophic swirl speed. However, an issue was detected regarding this parameter, which is further discussed in Chapter 5.2. Lastly, the travelled distance (T_D) and translation speed (c) are two important parameters for the current study, but were not included in the OpenEddy algorithms. Thus, a MatLab script was created for the calculation of such parameters, using the coordinates of the detected eddies. The travelled distance is computed using the following Equation 8:

$$T_D = \frac{\pi.r}{180} \times \cos^{-1}(\sin\varphi_a.\sin\varphi_b + \cos\varphi_a.\cos\varphi_b.\cos\Delta\lambda) \tag{8}$$

where r is earth's radius (6378 km), φ_a and φ_b are the latitudes of point a and point b, respectively, and $\Delta\lambda$ is the longitudinal difference between both points (Movable Type Scripts, 2017). Subsequently, the eddy propagation speed (c) was estimated following Equation 9:

$$c = \frac{T_D}{\Delta t} \tag{9}$$

where Δt is the time interval between point a and point b.

3.4. Absolute Dynamic Topography

The usage of altimetry-based products is fundamental for this study. The principle behind altimetry-sensed measurements is very similar to the wind scatterometer. However, instead of "sweeping" an area and relying only in the backscattered signal's power, the sensor measures the shape and more importantly the signal's travel time, estimating the distance of the satellite to the point directly below it – known as Nadir (Robinson, 2010). Albeit the eddy detection and tracking algorithms didn't require this dataset, it is still essential to include this parameter in order to access its variability in space and time, and to facilitate the study of individual eddies. For this reason, the AVISO Absolute Dynamic Topography (ADT) dataset (DT-MADT) was downloaded from the Copernicus Marine and Environment Monitoring Service[8]. It is part of the Ssalto/DUACS system, that processes data from all altimeter missions (Saral, Cryosat-2, Jason-1&2, T/P, Envisat, GFO,

---

[8] http://marine.copernicus.eu/services-portfolio/access-to-products/?option=com_csw&view=details&product_id=SEALEVEL_GLO_PHY_L4_NRT_OBSERVATIONS_008_046

31

ERS-1 & 2 and Geosat) in an attempt to provide a consistent and homogeneous dataset for various uses (AVISO, 2015). Furthermore, the combination of several altimetry datasets into one single product considerably improves the capacity for detecting mesoscale features such as fronts, eddies and even filaments (Pascual *et al.,* 2006)

The ADT is the sum of the SLA and the Mean Dynamic Topography (MDT) (Figure 3.2; Mertz *et al.,* 2017), or in other words, ADT corresponds to the SSH, but with respect to the geoid (GOCE DIR-R4), because the SSH is referenced to the ellipsoid. The ADT is a relevant parameter for the computation of seasonal and annual means. For the identification of single features, however, the SLA is the most adequate parameter to use, since it represents the absolute signal variation from the time-averaged signal. There are two ways of computing the SLA: one is with respect to the ellipsoid, which corresponds to the SSH deviation from the Mean Sea Surface (MSS); another is with respect to the geoid, which corresponds to the ADT deviation from the MDT. Regardless of the method, the anomaly signal remains the same as long as the correct mean is used as a reference. Thus, the SLA was computed using the 12-year MDT previously calculated from the ADT field.
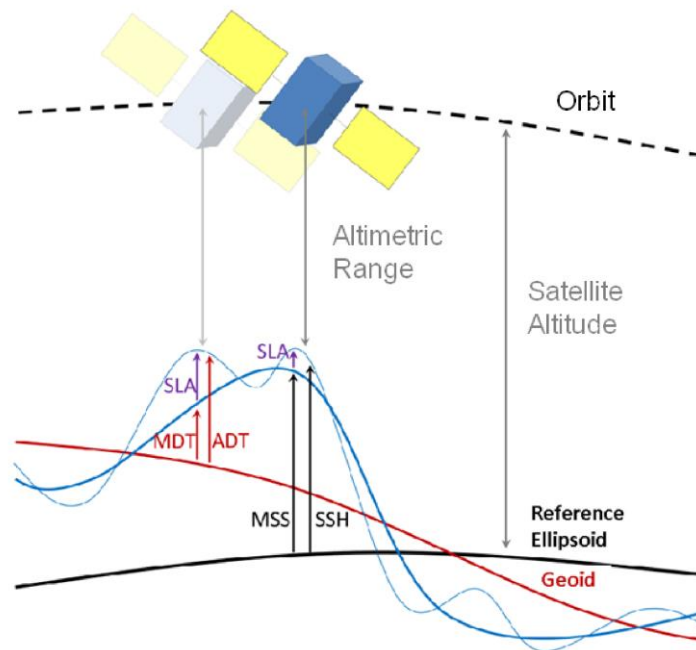
Figure 3.2 - Altimetry principles. Retrieved from Mertz *et al.* (2017).

3.5. Chlorophyll *a*

In the interest of determining the biological impact of the physical mechanisms being studied, as well as the remote-enrichment that may reach the Cape Verde Islands from the African coast (Fernandes *et al.,* 2005; Lathuilière *et al.,* 2008), monthly and 8-day averaged surface Chl*a* satellite observations were retrieved from the "OceanColor" server (https://oceandata.sci.gsfc.nasa.gov/MODIS-Aqua/Mapped/) with a 4.63-km spatial resolution. Chl*a* is the most important pigment in the respiration process of photosynthetic organisms, such as phytoplankton (Talley *et al.,* 2011). It absorbs mostly blue wave light (440 nm) and reflects the green. This is called the blue/green ratio and can be used as a proxy for determining primary production (Robinson, 2010; Gove *et al.*, 2016). However, this technique relies on passive sensors, which in turn are constrained by cloud coverage (Caldeira *et al.,* 2014). This is a significant limitation for this particular study, since Cape Verde is often under cloudy conditions due to the seasonal positioning of the ITCZ (Fernandes *et al.,* 2000; Karstensen *et al.,* 2015). Furthermore, it is important to note that the overestimation of Chl*a* concentration may occur – provoked by the presence of aerosols and dust load in the atmosphere, and suspended sediments in surface water (Helmke *et al.,* 2005; Tilstone *et al*., 2011). This dataset was recorded by the Moderate Resolution Imaging Spectroradiometer (MODIS) instrument flying aboard NASA Aqua satellite. It has a viewing swath width of ~2330 km in a sun synchronous polar orbit, providing an almost complete global coverage in one day (Savtchenko *et al.,* 2004).

3.6. Sea Surface Temperature

Lastly, SST was provided by the Group for High Resolution Sea Surface Temperature – a group composed by several international partners that assembles and delivers SST data obtained from 10 different satellite sensors (GHRSST, 2017). It offers a wide variety of spatial resolutions, from infra-red high-resolution instruments limited by cloud cover, to microwave coarser-resolution instruments with little limitations (Kaiser *et al.*, 2012). It is intended to be used as an auxiliary dataset for eddy identification, considering that anticyclonic (cyclonic) eddies have a distinct warm (cold) SST signature at its core (Robinson, 2010). It is also a valuable tool for the regional oceanic characterisation, since it can detect major mesoscale features, such as fronts, upwelling episodes and filaments that may originate at the Mauritanian coast (e.g., Mittelstaedt, 1983; Van Camp *et al.,* 1991; Gabric *et al.,* 1993; Barton *et al.,* 1998; Lathuilière *et al.,* 2008; Meunier *et al.,* 2012).

4. Results

Considering the exploratory nature of the current study, only the most relevant results are presented in this section. Further supplementary material – such as sequential 8-day average plots for wind, current, ADT, Chl*a*, and SST – was produced in order to observe the mesoscale variability in space and time. As part of a preliminary analysis, these results are extremely relevant, in the sense that it determined with great extension the planning and execution of the study. However, given the substantial number of plots (and the digital memory size), only the SLA and eddy trajectories 5-day sequential plots are included in digital format as supplementary material.

In the first part of this chapter a general approach was performed, converging into a more detailed characterisation along the process. Thus, the initial analysis is focused on the 12-year annual mean and seasonal description of the regional eddy signatures. Secondly, a zoom in approach is conducted in order to characterise the eddy field within and around the archipelago. At this stage, special attention is given to the geographical distribution and descriptive statistics of the eddy kinematic properties. Subsequently, far-field eddies that are generated at the Mauritanian coast and move westward into the Cape Verde area are assessed, with the main objective of determining spatial and temporal patterns, as well as the island-eddy interaction. For that, specific eddy trajectories are presented and further described. Then, following the same approach as the latter, the near-field eddy characterisation is conducted. Lastly, the local biological realm is characterised, along with the main mechanisms supporting it – i.e., remote enrichment and IME.

Different eddy-lifetime thresholds were used, depending on the nature of the analysis being performed. It is very important to filter the spurious from the most relevant eddies and still have a sufficiently large population to execute a robust geographical and statistical characterisation. Conversely, many eddy trajectories plotted in a map can superimpose each other, masking important patterns such as their origins and evolution in space and time. A series of thresholds were tested (1, 7, 30, 60 and 90 days; Annex C: and Annex D:) in order to find the ones that, without compromising the most relevant signals and patterns, could be used for the two main analysis. As such, a 1, 30 and 60-day thresholds were set for the descriptive statistics (and respective graphical representations), for the eddy kinematic geographical distribution and for the characterisation of the far and near-field eddies dynamics, respectively.

4.1. Regional Eddy Signatures

For the purpose of inferring the eddies dynamic signature in the regional oceanographic background, particularly their geographical and seasonal patterns, the 12-year annual and seasonal EKE field is further described. EKE is one of the most elementary parameters in this kind of studies, mainly because the representation of such parameter makes the main eddy hotspots and pathways obvious and easy to detect (Figure 4.1 and Figure 4.2). Furthermore, EKE signals represent the energy exclusively induced by eddies in the environment, but it does not discriminate eddy hotspots from pathways. Only the intensity and the frequency of the such features can be traced. Given the fact that an area of extremely elevated EKE levels is present between the 4 and 9ºN, two different areas and respective colormaps were defined. A grey-scale colormap with a bigger range was used for the southernmost and northernmost area. These areas are of less interest and are hereinafter referred as the "grey area". As for the main study area, a "rainbow" colormap with a smaller range was used.

The most evident feature in the 12-year mean EKE map (Figure 4.1) is easily identified as a transversal band of high EKE values, varying from ~40 to more than 100 $cm^2.s^{-2}$. It extends the entire tropical basin (16 – 50ºW), from Cape Blanc to the south-westernmost region. Within this band, the highest values are detected in the proximity of Cape Blanc and north of the windward islands, with values reaching ~100 $cm^2.s^{-2}$. The latter signal is characterised by an elongated shape, and although it is still within the major transversal band of high EKE, one should not neglect the possibility of an independent pathway for far-field turbulent mesoscale features.

Another area of great interest is located west of Fogo Island (25ºW), in the leeward group of islands. This feature is detached from the previous zonal band, because it is quite isolated from the latter and its signal is confined into a circular area. It has approximately 1º (~111 km) diameter and presents EKE values in the order of ~100 $cm^2.s^{-2}$.

Two other areas of significant EKE values are shown: one located in the African coast at 11ºN latitude; and another in the opposite side of the regional study area. However, due to their locations, these areas are not relevant for the present study. In the "grey area", a significant EKE signal covers the entire zonal extend, with values reaching more than 1000 $cm^2.s^{-2}$ in the western section.
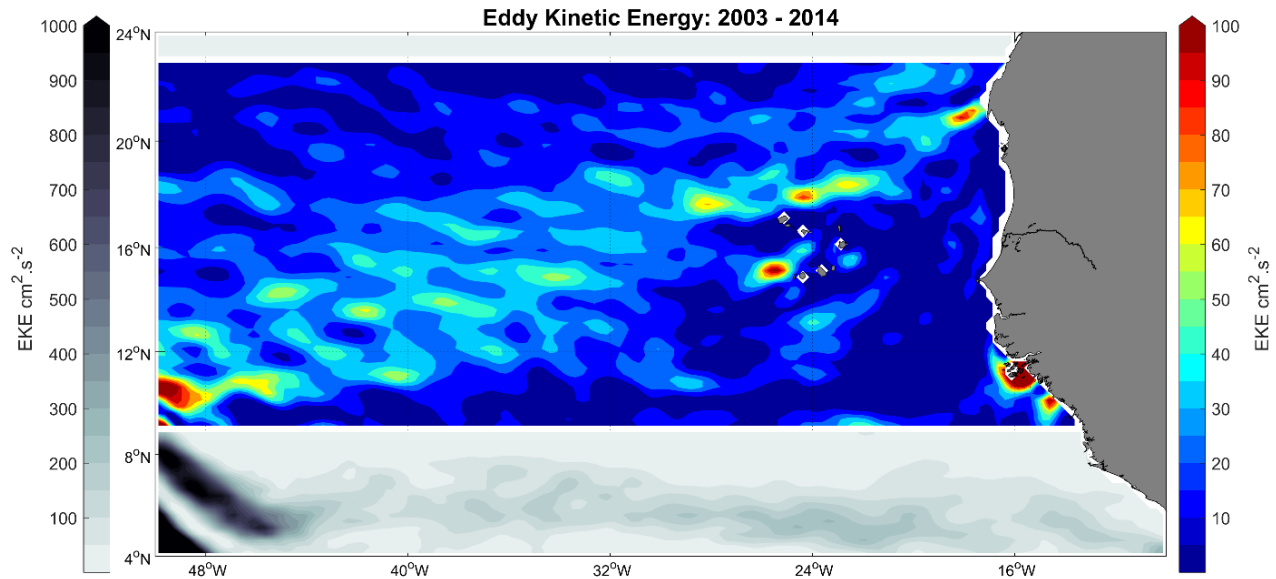
Figure 4.1 – Mean EKE for the 12-year study period in the region of Cape Verde.

In respect to the seasonal EKE signal, Figure 4.2 shows significant differences between the four seasons. A characterisation for all seasons follows:

Spring: the transversal band is not so pronounced as in the annual mean, but high values are still present near Cape Blanc and north of the windward islands (~140 and ~80 cm^2.s^{-2}, respectively). In this season, the most notable features are around the Cape Verde Archipelago. The previously described confined area west of Fogo Island presents a strong EKE signal, with values around 160 cm^2.s^{-2}. Furthermore, it is possible to observe what it seems to be a major eddy pathway south of Fogo Island with values between 60 and 140 cm^2.s^{-2}. The latter has an initial south-westward direction (from approximately 20ºW 15ºN to 26ºW 10ºN), turning westward in the final segment (for more 3º longitude). In the south-westernmost part of the figure, an extremely high EKE signal appears, but due to its location is not relevant for the current study.

Summer: It is during this season that the transversal basin-wide band of high EKE is more evident, showing its maximum seasonal EKE values varying from 80 to 140 cm^2.s^{-2}. Features previously identified around the archipelago diminishes in area and strength or even disappear, as it is the case of the circular area west of Fogo Island, and the case of the major pathway previously identified south of the archipelago, respectively. Conversely, new features arise in the African coast. One band is located near Cape Vert, following very closely the coastline in a northward orientation. Another band is located up north, detaching from the coastline and seemingly merging the quasi-permanent signal at Cape Blanc.

Autumn: the background EKE signal decreases dramatically in the main study area, being the basin-wide band the most evident feature, especially northward of the windward islands. An extremely strong signal appears in the south of the regional study area, showing evidences of the "grey area" northward seasonal migration. Another signal appears in the coastal zone of Guinea-Bissau, being of less interest due to its location.

Winter: The transversal band of high EKE signal disappears almost completely. The elongated signal north of the windward group is still present, with values around 60 $cm^2.s^{-2}$, reinforcing the hypothesis of a pathway independent from the transversal band. High EKE signals (~100 $cm^2.s^{-2}$) reappear around the archipelago, more specifically between the windward and the leeward group, and downwind of the Fogo Island. It is difficult to define these signals as distinct eddy pathways or places of origin, due to the elongated shapes. An interesting feature extending the oceanic area between the African coast and the archipelago is the apparent eddy trail, with values around 60 and 80 $cm^2.s^{-2}$. It originates near Cape Vert and then divides in two branches south-east of the archipelago, which then seemingly appear to merge the previously described areas (north and south of the leeward Island).
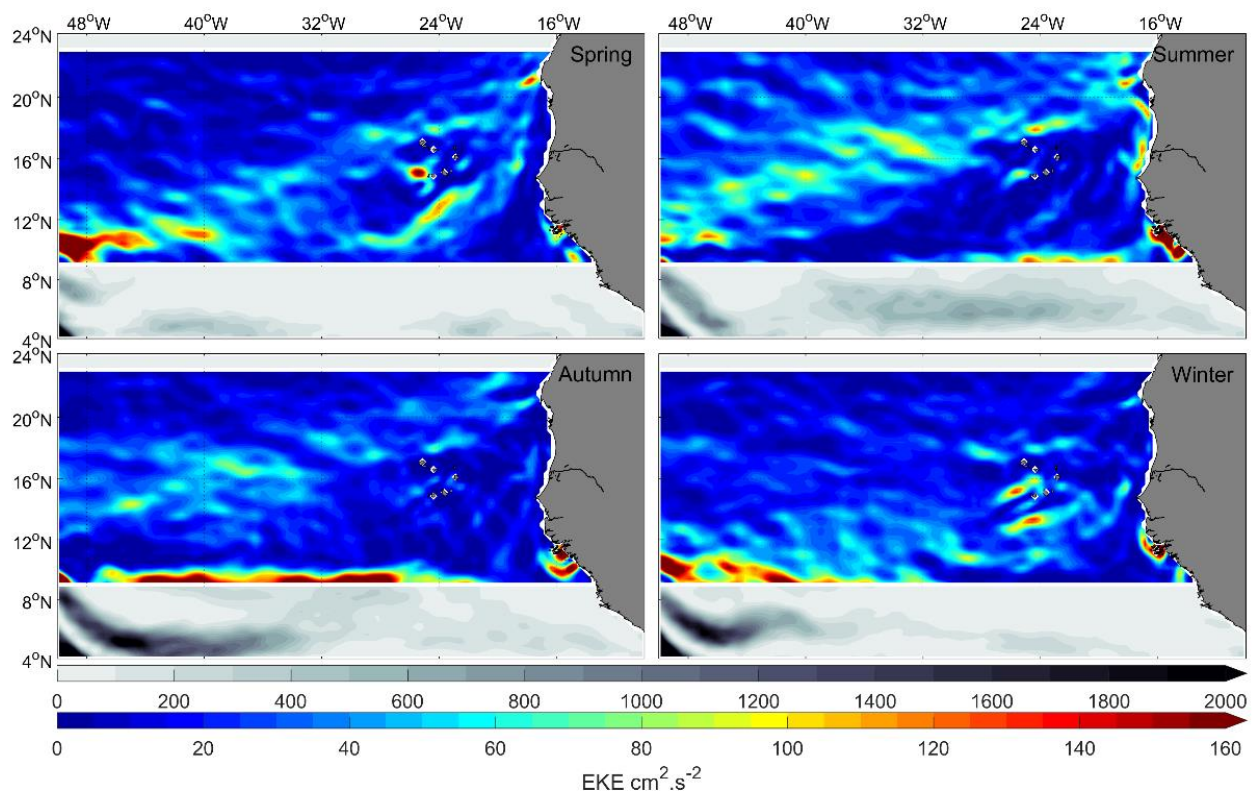
Figure 4.2 – Mean seasonal EKE for the 12-year study period in the region of Cape Verde.

4.2. Eddy Statistics and Geographical Distribution

In this section, the main characteristics of the eddy field within and around the archipelago are presented, together with the eddy kinematic properties and respective statistics. Two geographical areas are defined: the general study area (hereinafter referred as outside area) is set between 32 – 13ºW and 9 – 23ºN; and the Cape Verde area (hereinafter referred as CV area), is set to be at approximately 2º (~222 km) distance from the nearest islands, covering the area between 27 – 21ºW and 13 – 19ºN. Although the general study area covers a significantly broader area, it is the coastal area that deserves special attention – since most of the far-field eddies are generated there. Nevertheless, CV is the area of greatest interest. The statistical graphical representation of the eddy kinematic properties (histograms, upper-tail cumulative histograms and boxplots) follows the previously described eddy classification, in which the upper panel includes all eddies (regardless of lifetime) that were created inside the CV area; and the lower panel includes exclusively the ones that were created outside CV, but still within the study area. Furthermore, eddies are classified in three main groups, based on minimum lifetime: short (< 30 days), medium (≥ 30 days) and long-lived (≥ 60 days) eddies.

A total number of 14822 eddies are identified between 2003 – 2014 in the study area, in which 2282 (15 %) are created in CV (Table 4.1). The polarity ratio remains evenly distributed for the study area, whereas in CV area anticyclonic eddies seem to be dominant over cyclonic eddies, increasing its dominance concurrently with the threshold's increase. Expectedly, the total number of eddies decreases significantly with the threshold's increase: 50%, 86% and 96% of the total population is lost when applying a 7, 30 and 60-day threshold, respectively (Table 4.1).

Table 4.1 – Number of eddies identified per minimum lifetime.

		Total (rate)	Cyclonic Eddies (%)	Anticyclonic Eddies (%)
All eddies	Study Area	14822 (1235 yr^{-1})	7407 (50 %)	7415 (50 %)
	CV Area	2282 (190 yr^{-1})	1118 (49 %)	1164 (51 %)
≥ 7 days	Study Area	8006 (667 yr^{-1})	4002 (50 %)	4004 (50 %)
	CV Area	1433 (119 yr^{-1})	690 (48 %)	743 (52 %)
≥ 30 days	Study Area	2101 (175 yr^{-1})	1052 (50 %)	1049 (50 %)
	CV Area	452 (38 yr^{-1})	217 (48 %)	239 (52 %)
≥ 60 days	Study Area	676 (56 yr^{-1})	330 (49 %	346 (51 %)
	CV Area	151 (13 yr^{-1})	71 (47 %)	80 (53 %)

The exponential pattern is well represented in Figure 4.3, where red (anticyclonic) and blue (cyclonic) bars have a 7-day interval. Through the normal and the upper-tail cumulative histograms it is possible to observe that both areas follow a similar behaviour, and that the cyclonic/anticyclonic ratio is in equilibrium. Nevertheless, an initial ~10% difference is present between the two areas, as 70% and 80% of the CV and outside observations, respectively, is concentrated in the first 4 weeks. The boxplots confirm the previous observations, as CV eddies have on average slightly higher lifetime expectancy that the outside eddies (19.62 and 15.18 days, respectively; Table 4.2). Still, the maximum eddy lifetime recorded inside CV area was almost 250 days, while for the outside eddies it reached ~370 days.
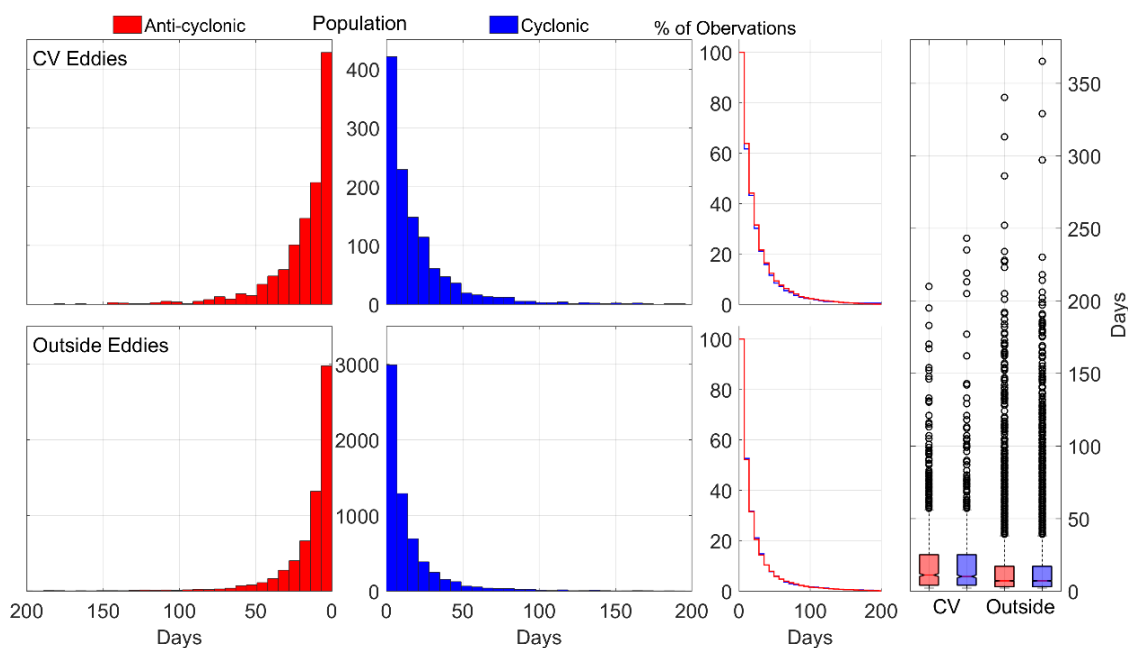
Figure 4.3 – Lifetime statistical distribution. From left to right: Histograms, representing the number of eddies (two left panels); upper-tail cumulative histograms, representing the percentage of observations (third panel); and boxplots (forth panel).

As the threshold increases to 7, 30 and 60 days, the percentage of CV eddies in relation to the entire study area also increases to 17 %, 21 % and 22 %, respectively (Table 4.1). These results are quite significant, since CV area accounts for only 16% of the total study area. The latter can be easily seen in Figure 4.4, which aims to assess eddy hotspots, as well as the prevailing eddy lifetime associated with such areas – i.e., short, medium and long-lived eddies.

From a preliminary analysis it seems obvious that, as the lifetime threshold increases, the number of eddies originating in the coastal area loses its dominance to the CV area. Regarding all eddies (≥ 1day lifetime), some hotspots are evident near Cape Blanc and in the southernmost

African coastal area, with values in the order of 200 and 170 – 220 eddies, respectively. Within the CV area, most of the boxes near the islands have a record of approximately 80 – 100 new eddies, which is significant but still not far from the background signal. For the 7-day threshold, however, the geographic patterns start to shift. The Cape Blanc area is still the main eddy hotspot, with ~110 new eddies, whilst the southernmost coastal area loses most of its significance. The CV area retains most of the eddies seen in the previous threshold, becoming more highlighted. When applying a 30-day threshold the result is even more evident. The area near Cape Blanc is close to the background values, with the generation of only ~20 eddies. The western African coast, especially near Cape Vert, shows some signals of long-lived eddies generation (17 – 24). The CV area, however, presents a considerable number of eddies generated in the lee of Santo Antão (~30) and Fogo (~27) islands. Finally, the 60-day threshold reduces significantly the number of eddy origins, as most of the background signal weakens. The most distinctive areas identified in the 1 and 7-day thresholds are lost, while the areas in the downwind regions south of Santo Antão and Fogo islands become even more pronounced. The area between Cape Vert and Cape Timiris also shows evidences of long-lived eddy generation, though not so evident as in CV area.
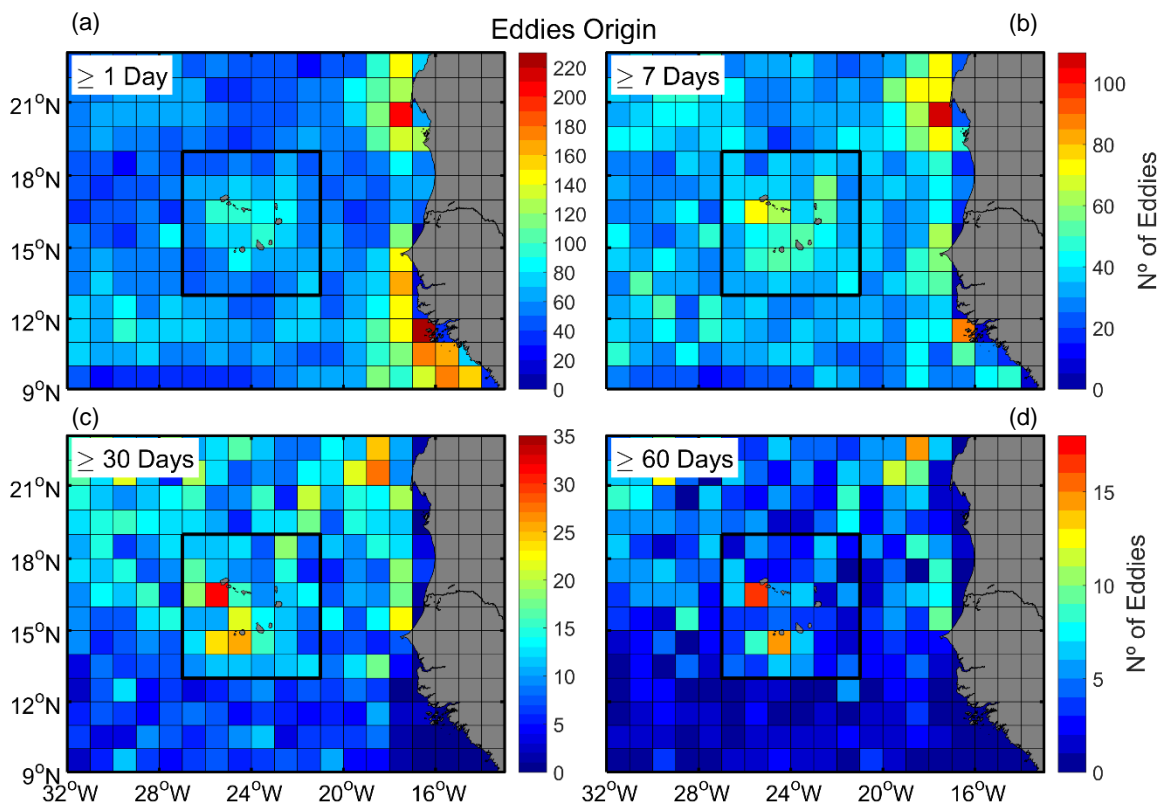
Figure 4.4 – Geographical distribution of the number of eddies generated in every 1º × 1º box, filtered per lifetime threshold. Black thick lines represent the CV area.

Regarding the eddy origins seasonal patterns, a brief characterisation is further presented, taking only into account medium and long-lived eddies. The most obvious patterns presented in Figure 4.5 are located in the lee of the two highest islands – Santo Antão and Fogo. Spring seems to be the most homogeneous season – especially in CV area – with values between 5 and 9 evenly distributed in the area around the islands. During summer, however, the signal is concentrated in the lee of Santo Antão and Santiago Islands, while at the Mauritanian coast the signal expands meridionally in 3°. A similar pattern is present in Autumn, but the area southwest of Fogo Island becomes the dominant region – with the generation of 11 eddies –, while the area south of Santo Antão remains unchanged and the area between the windward and leeward groups reaches its maximum recorded values. Lastly in winter, the area near Cape Vert, Cape Blanc and south of Fogo Island have the highest number of eddies generation – these being 9, 9 and 12, respectively.
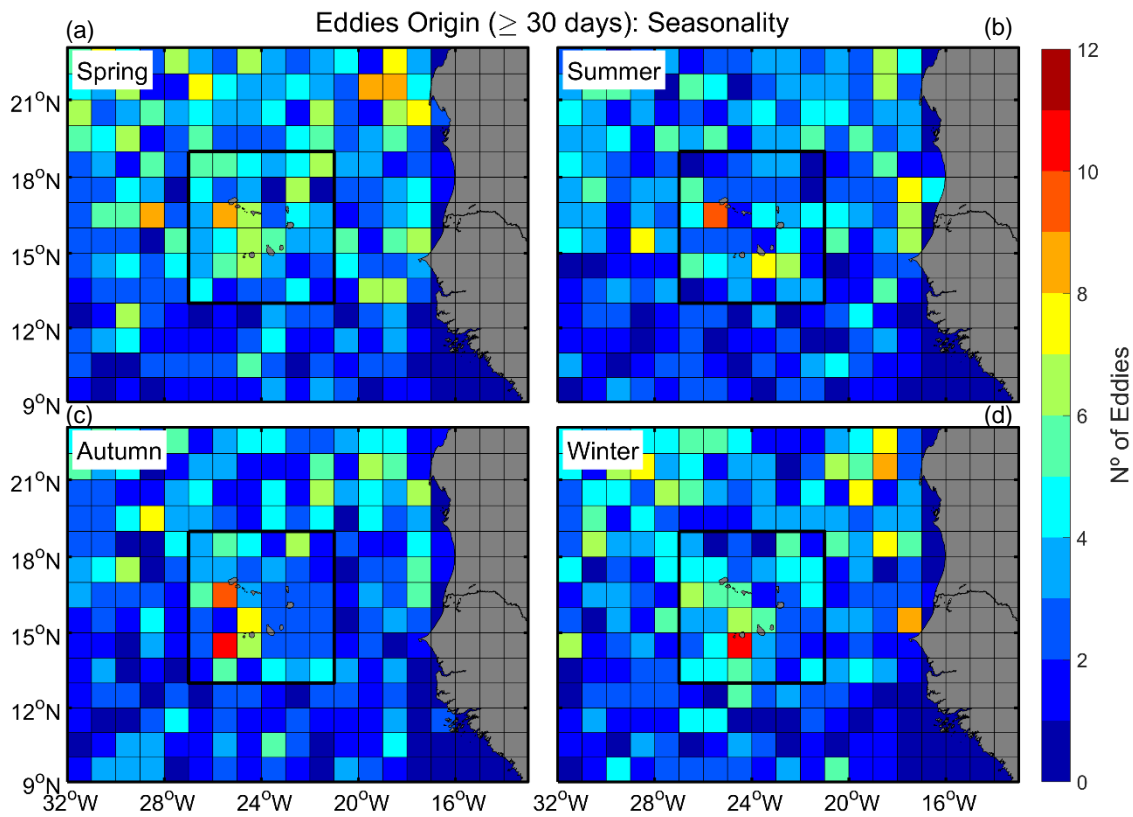
Figure 4.5 – Geographical distribution of the number of medium and long-lived eddies (≥ 30 days lifetime) generated in every 1° × 1° box, filtered per boreal seasons. Black thick lines represent the CV area. Eddy generation distributed along the boreal seasons.

4.2.1. Eddy Kinematic Properties

The study of the eddy kinematic properties is essential in order to understand their nature and behaviour. As such, the geographical distribution of the main eddy parameters is represented in Figure 4.6, in which every box represents the average value of all eddies generated there. Along with the characterisation of the latter, the eddy parameter descriptive statistics (Table 4.2) and respective graphical representations are also introduced. It is important to note that the geographical representation of such properties only includes eddies that have a minimum lifetime of 30 days (7 and 60-day representation in Annex E:), but the descriptive and graphical statistical characterisation includes all eddies, regardless of the lifetime.
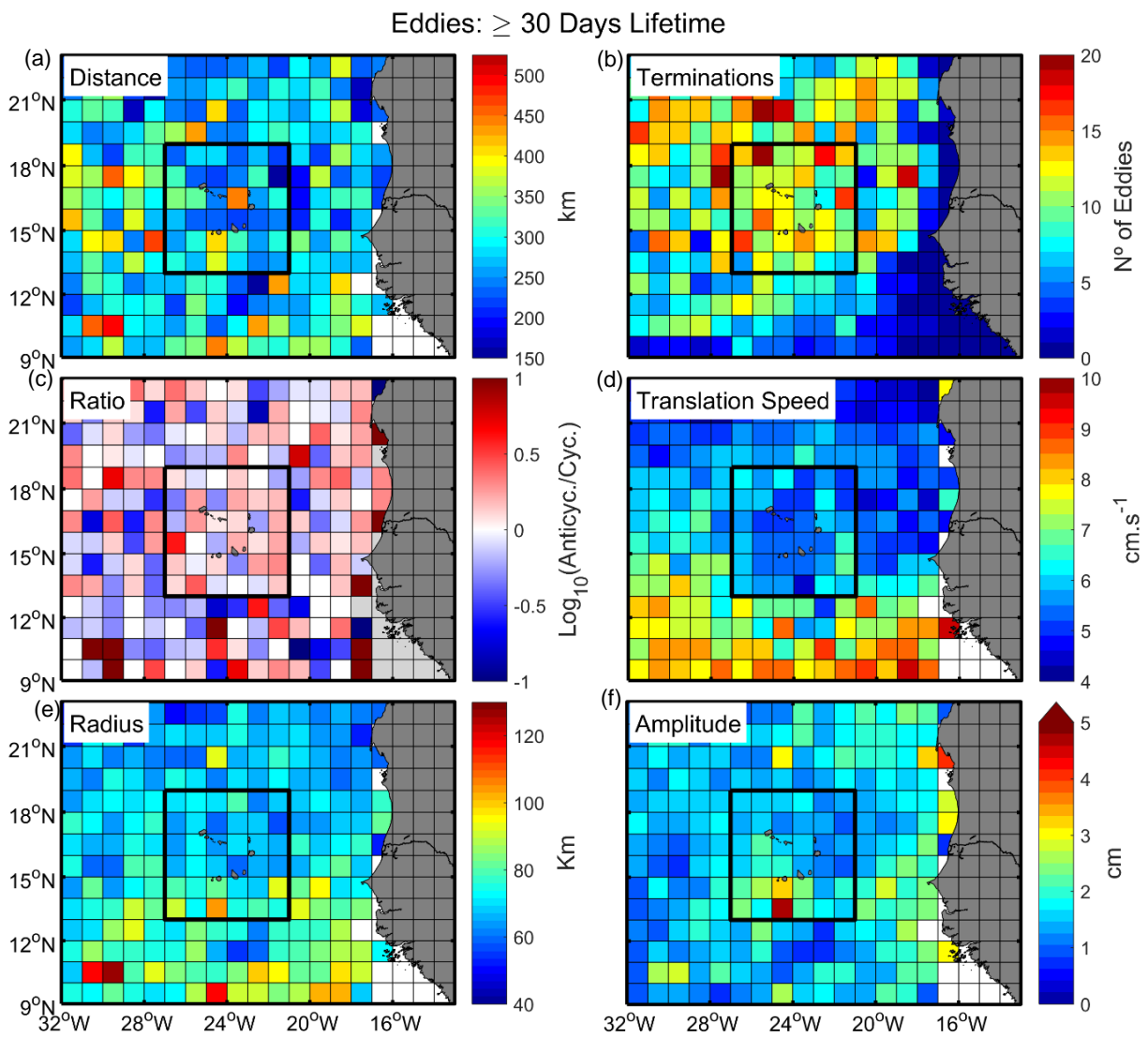
Figure 4.6 – Geographical distribution of the mean eddy kinematic properties, considering medium and long-lived (≥ 30 days) eddies generated in every 1° × 1° box.

Table 4.2 – Descriptive statistics of the eddy kinematic properties: CV and Outside Eddies

		CV Eddies		Outside Eddies	
		Cyclonic	Anticyclonic	Cyclonic	Anticyclonic
Number of Eddies		1118	1164	6289	6251
Lifetime (days)	Max	243	210	365	340
	Min	2	2	2	2
	Mean	19.36	19.88	15.21	15.16
Travel Distance (km)	Max	1599.33	1091.59	1717.51	1394.15
	Min	0.34	0.1	0.04	0.23
	Mean	93.85	96.11	80.44	77.96
Translation Speed (cm.s^{-1})	Max	14.23	14.83	29.82	31.16
	Min	0.2	0.05	0.02	0.13
	Mean	5.46	5.55	6.35	6.34
Radius (km)	Max	190.24	174.95	221.56	255.64
	Min	30.52	30.5	30.09	30.09
	Mean	53.84	52.95	56.31	55.6
Amplitude (cm)	Max	9.71	6.97	24.23	31.29
	Min	0.03	0.03	0.02	0.02
	Mean	0.89	0.81	1.17	1.13

For the travelled distance (Figure 4.6a), there is no obvious pattern at first sight. This can be explained by the fact that some boxes have a very low number of eddies with lifetime ≥ 30 days (Figure 4.4), which leads the average travel distance to be disproportional in some cases, being ultimately misleading. The latter is reinforced in Annex E.1, where eddies with lifetime ≥ 7 days are considered. Considering that the travel distance is directly proportional to the eddy lifetime – with a considerable 0.9 linear correlation (Figure 4.7) –, one may assume that the mean geographical and statistical distribution for the eddy travel distance and lifetime are very closely related. A similar statistical representation as the one generated for the eddy lifetime (Figure 4.3) was conducted for the travelled distance, but due to the striking similarity it is provided in Annex G.1. Most eddies of both areas (CV and outside) have a short travel distance, as approximately 60% of the total population do not exceed the 50-km distance (Annex G.1). Some eddies can travel for long distances (>1000 km), though the mean value is about 94 and 79 km for CV and outside eddies, respectively.
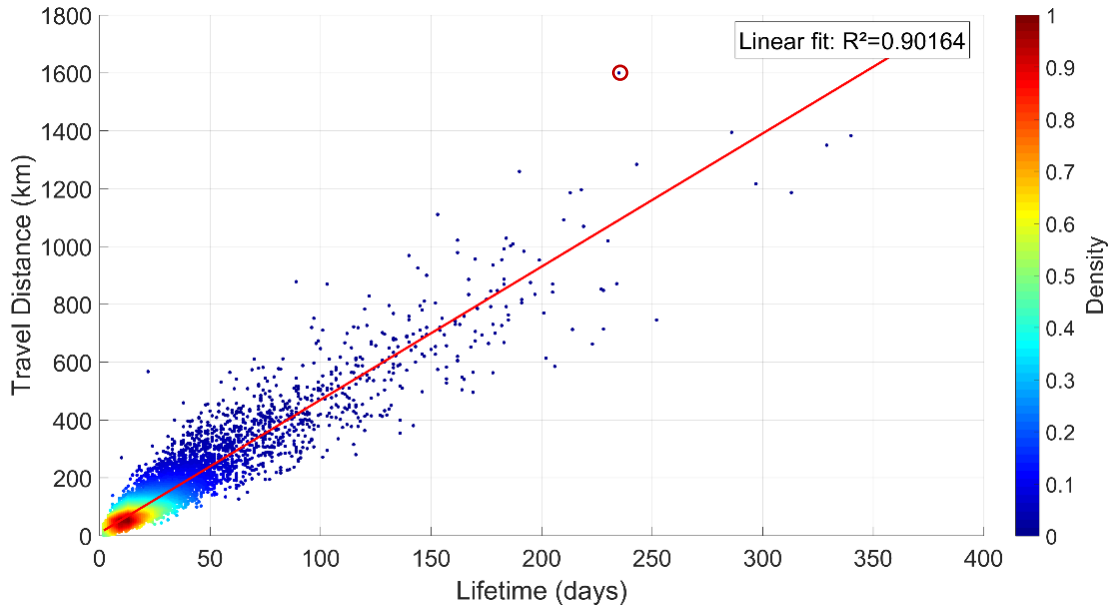
Figure 4.7 – Scatter plot and linear correlation between eddy lifetime and travel distance. Colour scale represents data density. Red circle represents the longest eddy trajectory (C1), identified in Figure 4.23.

The number of eddy terminations is represented in Figure 4.6b. In this subplot, each box accounts only the number of eddies that terminate there. The pattern seems to be randomly distributed, since the boxes with higher number are dispersed around the study area. The objective here was to verify if the far-field eddies intersection with the archipelago could leave a noticeable signature, but this is not the case.

Regarding the eddy polarity distribution, the ratio between anticyclonic and cyclonic eddies is represented in Figure 4.6c. The latter was $\log_{10}$ transformed for the purpose of normalization. As such, positive (red) and negative (blue) values indicate the dominance of anticyclonic and cyclonic eddies, respectively, while empty boxes indicate an equilibrium between the two polarities. In general, this figure is in perfect agreement with Table 4.1, as a vast number of white boxes is observed and the number of red and blue boxes seem to be counterbalanced. Nevertheless, some areas appear to have a predominant polarity. Anticyclonic eddies are prevalent in the coastal zone and on most boxes inside the CV area, particularly the ones that have a higher than average number of eddy origins – in the lee of Santo Antão and Fogo islands (Figure 4.4). However, cyclonic eddies are scattered around the study area and do not show a distinctive pattern. Several boxes have a very strong signal (1 or -1), indicating that only cyclonic or anticyclonic eddies were generated there. This result is biased by the small number of eddies originated in the respective areas and should be neglected.

The average translation speed per box is represented in Figure 4.6d. A distinctive spatial pattern is present, as higher speed eddies (≥ 7 cm.s^{-1}) seem to originate south and west of the CV area. In fact, CV area appears to act as an impediment to eddy propagation, since the boxes between the archipelago and the coastal area, as well as the ones within the delimited area, have predominant low translation speeds. From the statistical graphical representation (Figure 4.8), this pattern is also perceivable. CV eddies travel at a mean speed of approximately 5.54 cm.s^{-1} (4.78 km.d^{-1}), while outside eddies travel at a mean speed of approximately 6.35 cm.s^{-1} (5.49 km.d^{-1}) (Table 4.2). The difference in maximum values is even more impressive, since outside eddies can reach a mean maximum translation speed of approximately 30 cm.s^{-1} (25.92 km.d^{-1}), while CV eddies do not exceed ~14 cm.s^{-1} (12.1 km.d^{-1}) (Table 4.2). The latter is further reinforced by the boxplots in Figure 4.8, where the number of outliers is significantly higher for outside eddies. This parameter is the only one that follows a gaussian curve – meaning that the population is symmetrically distributed, with a higher concentration of values approximately at the centre of the distribution.
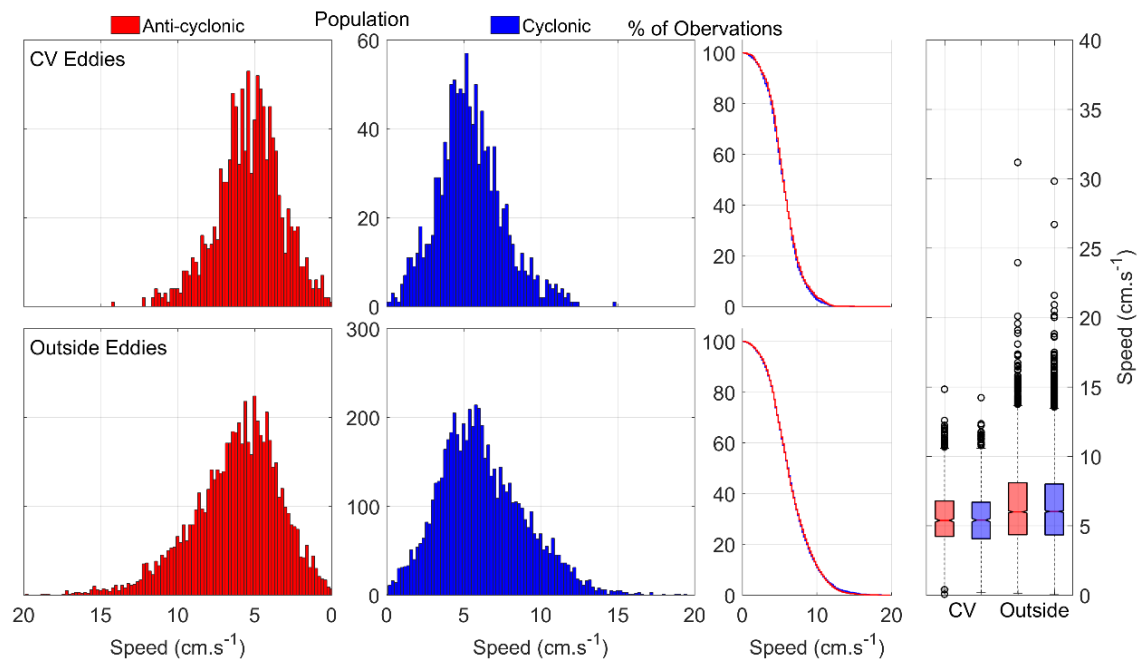
Figure 4.8 – Translation speed statistical distribution. From left to right: Histograms, representing the number of eddies (two left panels); upper-tail cumulative histograms, representing the percentage of observations (third panel); and boxplots (forth panel).

The average radius geographical distribution is represented in Figure 4.6e, along with the respective statistical representation in Figure 4.9. Considering that the eddies radius is calculated as a function of the area (Equation 7), it is reasonable to expect that the area associated with such features follows the same distribution of the eddies radius (Annex G.2) – as the correlation between

these two parameters is quite significant (0.93, Annex G.3). Furthermore, the scale of an eddy is highly dependent on the altimetry spatial resolution, leading the detectable eddies to have a minimum radius of approximately 30 km (Table 4.2). The most evident pattern in this subplot is very similar to the one described in the previous subplot, in the sense that higher values are located in lower latitudes. An interesting signal can be found in the lee of Fogo Island, an area that was identified in the previous Figure 4.4 as a hotspot for medium and long-lived eddies. Here, the mean radius reaches an approximate 105 km length, which is quite significant since the average for the CV and outside eddies is about 53 and 56 km, respectively (Table 4.2). Like the eddy distance (Figure 4.6a) and polarity ratio (Figure 4.6c), some boxes with very high values are identified in the map, but are biased from the small number of eddies being accounted for the mean and should be neglected. From the boxplots it is possible to observe that eddies generated outside CV have a slightly higher radius than the CV eddies. However, the latter can be explained by the fact the mean eddy radii tend to increase with lower latitudes, which in turn are mostly located outside CV area. The upper tail cumulative histograms confirm that the two groups of eddies follow each other's distribution very closely, as an exponential distribution is easily observed. From the analysis of the geographical and the descriptive statistical distribution, one may conclude that the Cape Verde Archipelago does not have a major influence on the eddy radius, being the variation in latitude the principal factor.
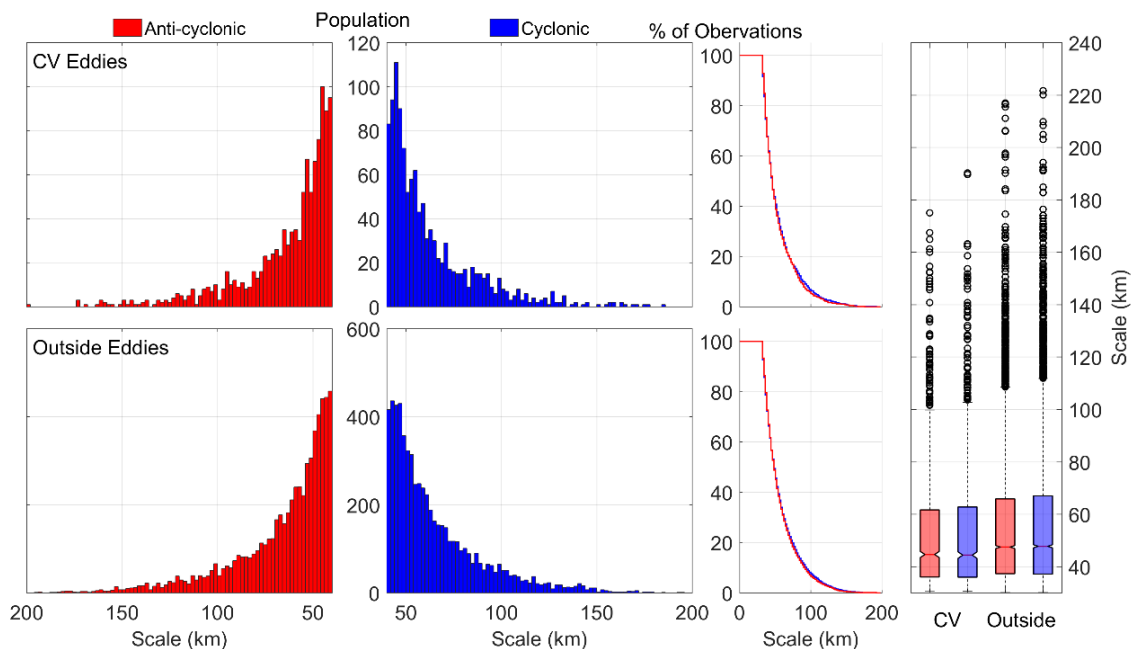
Figure 4.9 - Radius statistical distribution. From left to right: Histograms, representing the number of eddies (two left panels); upper-tail cumulative histograms, representing the percentage of observations (third panel); and boxplots (forth panel).

Lastly, the eddies amplitude is further characterized. This parameter represents the difference in SSH from the higher (lower) extreme to the lower (higher) SSH contour of the cyclonic (anticyclonic) eddy. The geographical distribution in Figure 4.6f indicates that, in general, eddies generated in the coastal area have a higher amplitude (from 2 to 3 cm) in comparison with the rest of the study area. The mean values for CV and outside eddies are around 0.86 and 1.15 cm (Table 4.2), respectively. Nevertheless, the most remarkable signal arises once again from the medium and long-lived eddy hotspot – in the lee of Fogo Island – exceeding a significant 5 cm amplitude. From the normal and the upper-tail cumulative histograms in Figure 4.10, an exponential distribution is evident, as most of the population is skewed to the low values area. For the CV area, cyclonic eddies appear to have a slightly higher amplitude than anticyclonic eddies, as the blue line (cyclonic) in the upper-tail cumulative histograms detaches from the red line (anticyclonic) at around 4 cm amplitude. The latter is also confirmed by the mean values, which are 0.89 and 0.81 cm for cyclonic and anticyclonic eddies, respectively (Table 4.2).
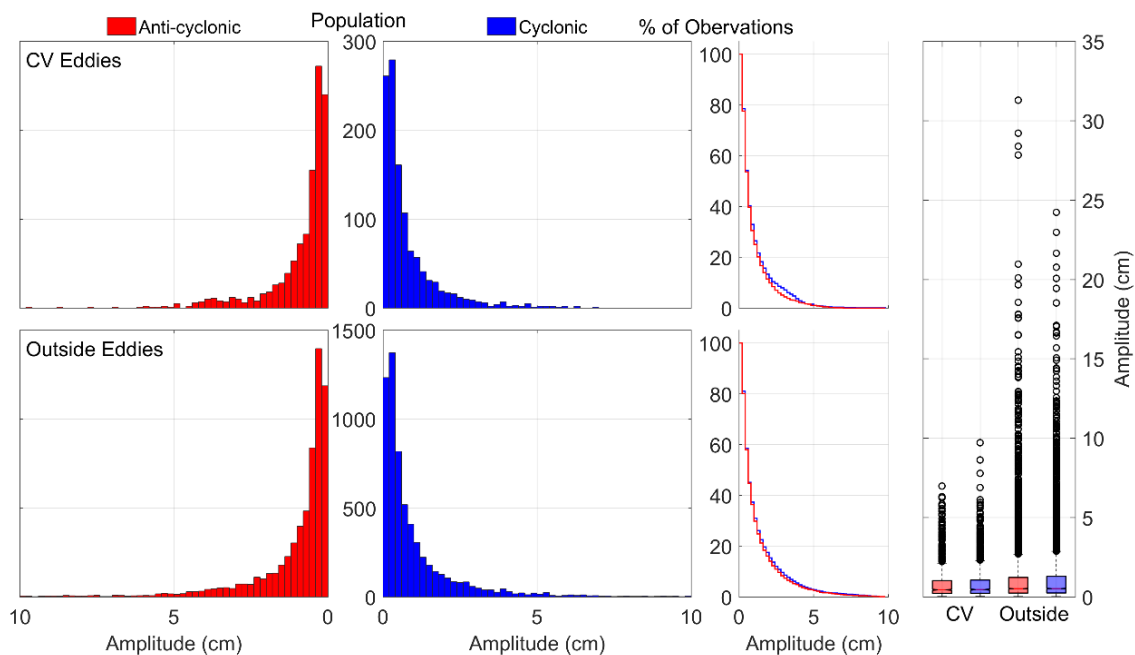

Figure 4.10 – Amplitude statistical distribution. From left to right: Histograms, representing the number of eddies (two left panels); upper-tail cumulative histograms, representing the percentage of observations (third panel); and boxplots (forth panel).

4.3. Far-field Eddies

After a first statistical analysis, a more detailed characterisation is presented. The far-field eddies are defined as eddies that are originated outside CV area but pass by or terminate inside the delimited area. The main objective here is to characterise and assess the impact of these eddies on the archipelago (and vice-versa), as well as its nature and behaviour. Only long-lived eddies (≥ 60 days lifetime) are accounted from this point onwards, representing approximately 23 % and 34 % of the total cyclonic and anticyclonic far-field eddies, respectively (Annex H.1). From this selection, eddies that are not relevant for the current analysis – those that are created near the CV area and trespass the delimitation, even if they do not pose a significant impact on the archipelago – are successfully eliminated, without jeopardising the eddies of interest (Annex C:).

Far-field eddies trajectories and points of origin are presented in Figure 4.11. All eddies travel westward, with some meridional deflections along the way. Anticyclonic eddies seem to be the dominant polarity, as most trajectories and points of origin are represented in red. At latitudes comprising the archipelago (15 – 17ºN), it seems obvious that the incoming eddies cannot advance further than the islands. Thus, a shadow effect is created with the archipelago acting as a barrier. This effect is even more noticeable at higher latitudes, where the eddy trajectories do not intersect the islands and are thus able to continue their path, reaching longitudes as far as 30ºW.
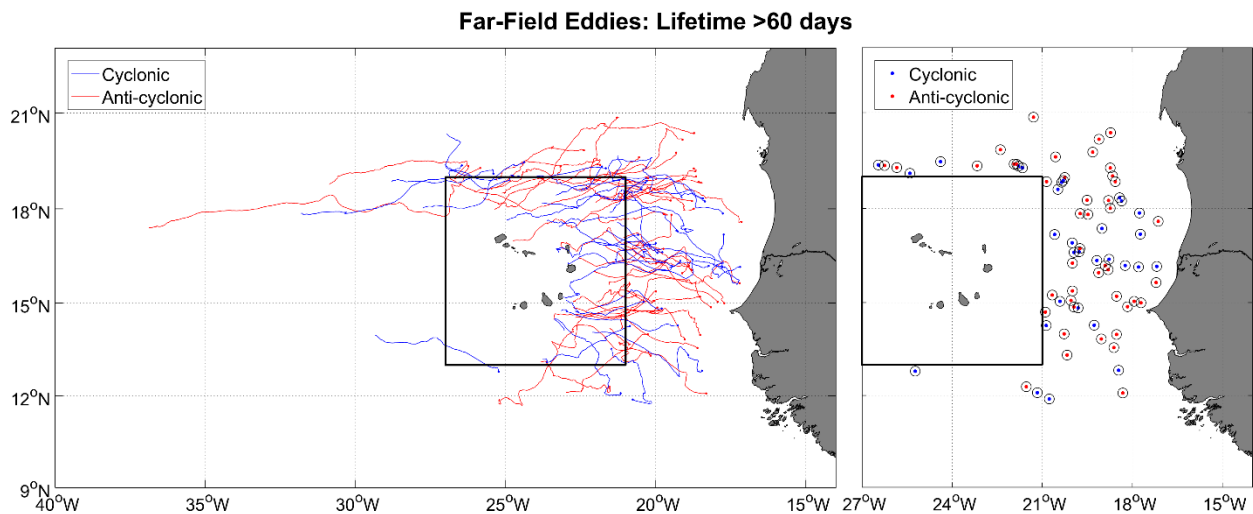
Figure 4.11 – Far-field long-lived (≥ 60 days) eddy trajectories (left panel) and points of origin (right panel). Blue and red colours represent cyclonic and anticyclonic eddies, respectively.

The easternmost islands of the archipelago are undoubtedly the most impacted by incoming eddies – specially Sal, Boa Vista, Maio and Santiago – because most far-field eddies are generated between those latitudes and, as they travel west, they end up interacting with the islands. The windward group (Santo Antão, São Vicente, Santa Luzia and São Nicolau; Figure 2.1) receives eddies mostly with a south-westward direction, although there are some exceptions from the east. The leeward group, however, only receives eddies that originate east of CV, with some exceptions coming from southeast. In fact, Fogo is the only Island that is not reached by any long-lived far-field eddy, as it seems to be sheltered by the Santiago and Maio islands. Regarding the eddy origins, anticyclonic eddies are predominant near Cape Vert and Cape Blanc, with the appearance of some cyclonic eddies near the Mauritanian coast. Many of the far-field eddies are created north of the archipelago, whereas very few of them are created in the south.

As far-field eddies need to travel longer distances to be considered as such, their kinematic properties (Annex H.1) are generally higher than the ones created inside and outside CV area (Table 4.2). Thus, it is reasonable to assume that the incoming eddies are, in general, more robust than most of the others.

All eddies show evidences of meridional deflections. These variations are presented in Figure 4.12, as a function of longitudinal propagation. In the left panels, long-lived eddy trajectories are plotted from a common point of origin by subtracting the initial position (coordinates) from the trajectory. The right panels show the histograms of the meridional variation between the final and the initial position of each eddy. The histograms are skewed poleward for the cyclones and equatorward for anticyclones, with a mean azimuth of 0.29º poleward and 0.28º equatorward, respectively. The difference in the dominant meridional sign is quite significant, as 60 % of the cyclonic eddies have a predominant poleward deflection, while the anticyclonic have an almost identical result (57 %) in the opposite direction. Some of these patterns can be identified in Figure 4.11, as red trajectories seem to have a predominant south-westward direction – mainly those created at higher latitudes (> 17ºN), and blue trajectories seem to propagate mostly in the north-westward direction – especially those created at lower latitudes (< 15ºN). Furthermore, anticyclonic eddies appear to travel longer distances than the cyclones. However, Annex H.1 shows that long-lived cyclonic eddies (≥ 60 days) travel, on average, ~11 km more than anticyclonic eddies, though the latter have higher maximum distances – which in turn is associated with those eddies that are generated at higher latitudes, intersect CV area but fail to interact with the islands (Figure 4.11).
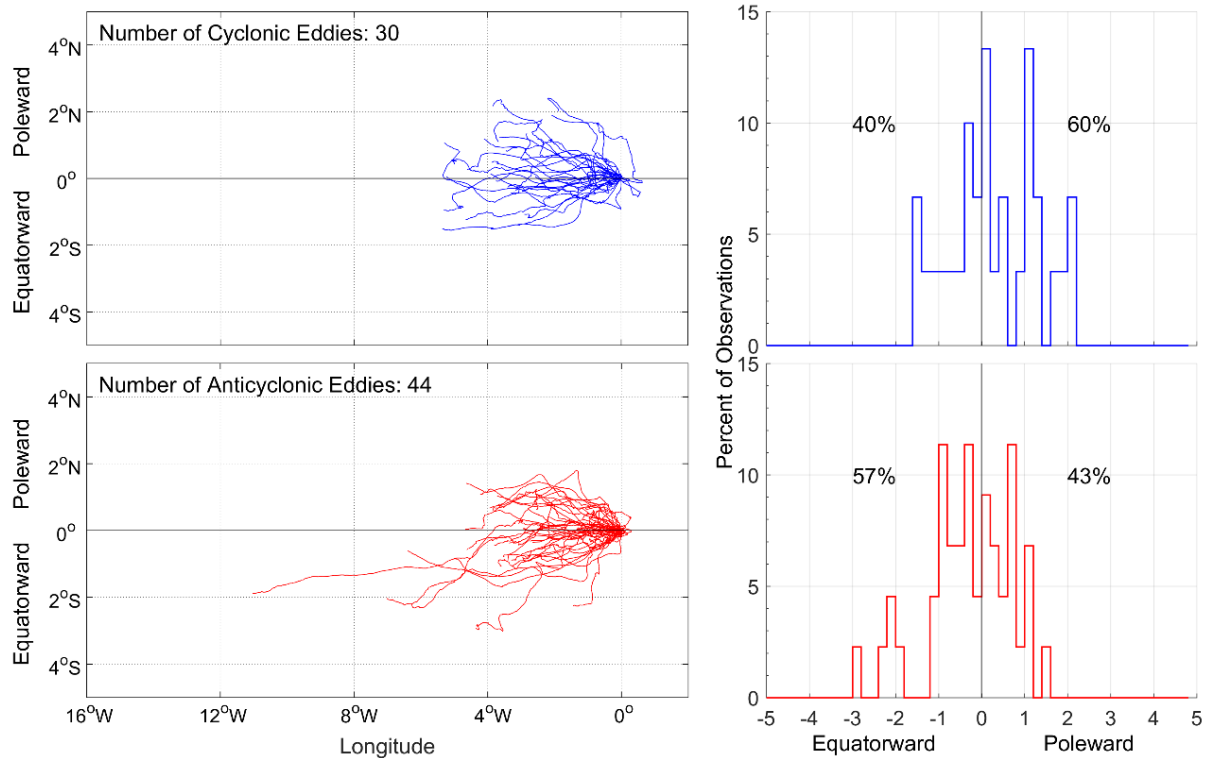
Figure 4.12 - Meridional deflections of the cyclonic (upper panels) and anticyclonic (lower panels) long-lived (≥ 60 days) far-field eddies. The left panels show the changes in longitude and latitude relative to the initial location of each eddy. The right panels show histograms of the average azimuth of each eddy trajectory.

Time-latitude plots (Hovmöller diagrams) were computed using a meridional cross-section set in the eastern CV boundary (21ºW) and between the latitudes from 12 – 19ºN. Although some eddies approach the archipelago from north and south, most of them come from east (Figure 4.11), thus the positioning of the cross section. The main objective here is to identify far-field eddy signatures and to assess its frequency in space and time. As such, two variables are represented in Figure 4.13, with the SLA (computed from the ADT and the 12-year MDT) in the upper panel, and the EKE in the middle panel. The usage of these two different (but intrinsically connected) datasets is based on the fact that both variables complement each other, in the sense that eddy-induced signals are easily detectable in the EKE panel, but the SLA panel holds information regarding their polarity. The latitudinal average for both variables is represented in the lower panel, where the anomaly (red for positive, blue for negative) and the light-blue linear plot represent the SLA and EKE datasets, respectively. It should be noted that, as all eddies travel westward, the x-axis (which represents time) orientation was shifted from left to right to facilitate the interpretation. Moreover, a SLA linear trend (~3.77 mm.yr^{-1}) was found in the meridional cross-section (Annex I.1), and considering that the latter could bias positive and negative signals, the dataset was detrended.

50

The final months of all the years are characterised by positive SLA, whereas the first months are marked by negative values (Figure 4.13). Some punctual and localised positive (anticyclonic) and negative (cyclonic) SLA signals are identified, though the positive seem to be more frequent than the negative – which is in agreement with Figure 4.11. The EKE panel is marked by identical signals, which validates the relationship between both datasets. Cyclonic eddies seem to occur mostly during late spring and summer. Nevertheless, anticyclonic eddies are also found during that period, as it is the case of the year 2008 – when 4 anticyclones are evident in the SLA panel. Most of the strongest EKE signatures ($\sim$1000 cm^2.s^{-2}) are found between 12 –16ºN and are normally seen from late Autumn to spring. For example: in December 2003 (14 – 16ºN) and November 2005 (12 – 14ºN) it is possible to identify one cyclonic (C0) and another anticyclonic eddy (A0), respectively (circled in black). Those signals extend 2º in latitude, indicating that the diameters of such features were ~222 km length. Nevertheless, there are some remarkable events occurring all year round, as it is the case of the years between 2008 and 2012. This period was, unequivocally, the one with the highest number of far-field eddies entering the CV area. It was also the one in which the eddy signatures were more distributed in space and time.
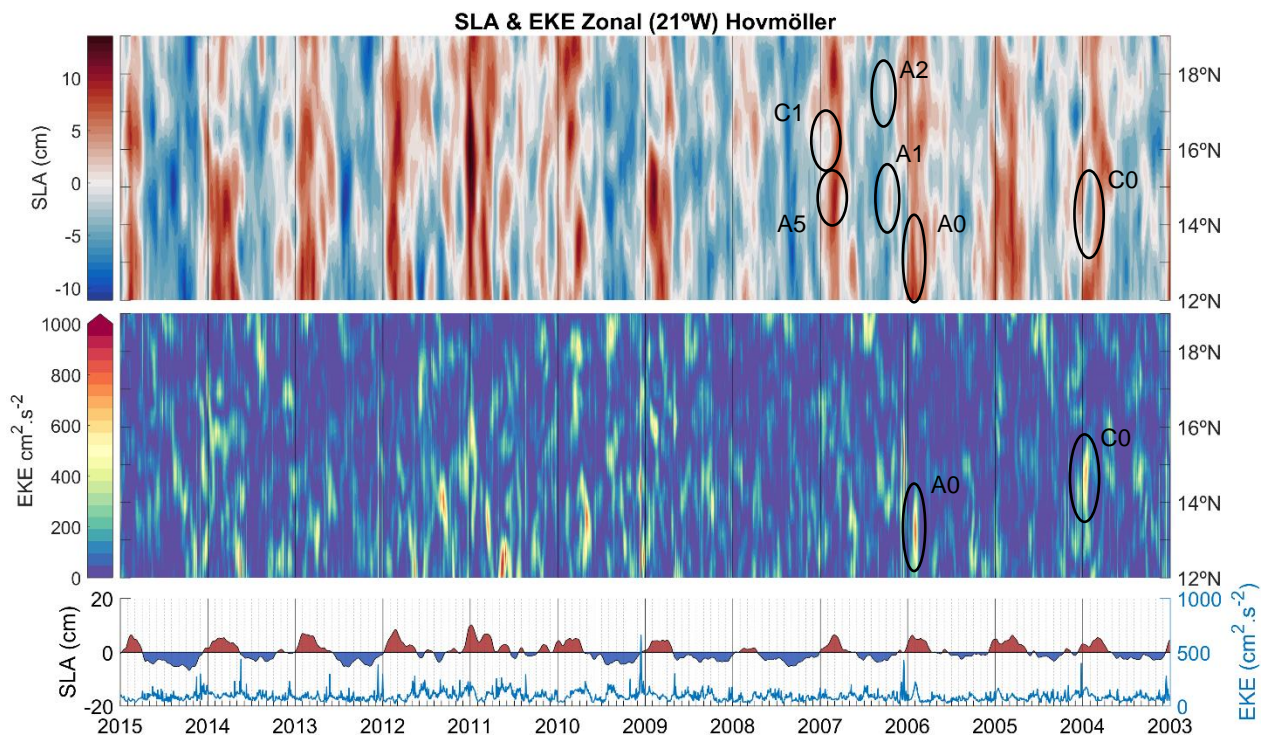
Figure 4.13 – Zonal Hovmöller diagrams for SLA (upper panel) and EKE (middle panel) along 21ºW and the latitudes from 12 – 19ºN (eastern CV boundary in Figure 4.11). Identified signals represent specific far-field eddy cases. In the lower panel, the latitude-averaged SLA and EKE are represented by the anomaly plot (left axis) and the blue line (right axis), respectively.

As a seemingly seasonal signal was identified for both variables, the seasonality of the SLA and EKE far-field zonal signatures were computed, where each day from January to December represents the average of the all respective days between the 12-year study period (Figure 4.14). In the SLA panel a seasonal pattern is evident. Minimum SLA values (~ -4.5 cm) are reached in May, while maximum values (~6.2 cm) are observed between October and December. The strong seasonal signal hampers the identification of eddy signals. In the EKE panel, however, a seasonal pattern seems to exist in the months of January and August, though with low maximum values (~300 $cm^2.s^{-2}$). Nevertheless, all the other months show evidences of relatively high EKE values (150 – 200 $cm^2.s^{-2}$), which leads to the conclusion that there are no obvious seasonal eddy signatures in this cross-section.
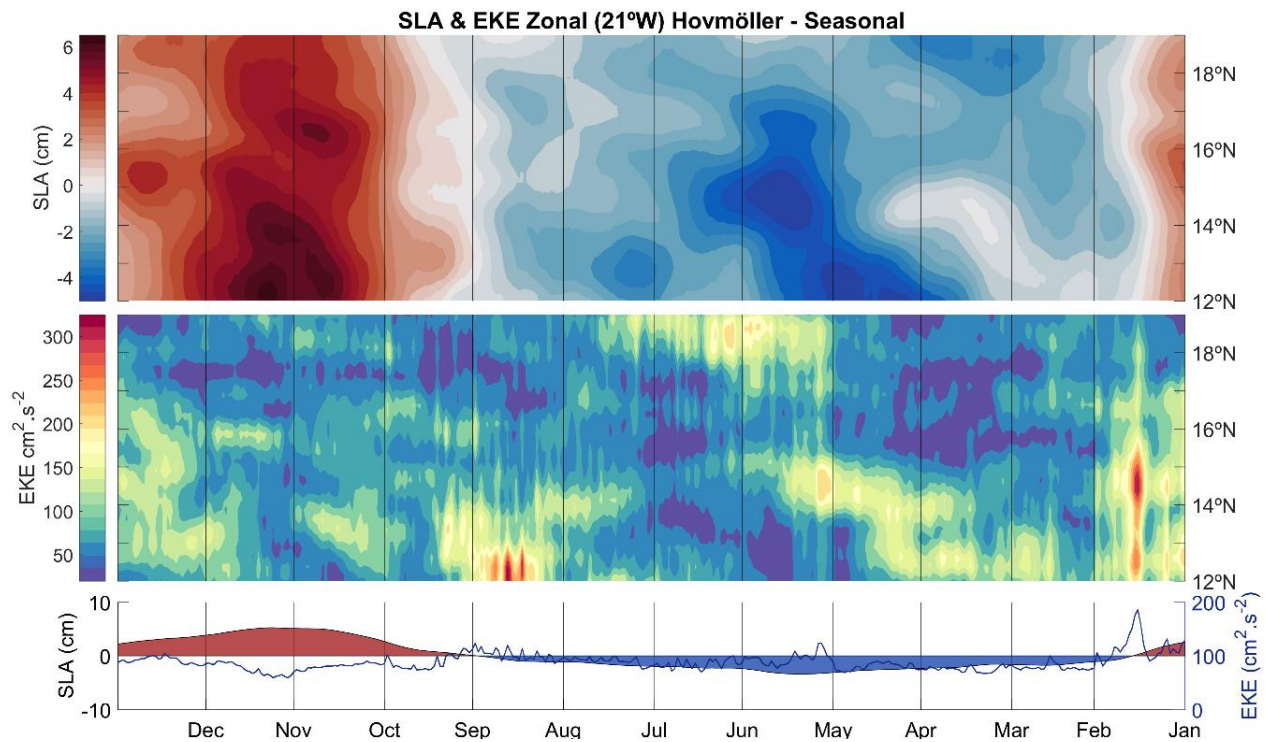
Figure 4.14 - Seasonal zonal Hovmöller diagrams for SLA (upper panel) and EKE (middle panel) along 21ºW and the latitudes from 12 – 19ºN (eastern CV boundary in Figure 4.11). In the lower panel, the latitude-averaged SLA and EKE are represented by the anomaly plot (left axis) and the blue line (right axis), respectively.

4.3.1. Specific cases

Far-field eddies are subjected to many processes in their transition to offshore, especially when interacting with the archipelago of Cape Verde. The main objective in this analysis is to assess the outcomes of such interaction. As such, the period of 19th March 2006 – 2nd May 2007 was selected for the characterisation of 9 eddy trajectories. The latter is divided in two parts, represented in Figure 4.15 and Figure 4.16. Many eddies are present in the selected timesteps, but only the ones most representative of the processes in focus are identified and characterised. A sequential characterisation follows, in which each paragraph is dedicated to each timestep.

First in 19th of March 2006 (Figure 4.15a), three anticyclonic eddies arise at distinct locations: A1 is created west of Cape Vert, very close to the CV delimitation; A2 is created west of Mauritania coast; and A3 is created southwest of Cape Blanc.

After almost 4 months (2nd July 2006, Figure 4.15b), A1 and A3 show a significant southward meridional deflection in their westward translation. Consequently, A1 avoids a direct interaction with the leeward group of islands, while the intersection of A3 with the windward group becomes more likely to happen. A2 continues at approximately the same latitude, with some minor meridional deflections along the way.

Fifteen days later (17th July 2006, Figure 4.15c), A1 gets farther from the archipelago and continues propagating south-westward, while A3 propagates steadily in a westward orientation. A2, on the other hand, intersects the westernmost islands of the windward group (Santo-Antão, São Vicente, Santa Luzia and São Nicolau, Figure 2.1). At the same time that this eddy is under transformation and the outer perimeter extends in longitude, another eddy of the same polarity (A4) originates south-west of Santo-Antão. This eddy, however, seems to be part of the same SLA body as the A3. Still in the same date, a dipole SLA signal appears north of Cape Vert, giving origin to a cyclonic (C1) and anticyclonic (A5) eddy.

Ten days later (27th July 2006, Figure 4.15d), A1 gets even farther away from the archipelago, while A3 keeps its westward propagation without any significant change. A2 however, is considered terminated by the eddy tracking algorithm, although some of its SLA signal remains visible. On the opposite side of the windward islands, A4 increases in amplitude and initiates a westward propagation to offshore, though it outer delimitation is still attached to the remaining A2 SLA body. At the coast, the newly generated C1 and A5 eddies seem to be entangled, as the anticyclonic and cyclonic eddies moved north-westward and south-eastward, respectively.

Another 10 days latter (6th August 2006, Figure 4.15e), A1 loses its southward component and propagates exclusively to west, while A3 increases in area and continues its westward translation. A4 gets more robust while propagating westward – increasing in area and amplitude –, and the outer periphery becomes more compact. At the coast, C1 and A5 appear to continue entangled, though the former increases significantly in amplitude, while the latter almost disappears.

Almost 2 months later (5th October 2006, Figure 4.15f), A1 is considered terminated after a short sequential southward and northward deflection, but some of its SLA signal remains visible. A3 deflects significantly to the south, entering in a collision line with the windward islands and extending its outer periphery. The A4 suffers a slightly southward deflection while propagating westward. An interesting behaviour is seen at the coast, when C1 and A5 detach from each other. At this moment, C1 inverts its direction from east to west, while the A5 ceases its northward direction and propagates almost exclusively westward.

Ten days later (15th October 2006, Figure 4.15g), A3 is given as terminated after its southernmost area intersects Santo Antão Island, though its SLA body keeps propagating south-westward (doted contour). A4 keeps its translation without any notable change, while C1 and A5 suffer a minor southward deflection at approximately the same instant.

Finalising the Part I of the selected period (4th November 2006, Figure 4.15f), the new A6 arises from the terminated A3 SLA body, west of Santo-Antão. The A4 continues propagating west as previously observed. The A5 propagates south-westward, getting further away from the islands, while the C1 moves westward in the direction of the easternmost group of islands (Sal, Boa Vista and Maio, Figure 2.1).

In the continuation of the previous sequences, Part II is represented in Figure 4.16. In 19th of November 2006 (Figure 4.16a), A4 and A6 continue their translation westward, along with C1, without any significant change. A5, however, is considered terminated as most of the SLA signal seems to dissipate.

Almost 1 month later (14th December 2006, Figure 4.16b), A4 and A6 are given as terminated, as their SLA signal seems to have dissipated completely. Concurrently, C1 increases its amplitude (from -1 to -4 cm), becoming more robust and closer to the eastern islands, with the outer perimeter intersecting Boa Vista Island.

Approximately one month and a half later (2nd February 2007, Figure 4.16c), C1 intersects in its entirety the eastern group of islands. Consequently, the eddy seems to be deflected southeast, while the eastern branch gets elongated and extends zonally until it reaches Fogo Island.

Only five days later (7th February 2007, Figure 4.16d), a new eddy arises (C2) in the northern side of Fogo, in what it seems to be part of the previously described elongated branch of C1. At the same time, C1 loses some of its amplitude and remains approximately at the same location, continuing interacting with Boa Vista and Maio Islands.

Twelve days later (19th February 2007, Figure 4.16e), a second eddy (C3) is created southwest of Fogo, in what seems to be another elongated branch of C1 and C2. C2 increases in area and remains at approximately at same location, while C1 gets weaker and moves slightly to the west in the direction of Maio Island.

In the 4th of March 2007 (Figure 4.16f), C1 is considered terminated, as all of its SLA signal is lost when intersecting Maio. C2 and C3 detach from the common SLA body, significantly increasing their amplitude by >10 and 8 cm, respectively. Both eddies appear to have a similar propagation direction with a strong north-westward component.

Ten days later (14th March 2007, Figure 4.16g), C2 is terminated as most of its SLA body seems to merge with C3. Consequently, the latter increases in amplitude and in size.

In the last sequence (2nd May 2007, Figure 4.16h), C3 is considered terminated after propagating north-westward, but most of its signal persists in the SLA field, though significantly more elongated than before. In fact, after a cautious analysis of the supplementary material, it was observed that this eddy continues propagating westward until it vanishes completely from the SLA field at around 40ºW, between 9th and 16th of November 2007 (6 months later).
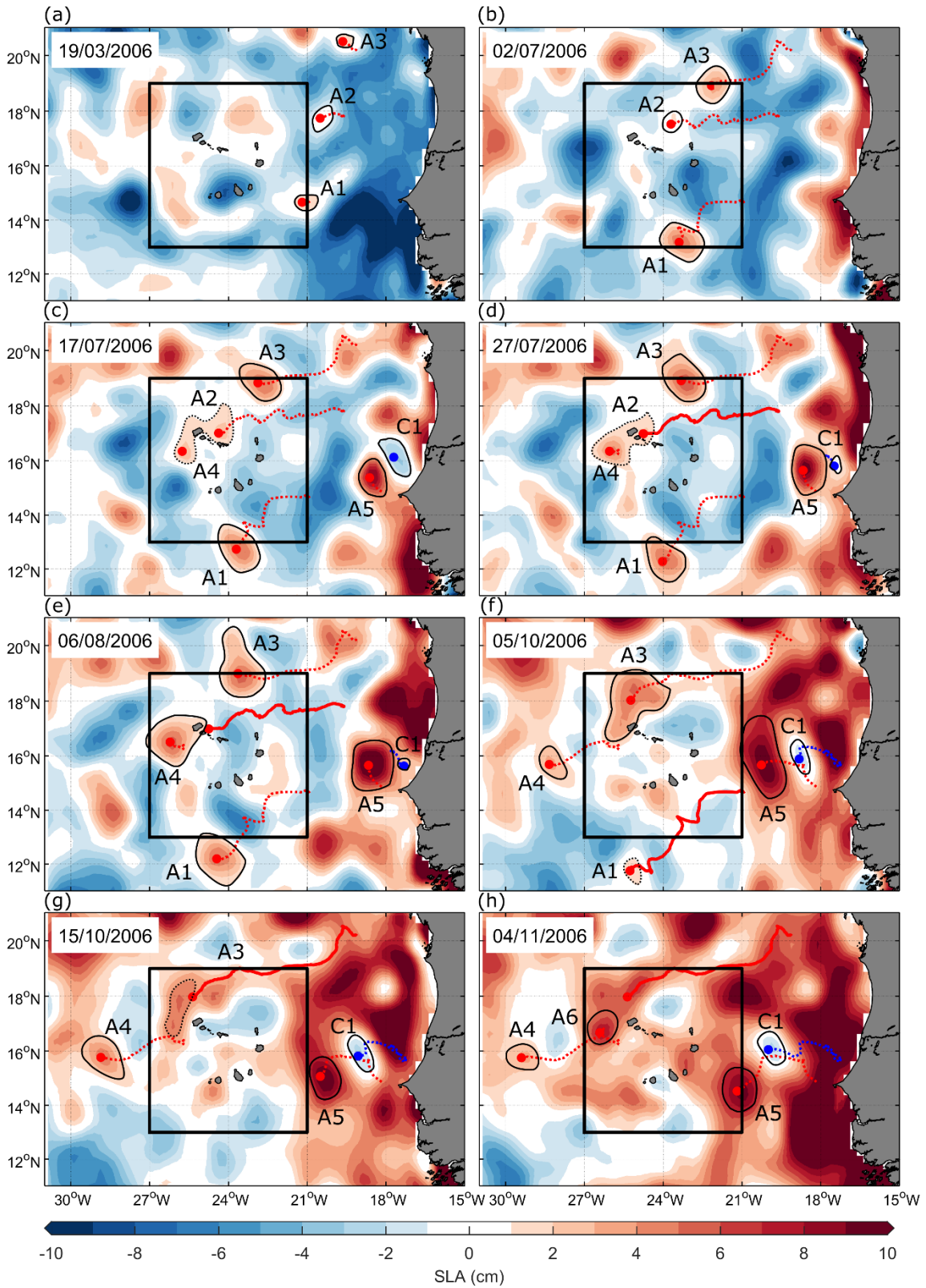
Figure 4.15 – Far-field eddies evolution from 19th March 2006 to 4th November 2006, plotted against SLA maps (Part I). Black square represents CV area. Blue and red colours represent cyclonic and anticyclonic eddies, respectively. Doted and solid lines represent active and terminated eddy tracks, respectively; black solid and doted contours represent the active and the transformed eddy delimitation (-2 to 2 cm amplitude), respectively.
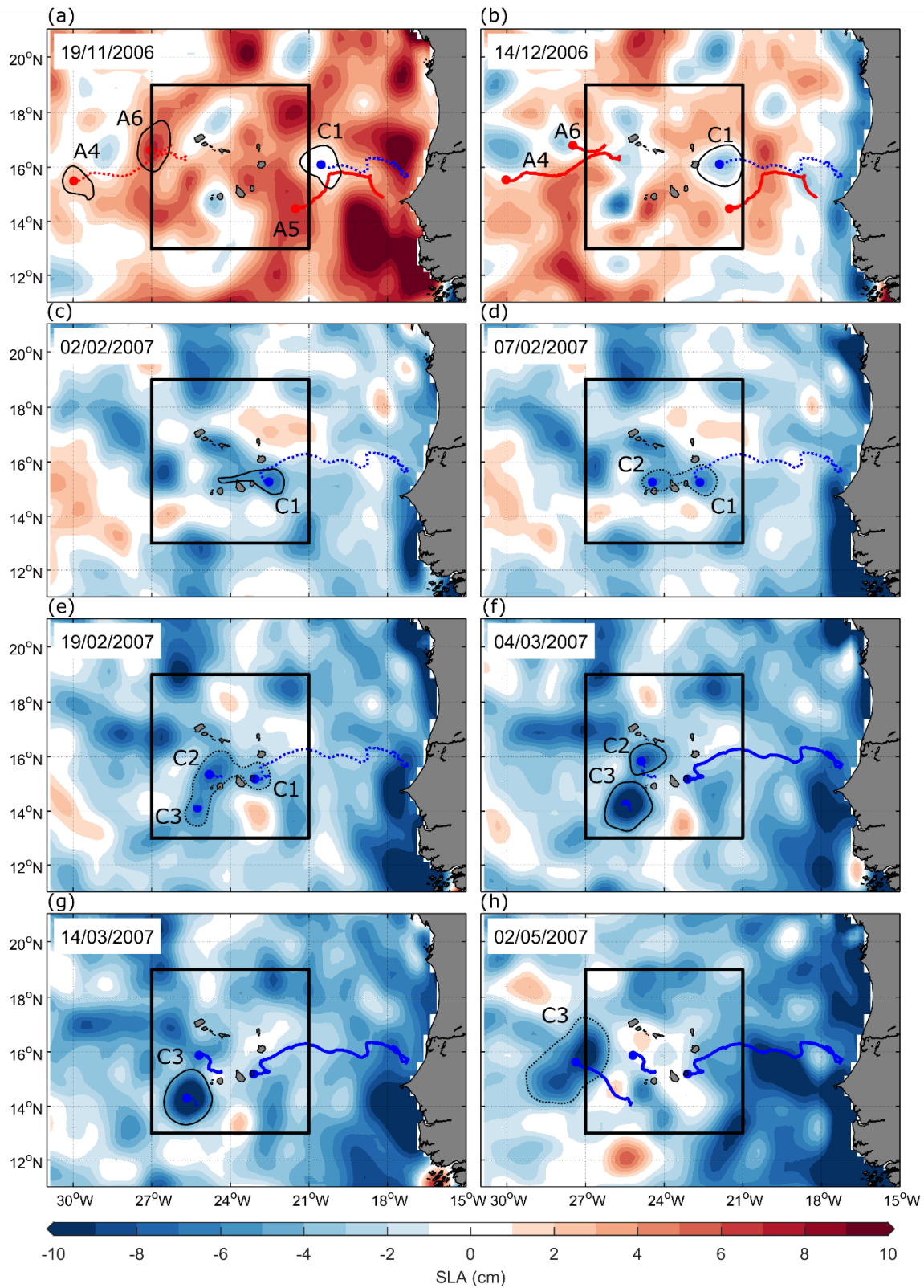
Figure 4.16 – Far-field eddies evolution from 19th November 2006 to 2nd May 2007, plotted against SLA maps (Part II). Black square represents CV area. Blue and red colours represent cyclonic and anticyclonic eddies, respectively. Doted and solid lines represent active and terminated eddy tracks, respectively; black solid and doted contours represent the active and the transformed eddy delimitation (-2 to 2 cm amplitude), respectively.

4.4. Near-field Eddies

Following the same kind of analysis as the one conducted for the long-lived far-field eddies (previous sub-chapter), the long-lived near-field eddies are further characterised. These are defined as eddies that are created inside the CV area. What differs from the previous analysis is merely the nature and the mechanisms behind the generation of such features, which are most likely to be driven by the islands interaction with the atmosphere and/or the ocean. Nevertheless, it is also very likely that some of these eddies result from the interaction of the far-field eddies with the archipelago. Only 71 (~6 %) and 80 (~7 %) of the total near-field cyclonic and anticyclonic eddies, respectively, were selected for this analysis (Table 4.1). In this case, the application of a 60-day filter was extremely important, since the number of eddies with lower lifetime is significantly higher than for the far-field eddies, hampering the analysis and interpretation of spatial patterns (Annex D:).

That being said, long-lived near-field eddy trajectories (bigger panel) and points of origin (smaller panel) are represented in Figure 4.17. The most noticeable pattern is, as for the far-field eddies (Figure 4.11), the dominant westward orientation with some meridional deflections. A considerable number of eddies are observed to originate in the lee of the archipelago's highest islands (Santo Antão and Fogo) – which in turn is in accordance with Figure 4.4. The majority of these eddies have an anticyclonic polarity. Some eddies are originated east and north of the islands, but in fewer numbers. Due to their location, the latter are most likely to be caused by processes other than island-induced perturbations, thus they are not so relevant for the current analysis. The length of the trajectories is considerably high, with a mean value of approximately 480 and 454 km for cyclonic and anticyclonic eddies (Annex J.1), respectively, which is expected due to the minimum lifetime threshold applied. One of the most interesting patterns is related to the propagation of the eddies that originate in the lee of Fogo Island. Here, almost all the red tracks have a very similar behaviour, with a clear south-westward orientation and identical extensions. Near this area, an agglomerate of long-lived cyclonic eddy origins appears to dominate the area between Fogo and Santiago islands. Despite the proximity to the former group of eddies, the latter have a predominant westward propagation. Still, the travelled distances seem identical, except for one large track (C1) that almost reaches 40ºW. This specific eddy has a very interesting behaviour, when at approximately 30ºW starts deflecting south-westward at a constant rate. Given the peculiarity of such eddy, some attention was regarded towards the characterisation of the latter in

the next section (Figure 4.23), being also identified in the previous Figure 4.7 and in the following Figure 4.18 as the longest eddy track on record, and in the following Figure 4.19 as the most distinctive eddy signal in the EKE field. In the windward group of islands, cyclonic tracks (blue) are more evident because of their extension, being able to reach longitudes far west of 35ºW. In fact, the maximum travelled distances for cyclonic and anticyclonic eddies is approximately 1600 and 1091 km, respectively, though the mean values are only 15 km apart (Annex J.1).
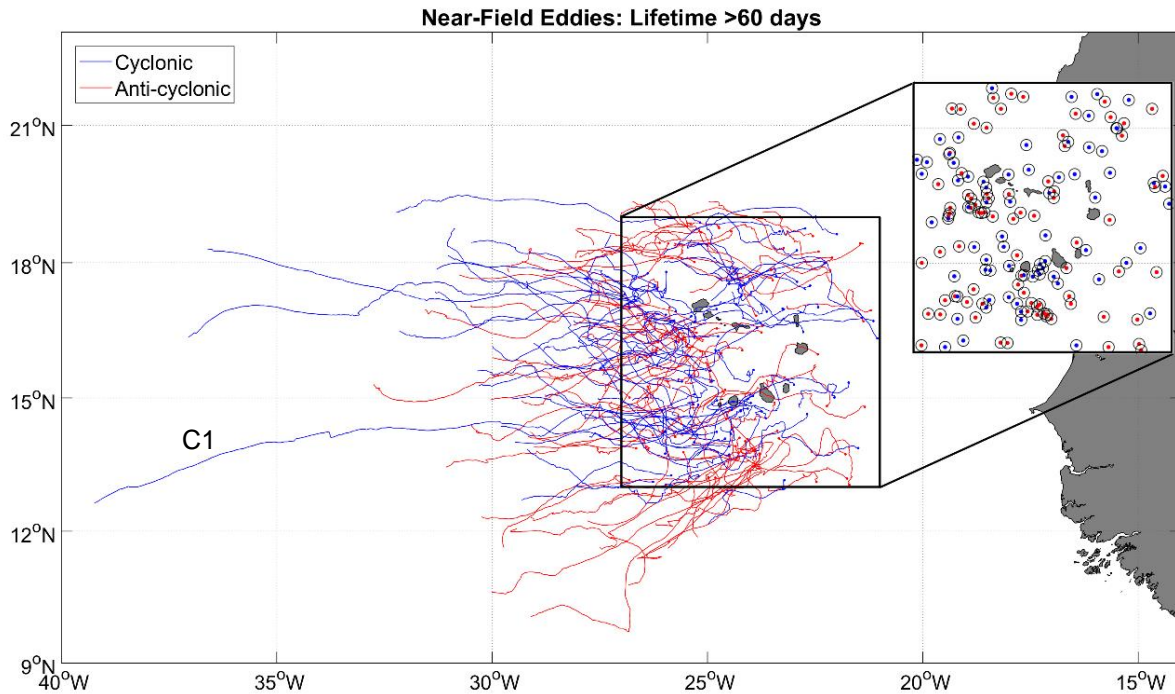
Figure 4.17 - Near-field long-lived (≥ 60 days) eddy trajectories (main panel) and points of origin (smaller panel). Blue and red colours represent cyclonic and anticyclonic eddies, respectively.

The difference in maximum travelled distance is well noticeable in Figure 4.18, where the meridional deflection for every track is presented. It is well clear that 6 specific cyclonic tracks have exceptional extensions (around 1100 – 1600 km). However, if these tracks were excluded, the average travel distance for cyclonic eddies would be quite lower, as the remaining eddies have a relatively short extension. Even more remarkable, however, is the difference in the main meridional track orientation. While cyclonic eddies do not show a significant trend for equatorward or poleward propagation, it is obvious that this is not the case for anticyclonic eddies. In fact, 63 % and 38 % of the anticyclones have a dominant equatorward and a poleward propagation, respectively. Moreover, the mean azimuth for such eddies is approximately 0.48ºS. On the other hand, cyclonic eddies are more evenly distributed, with 49 % and 51 % of the long-lived population

propagating equatorward and poleward, respectively. As expected, the mean azimuth for cyclonic eddies is considerably lower than for anticyclonic eddies (0.14ºN).
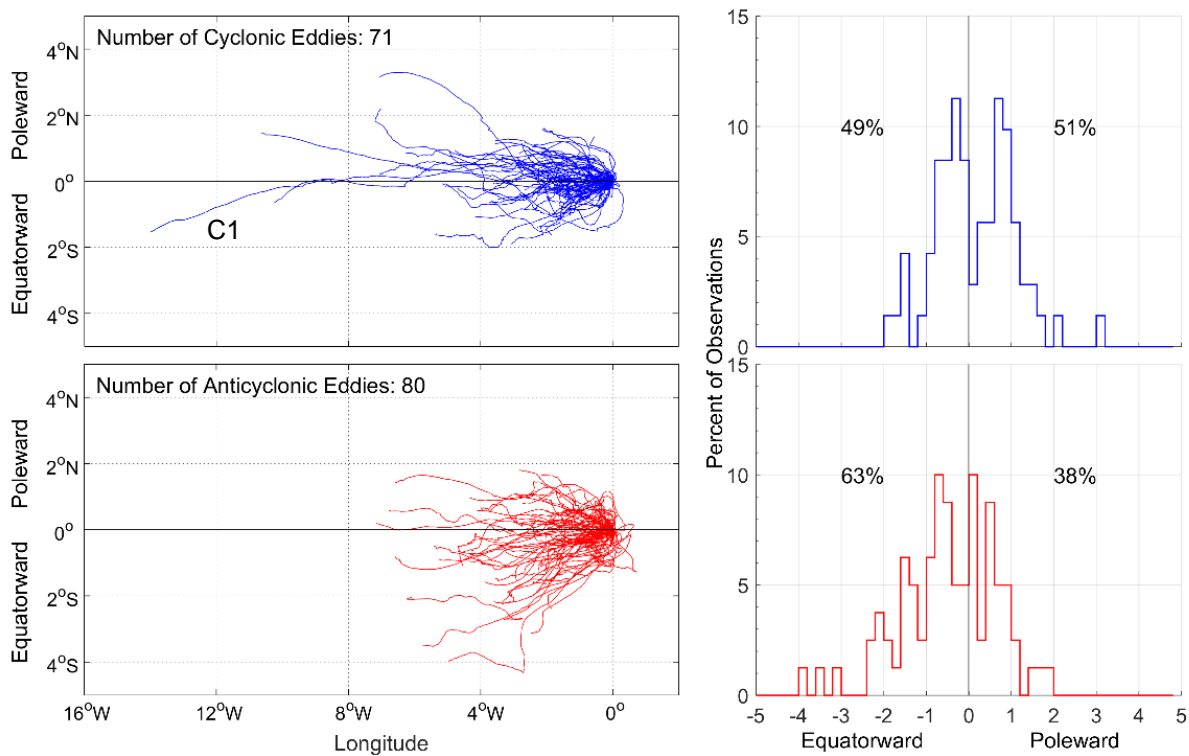
Figure 4.18 - Meridional deflections of the cyclonic (upper panels) and anticyclonic (lower panels) long-lived (≥ 60 days) near-field eddies. The left panels show the changes in longitude and latitude relative to the initial location of each eddy. The right panels show histograms of the average azimuth of each eddy trajectory.

Hovmöller diagrams were computed for the near-field eddies. Considering that many eddies propagate through the southern CV boundary, one additional meridional cross section was performed (Figure 4.17). Very few eddies are exported offshore through the northern CV boundary, and those that are, are most likely to be generated by mechanisms other than the ones in focus. Thus, these eddies are neglected from the current analysis.

The zonal Hovmöller is set in the western CV boundary (26ºW) and covers the latitudes between 12 – 19ºN (Figure 4.19). The x-axis is oriented from right to left to simulate the westward eddy propagation. Furthermore, the SLA was detrended as trend of approximately 3.60 mm.yr^{-1} was found (Annex K.1). The SLA seasonal pattern is not so evident in this diagram, although the dominance of positive values is recurrent in the last months of several years. The SLA panel shows evidences of an exceptional period between 2010 and 2012, when a predominant positive SLA signal is clear. This period is even more evident in the anomaly plot represented in the lower panel.

Several cyclonic (negative) and anticyclonic (positive) signals are dispersed throughout space and time, though cyclonic eddies are more often observed in the first half of the year.

In the EKE panel, a remarkable number of high value signals is observed, following the same behaviour as the SLA. The latter is also evident in the lower panel, where the latitudinal averaged EKE is represented in blue and is marked by a highly dynamic pattern. The most evident pattern, however, is easily identified between 14 – 16ºN. This persistent band of high EKE values (≥ 1000 $cm^2.s^{-2}$) is present in all the years, though with variable intensity. In conjunction with the upper panel, it is possible to link these signals to cyclonic eddies, while the anticyclonic eddies seem to be associated with lower EKE values. Judging from the EKE signal extensions, the eddy diameters can vary between 1º and 4º degrees in length (~111 and ~444 km, respectively). The perfect example of an eddy footprint is observed in late 2004 – beginning 2005 between 14 – 16ºN. This signal belongs to the previously identified C1 and is, undoubtedly, the clearest on the EKE record so far. As it propagates westward at low speeds, the eddy centroid distinguishes from the eddy perimeter as a point of low EKE values, circled by very high values (≥ 1000 $cm^2.s^{-2}$).
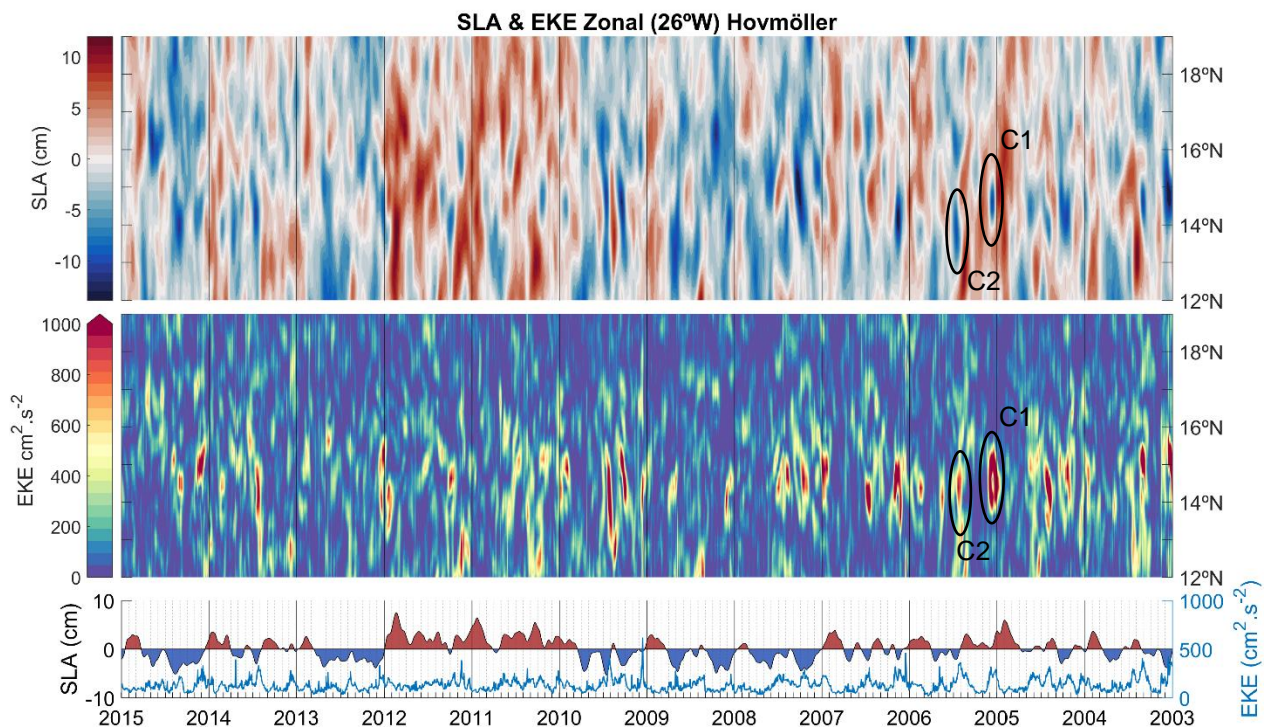
Figure 4.19 - Zonal Hovmöller diagrams for SLA (upper panel) and EKE (middle panel) along 26ºW and the latitudes from 12 – 19ºN (western CV boundary in Figure 4.17). Identified signals represent specific near-field eddy cases. In the lower panel, the latitude-averaged SLA and EKE are represented by the anomaly plot (left axis) and the blue line (right axis), respectively.

In order to assess the seasonal behaviour of the SLA and EKE datasets, the 12-year daily average was computed and is presented in Figure 4.20. From the analysis of the upper panel, a seasonal pattern seems to exist, as positive values mark the final 3 months of the year. Cyclonic signals are recurrent in April, June and September, whereas anticyclonic signals are more difficult to determine. However, only the cyclonic signal identified in June has a corresponding counterpart in the EKE panel (though with a negative time-lag), with values exceeding 500 cm^2.s^{-2}. Besides this, some other EKE signals are observed, but do not show an obvious corresponding pattern in the SLA panel.
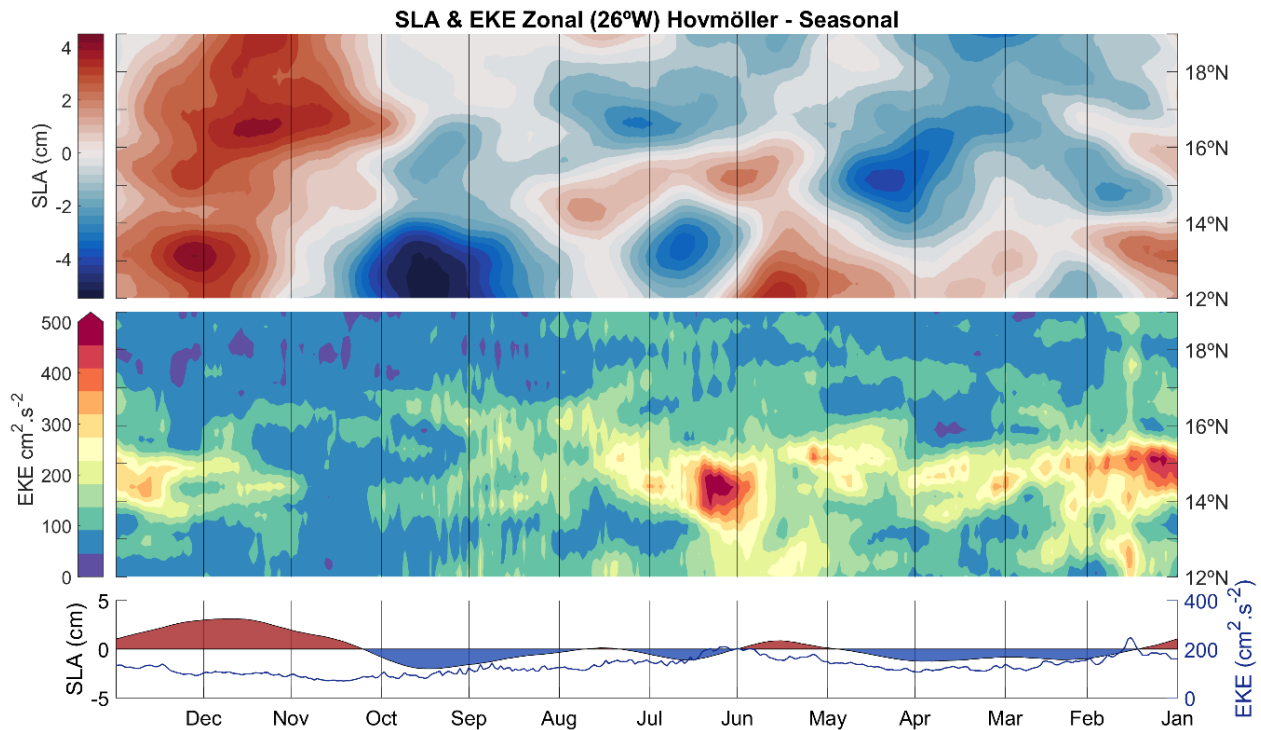
Figure 4.20 – Seasonal zonal Hovmöller diagrams for SLA (upper panel) and EKE (middle panel along 26ºW and the latitudes from 12 – 19ºN (western CV boundary in Figure 4.17). In the lower panel, the latitude-averaged SLA and EKE are represented by the anomaly plot (left axis) and the blue line (right axis), respectively.

Longitude-time plots were computed along the southern CV boundary (13ºN) and for the longitudes between 21 – 27ºW. This specific Hovmöller diagram differs from the previous, in the sense that the x and y-axis are shifted. As the eddy propagation follows a south-westward orientation at this location (Figure 4.21), the time axis (y-axis) starts from the top, in order to simulate the passage of eddies through the cross-section and facilitate the interpretation. The SLA dataset was detrended, after a trend of approximately 5.05 mm.yr^{-1} was found (Annex L.1).

Following the same behaviour as the previous Hovmöller diagrams (Figure 4.13 and Figure 4.19), positive SLA characterise the final months of all year within the study period. However, the most evident pattern seen in both SLA and EKE panels is related to the orientation of the eddy signals. Most of the them start around 24ºW longitude and then propagate westward as time progresses, resulting in a tilted orientation. Furthermore, the SLA panel presents evidences of mostly positive signals, indicating the dominance of anticyclonic eddies. The latter two statements are in perfect conformity with the dominant eddy polarity and propagation in that area (Figure 4.21). Regarding the time frequency, there seems to exist a recurrent anticyclonic signal in the first months of all years, at almost exactly the same location (24ºW). Cyclonic signals are sometimes visible, but do not show any significant spatial or temporal pattern. In fact, the latter appear to be associated with the low EKE signals dispersed through the middle panel.
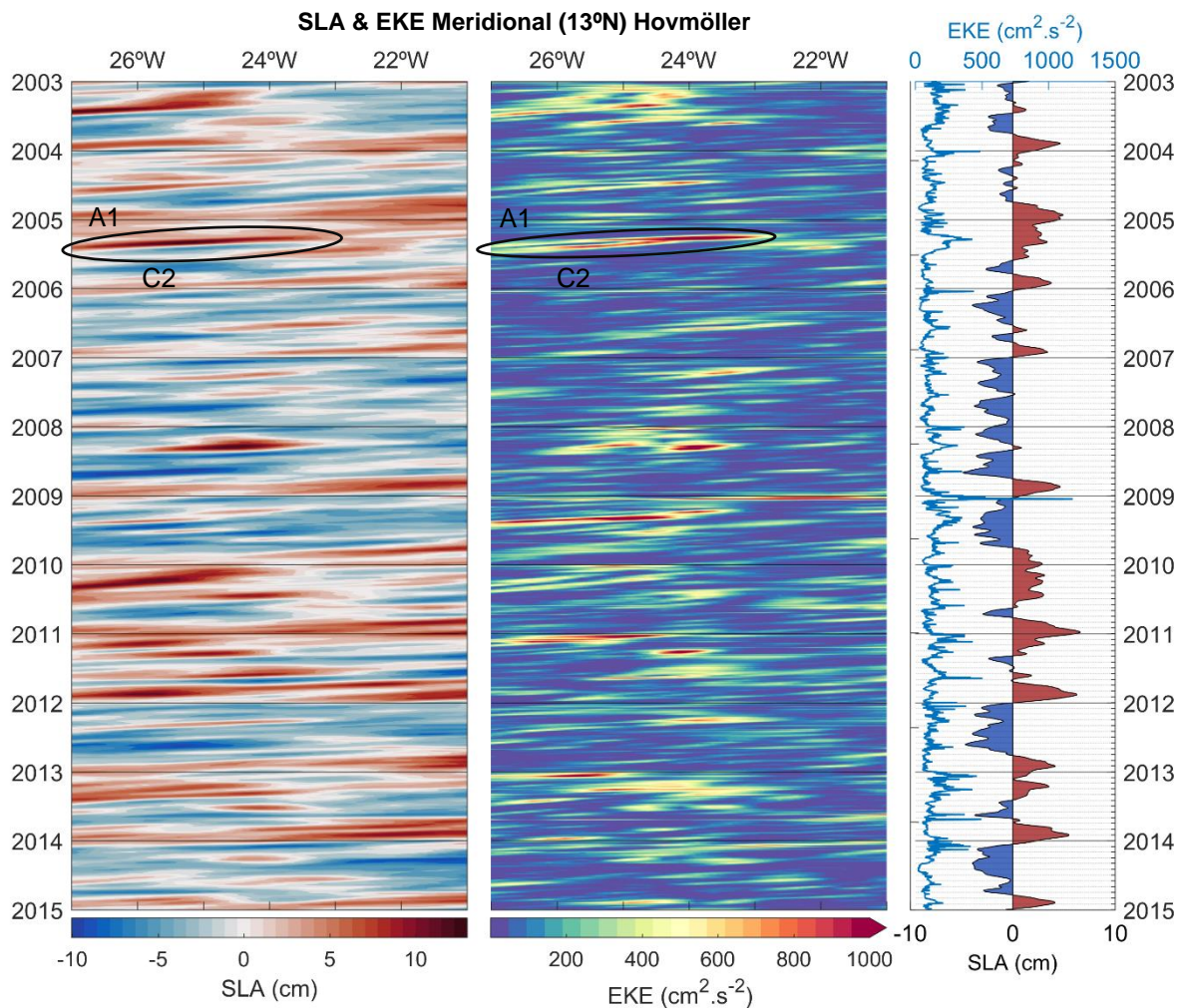
Figure 4.21 – Meridional Hovmöller diagrams for SLA (left panel) and EKE (middle panel) along 13ºN and the longitudes from 21 – 27ºW (southern CV boundary in Figure 4.17). Identified signals represent specific near-field eddy cases. In the right panel, the longitude-averaged SLA and EKE are represented by the anomaly plot (lower axis) and the blue line (upper axis), respectively.

The seasonal behaviour for SLA and EKE is represented in Figure 4.22 and was computed following the same procedures as the previous seasonal diagrams. This figure is, undoubtedly, the one which better represents a seasonal signal in both far-field and near-field eddies. The predominant positive and negative SLA values are again well noticeable in the last and initial half of the year, respectively. Moreover, the previously observed south-westward signal orientation is evident in both panels. Two distinct EKE signals are observed in January and March-April (~350 and ~500 $cm^2.s^{-2}$, respectively), very likely to be associated with the seasonal pattern observed in Figure 4.21. However, only the signal from March-April finds a correspondence in the SLA panel, which in turn is in conformity with the anticyclonic dominant polarity (Figure 4.21).
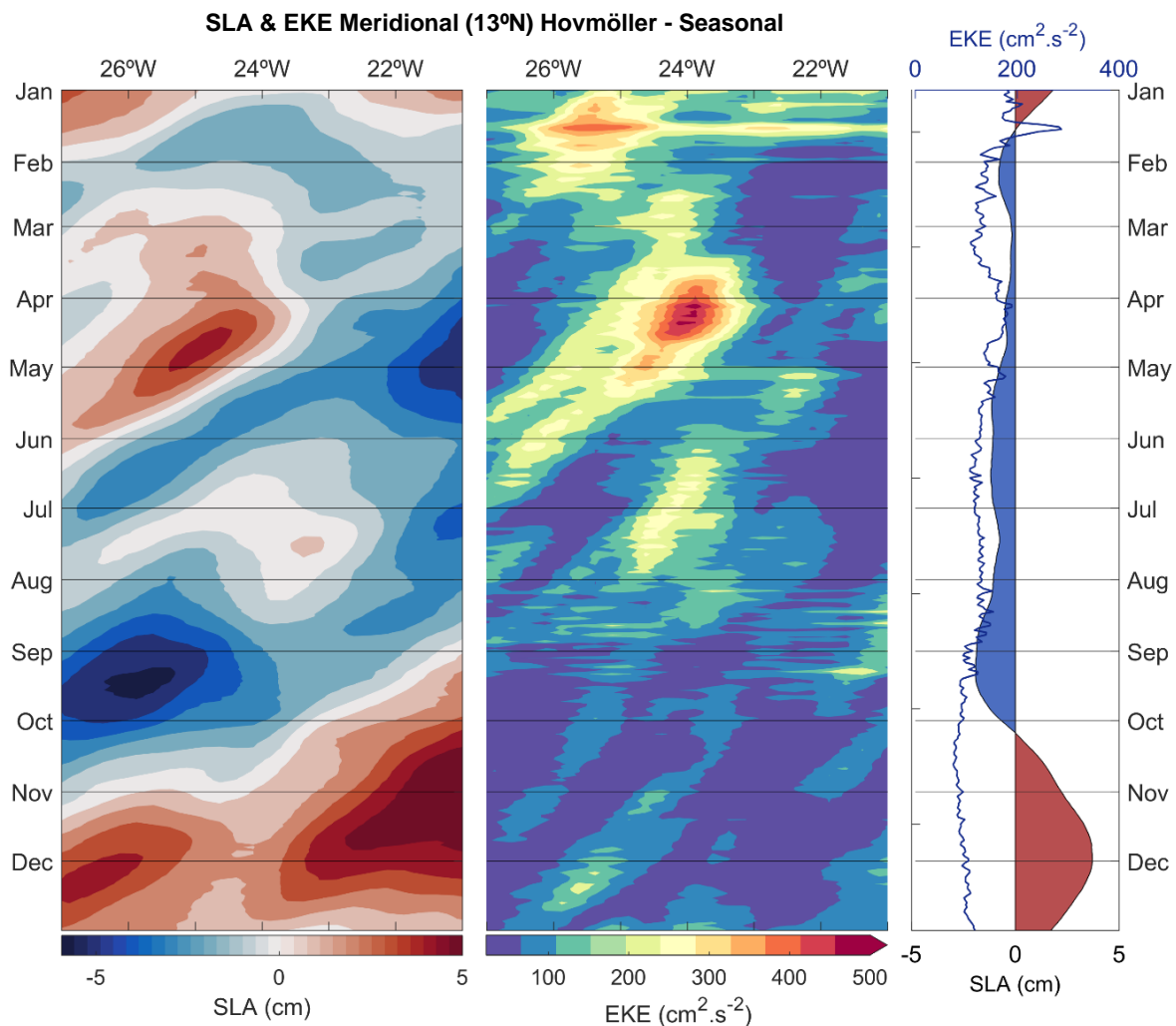
Figure 4.22 – Seasonal meridional Hovmöller diagrams for SLA (left panel) and EKE (middle panel) along 13ºN and the longitudes from 21 – 27ºW (southern CV boundary in Figure 4.17). In the right panel, the longitude-averaged SLA and EKE are represented by the anomaly plot (lower axis) and the blue line (upper axis), respectively.

4.4.1. Specific cases

Based on the results previously described, a great number of eddies are reported to originate in the lee of the major islands of Cape Verde. In order to investigate the nature and the evolution of such features, the period of 24th of December 2004 – 10th of August 2005 was selected, based on the number of eddies suitable for the purpose. Five seemingly island-induced eddies were identified and are represented in Figure 4.23. All eddies are most likely to be generated by the island interaction with the atmosphere and/or the oceanic background. The latter also means that, due to the complexity of the system, the possibility of a near-field eddy to result from the interaction of incoming far-field eddies with the archipelago, or even with near-field eddies, cannot be fully disregarded. As for the previous far-field eddy specific cases, many eddies are present in the selected timesteps, but only the ones most representative of the processes in focus are identified and characterised. As such, a detailed description of the latter follows.

On the 24th December 2004 (Figure 4.23a), an anticyclonic eddy (C1) forms in the lee of Fogo Island. Almost two months later (26th February 2005, Figure 4.23b), this eddy is seen propagating westward, after propagating first north-westward. Concurrently, one anticyclonic eddy (A1) originates almost at the same location of C1.

On 14th of March 2005 (Figure 4.23c) one anticyclonic eddy (A2) originates in the lee of Santo-Antão, while C1 continues translating west. A1 on the other hand, propagates eastward during the initial phase, becoming significantly larger – with a diameter of approximately 3º (333 km) – and increasing its amplitude (~10 cm).

Almost 1 month later (13th April 2006, Figure 4.23d), another cyclonic eddy arises (C2) west of Fogo Island, though with very small dimensions. C1 continues its translation following the same orientation as before. A1 changes its course and initiates a south-westward propagation, while A2 follows the same direction as A1.

One month later (13th May 2006, Figure 4.23e), another cyclonic eddy is created south of Santo Antão, with an initial southward direction. At this time, 4 eddies are simultaneously interacting with each other, while C1 gets farther away from the islands. A1 travelled a remarkable distance of approximately 240 km in the south-westward direction, while A2 keeps its previous orientation. C2 continues its southward direction, but with a small deflection to west.

On 7th of June 2006 (Figure 4.23f), the eddy trajectories remain almost identical to the previous timestep, with minor changes. A1 loses some of its amplitude to ~6 cm. An interesting change is observed in the C2 trajectory, as it acquires a westward dominant direction. C1 also seems to deflect slightly southward, while it translates westward.

Almost 1 month later (2nd July 2005, Figure 4.23g), A2 is given as terminated. Part of its signal seems to merge A1, which also appears to be in the process of dissipating, as its amplitude decreases and its diameter expands significantly. The C1 keeps its previous trajectory, but its southward component seems to increase. Even more interesting is the pattern observed in the C2 and C3 eddies, as their trajectories changes dramatically, with a north-westward direction.

Finally, all eddies are given as terminated after more than 1 month (10th August 2006, Figure 4.23h). C1, C2 and A1, however, seem to have a premature termination, as part of their SLA signal is still present in the figure (delimited by a black dotted line). Now that all eddies are terminated, the most interesting pattern is linked to the distinct characteristics between cyclonic and anticyclonic eddy trajectories. Only C1 follows a different behaviour.
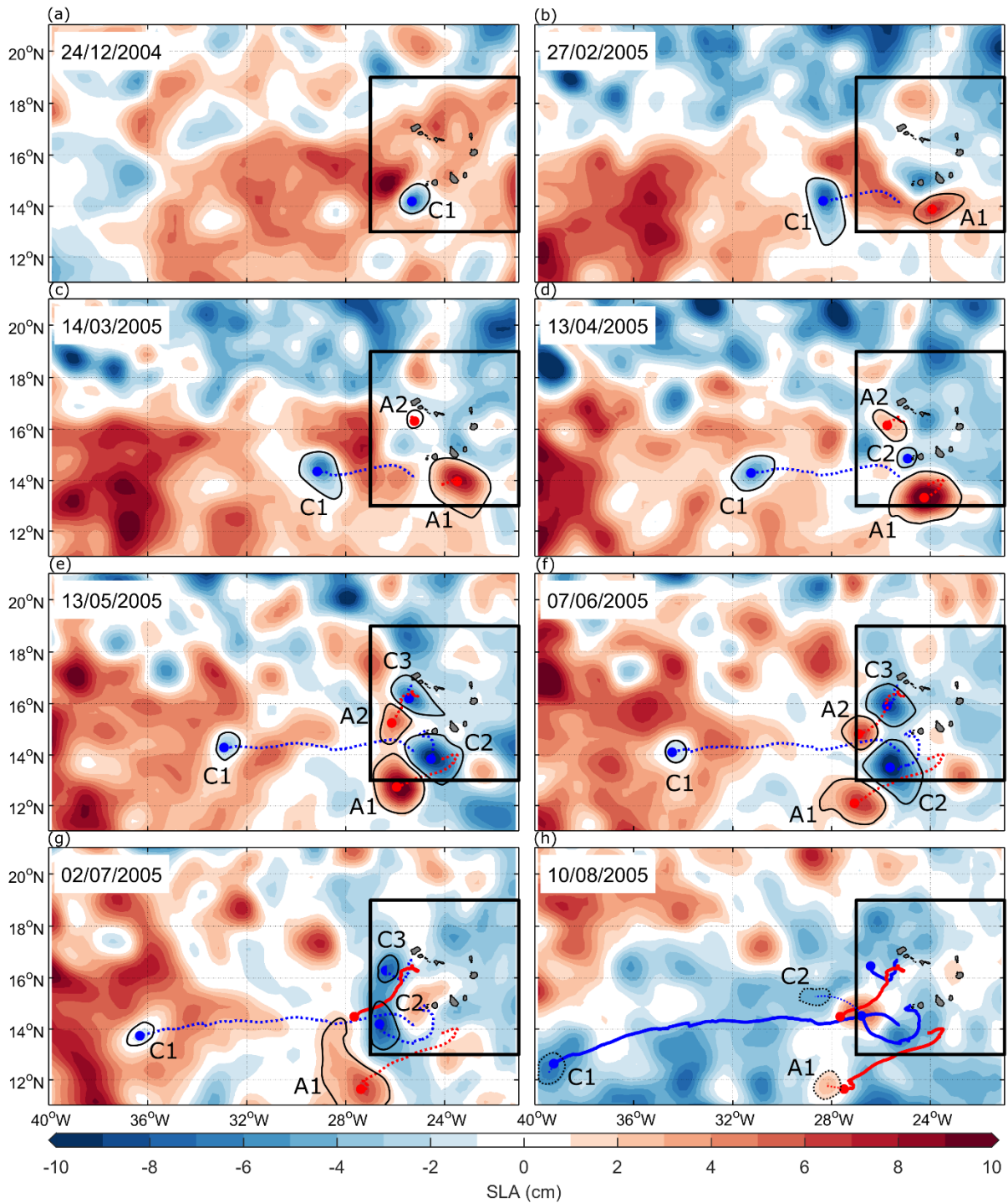
Figure 4.23 – Near-field eddies evolution from 24th December 2004 to 10th August 2005, plotted against SLA maps. Black square represents CV area. Blue and red colours represent cyclonic and anticyclonic eddies, respectively. Doted and solid lines represent active and terminated eddy tracks, respectively; black solid and doted contours represent the active and the transformed eddy delimitation (-2 to 2 cm amplitude), respectively.

4.5. Biological Characterisation

The primary productivity in the vicinity of Cape Verde is further characterised, with the main objective of inferring temporal and spatial patterns, the archipelago susceptibility to remote biological enrichment through far-field features (especially eddies), and the local biological enrichment (IME) through near-field island-induced eddies. For that, three approaches are introduced. First, the seasonal characterisation of the surface Chl*a* concentration in the previously introduced general study area is conducted. Subsequently, a longitude-time diagram (Hovmöller) is presented for the determination of the temporal variation of the Chl*a* extension from coastal to offshore waters. Lastly one specific case of remote enrichment and one specific case of IME are presented and characterised.

The seasonal Chl*a* mean for the study period are represented in Figure 4.24, overlapped by the seasonal mean ocean surface currents. The most obvious pattern is related with the resemblance between the two different datasets, in which the very pronounced seasonal patterns seem to follow each other very closely. During spring, the coastal Chl*a* concentrations reaches its maximum extension offshore, spreading over an approximate 4º (~444 km) length. At the coast, the concentration almost exceeds a remarkable 30 mg.m^{-3}, progressively decreasing to ~0.3 mg.m^{-3} until the longitude of Cape Verde. In the archipelago it is possible to observe a localised Chl*a* enhancement in the immediate proximity of the islands – especially Fogo – of up to 2 mg.m^{-3}. The ocean surface currents have a linear south-westward orientation from the coast to the archipelago, becoming turbulent when intersecting the islands. One cyclonic and anticyclonic dipole feature is observed in the lee of Fogo Island, whereas one cyclonic eddy is observed in the lee of Santo Antão.

During summer, the Chl*a* concentration is pushed northward, concurrently with the northward ocean current at the coast. In fact, the coastal Chl*a* seems to be supressed by the latter, which when intersecting the westward current near Cape Blanc creates a cyclonic gyre which then serves as an export mechanism of Chl*a* to offshore waters. The extension of such mechanism almost reaches the archipelago from northwest, with some fragmentations of the latter with concentrations around 1 mg.m^{-3} getting very close from the easternmost windward islands. In the lee of Fogo Island, a very pronounced anticyclonic eddy is perceivable.

In Autumn, the costal ocean current reaches its northernmost extension. Consequently, Chl*a* concentration is suppressed and pushed northward until it intersects the westward NEC at Cape Blanc (Figure 2.4). However, the extension of the offshore transport, in relation with the previous

season, is considerably shorter. A new – but less pronounced – offshore extension arises near the Cape Vert promontory with concentrations around 2 mg.m^{-3}, though surface currents do not follow the same behaviour.

Lastly in winter, high Chl*a* concentration extend from the coastal zone to offshore, seemingly reaching the archipelago with concentrations at approximately 1 mg.m^{-3}. As expected, the latter seems to be driven by the ocean surface currents, which follow a dominant westward direction. Pronounced patches of high Chl*a* concentration are observed in the vicinity of the archipelago, with values between 1 – 2 mg.m^{-3}. In fact, it is during this season when higher concentration are observed around Cape Verde. However, it is difficult to classify the origin of such enhancement, i.e., from remote or local enrichment.
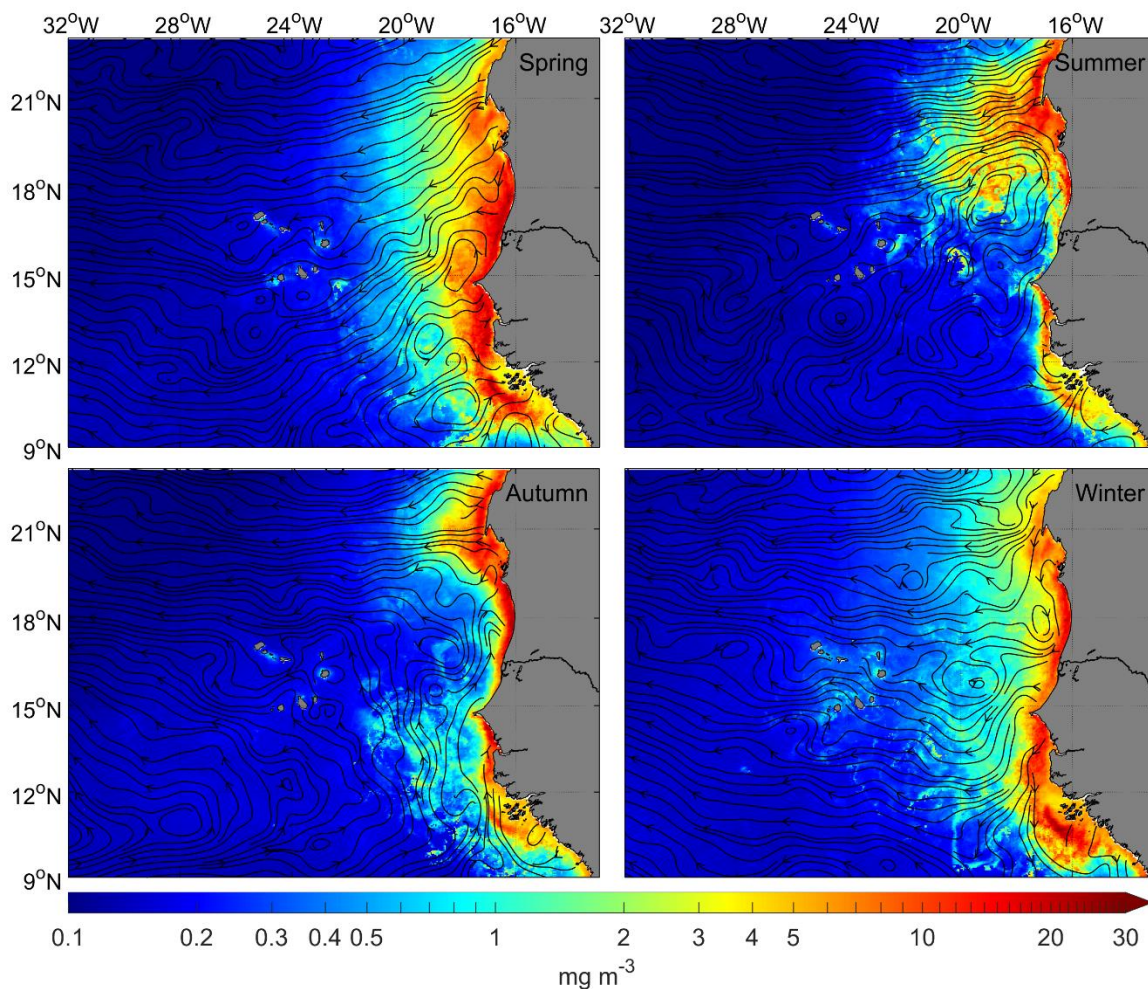
Figure 4.24 – Seasonal Chl*a* surface concentrations (coloured) and currents (streamlines).

The inter-annual extension of the Chl*a* surface concentration from the African coast to offshore is represented in Figure 4.25. As observed in the previous Figure 4.24, a seasonal pattern is well perceivable along the years. Highest concentrations are seen during the first and final months of all the years, with concentrations reaching ~30 and ~1 mg.m^{-3} at the coast and in the longitudes comprising the archipelago, respectively. The extension of the Chl*a* signal reaches the westernmost position in late spring and early summer. At the longitudes between Santo Antão and Boa Vista, highest Chl*a* concentrations take place between January and March, with values in the range of 0.5 and 1 mg.m^{-3}. Tough, there are some exceptions, as it is the case of 2009 and 2014 – when the coastal-offshore Chl*a* export reaches the archipelago during June. The apparent connection between the coastal and offshore Chl*a* concentrations hampers the distinction between remote and local Chl*a* enrichment, making the quantification of the IME inconclusive.
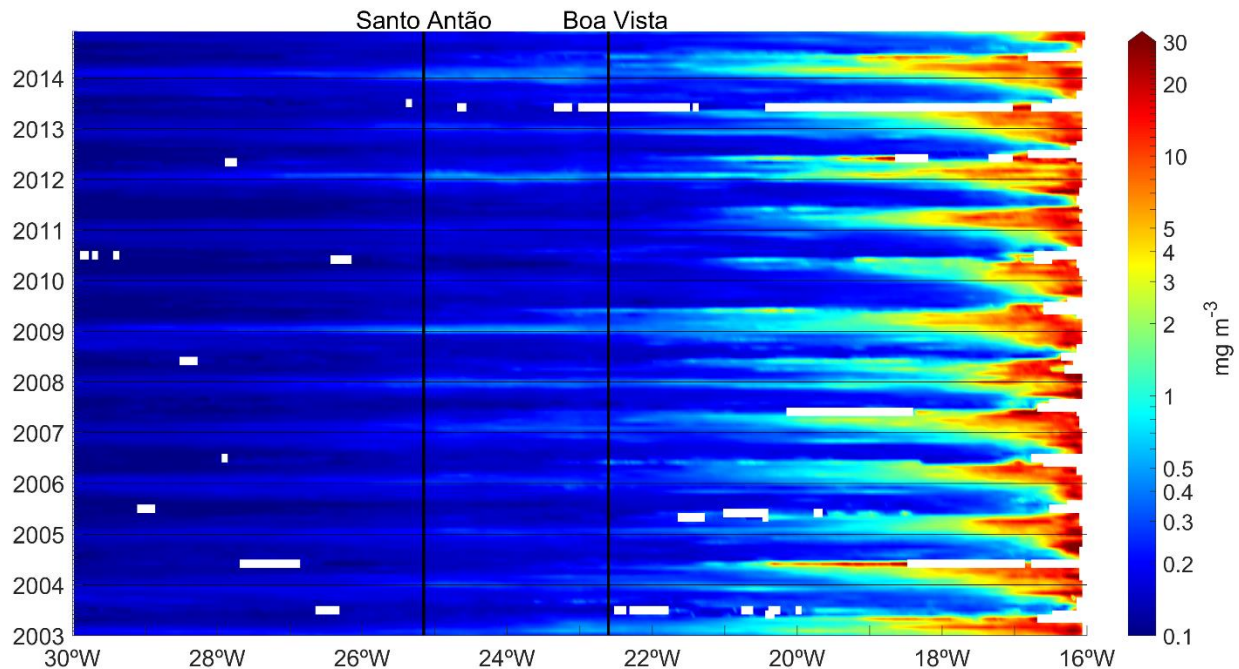
Figure 4.25 – Longitude-time diagram (Hovmöller) of the Chl*a* inter-annual variability, averaged between 13 – 19ºN. Black solid lines represent the longitudinal location of the easternmost (22.6ºW) and westernmost (25.2ºW) islands of the archipelago (Boa Vista and Santo Antão, respectively).

4.5.1. Specific Cases

Having into account the existence of two types of driving mechanisms for the local primary productivity, the periods from October 2013 to March 2014 and from October 2009 to January 2010 were selected, being representative of a remote (Figure 4.26) and local biological enrichment scenario (Figure 4.27), respectively. Nevertheless, it has been observed that both mechanisms can coexist simultaneously. In fact, the interaction of both distinct mechanisms is the most frequent scenario in the region, being virtually impossible to find isolated cases for both mechanisms. In order to facilitate the interpretation, both representations only include the Chl*a* surface concentration, but for the identification of the driving mechanisms responsible for such features, the computation of the mean ocean surface currents was also considered and are included in Annex M:. Furthermore, monthly Chl*a* mean concentrations proved to be the best solution for the current analysis, avoiding large gaps that are provoked by the very frequent cloud cover.

First, the remote enrichment scenario (Figure 4.26) is characterised. In October 2013 it is observed the apparent existence of a coastal filament with high Chl*a* concentration in Cape Blanc. Within its offshore expansion, a fragment (circled in red, possibly an anticyclonic eddy; Annex M.1) detaches from the filament transporting significant Chl*a* concentrations (~ 20 mg.m^{-3}) in the direction of the archipelago. In November 2013, this feature continues propagating in the same direction, though with less pronounced Chl*a* concentrations ($1 - 2$ mg.m^{-3}), while the coastal filament near Cape Blanc retracts. In December 2013, the latter south-westward propagating feature intersects the archipelago, as the Chl*a* concentrations in its vicinity increases substantially in relation to the previous months, reaching values as high as 5 mg.m^{-3}. In the subsequent months, the local Chl*a* concentrations remain constant, with values between $1 - 10$ mg.m^{-3}. Concurrently, the adjacent costal area is marked with enhanced Chl*a* levels, especially near the Cape Vert promontory in February and March 2014. Some coastal filaments extend offshore, almost reaching the archipelago. Nevertheless, it is possible that some fragments reach the islands, promoting local primary production. An interesting Chl*a* signal (circled in light blue) is observed during February 2014 at approximately 28ºW – 13ºN. The latter can be a result of two scenarios: the advection induced by an anticyclonic eddy, or the nutrient injection induced by a cyclonic eddy. However, there are no evidences of such features in Annex M.1, which can be a result of the monthly average applied for the ocean current – as such procedure may indiscriminately filter mesoscale features – or the small eddy size that may not be detectable in the altimetry sensor.
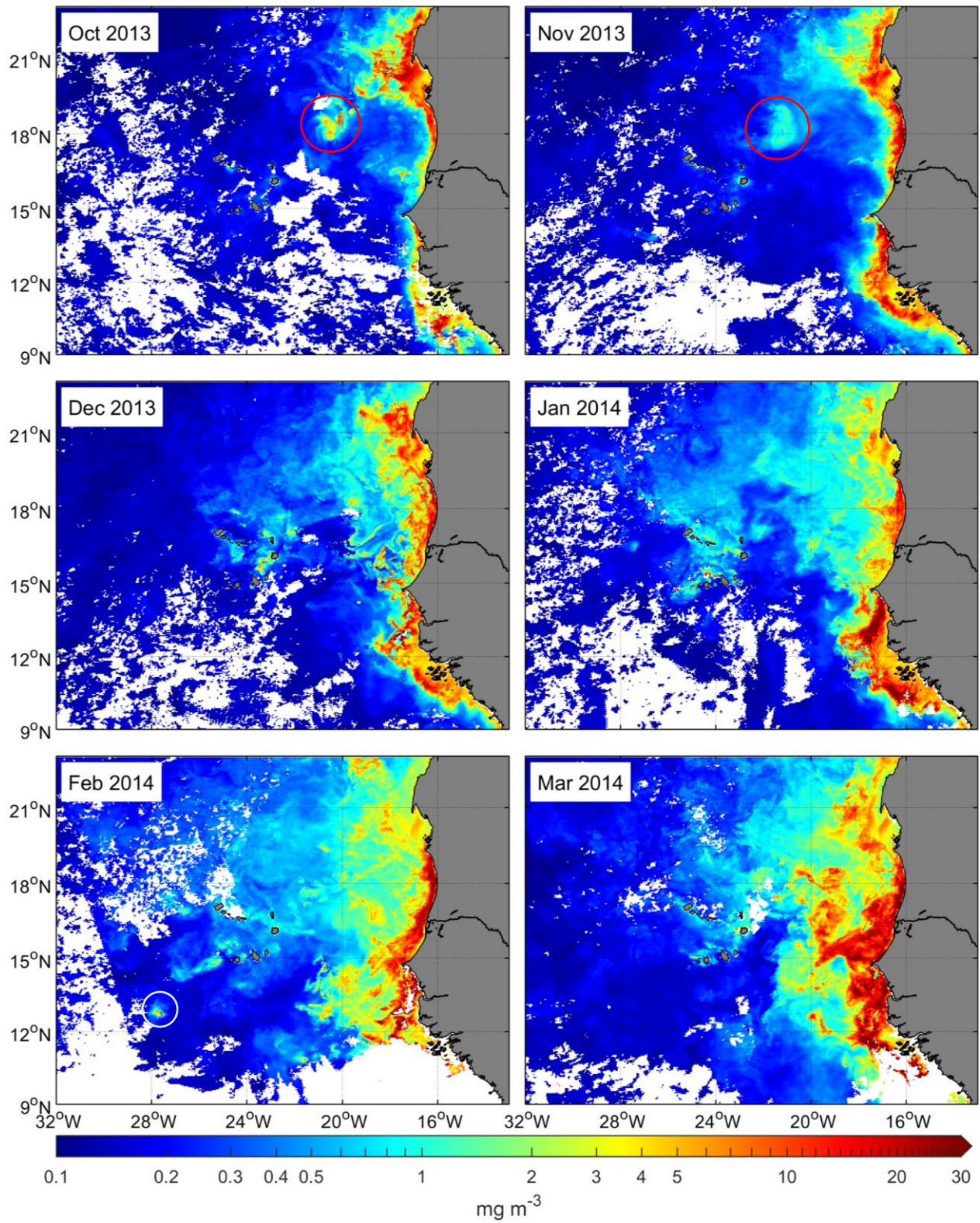
Figure 4.26 – Biological remote enrichment scenario. Monthly Chl*a* means from October 2013 to March 2014. Red and light blue areas represent remote and local enrichment, respectively.

Lastly, the local enrichment scenario is presented in Figure 4.27. One far-field feature (circled in red, possibly an anticyclonic eddy; Annex M.2) is observed in all the months. This patch of high Chl*a* concentrations approaches the archipelago from the northeast, similarly to the previously described remote enrichment case (Figure 4.26), fainting away as it propagates. The most remarkable Chl*a* signal, however, is depicted in the lee of Fogo Island in January 2010 (circled in light blue), reaching values of up to 20 mg.m^{-3}. This signal is only present in January. Moreover, the area in which it arises has been linked to the generation of island-induced eddies in the previous sub-chapters. Therefore, such occurrence may be possibly linked to a punctual and localised biological response to the injection of nutrients from deep layers to the euphotic zone through Ekman-suction.
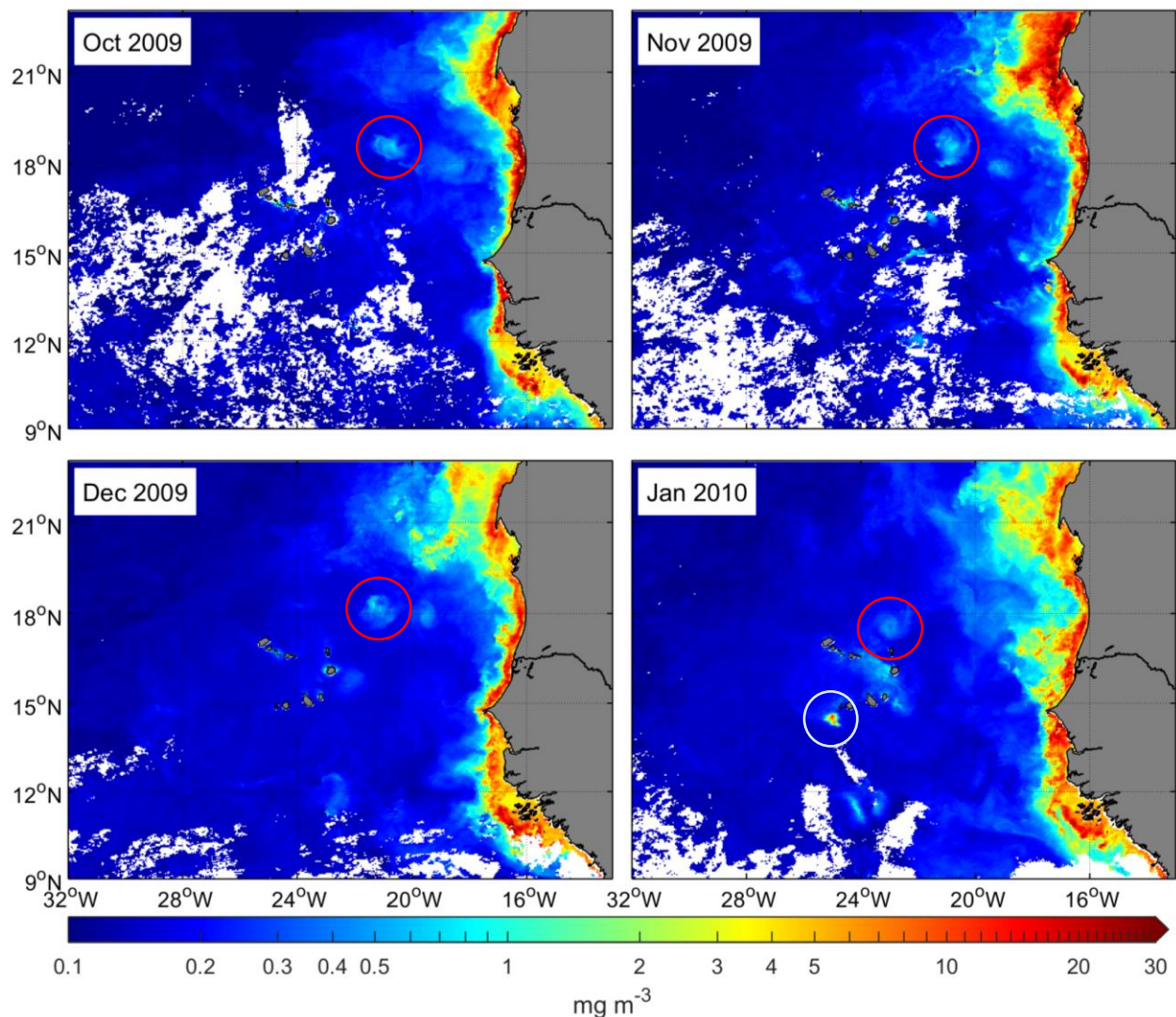
Figure 4.27 – Biological local enrichment scenario. Monthly Chl*a* means from October 2009 to January 2010. Red and light blue areas represent remote and local enrichment, respectively.

5. Discussion

A great deal of results was presented and characterised in the previous chapter, which may lead the reader to be overwhelmed with such an amount of information. Thus, the main objective here is to link and discuss the most meaningful results, so that the big picture can be eloquently retained.

5.1. Eddy Hotspots and Pathways

The identification and characterisation of the predominant eddy birthplaces and pathways is extremely important for several reasons. First, it promotes the knowledge and comprehension of a localised oceanic region (e.g., a group of islands or a specific coastal area), and subsequently its impact on a regional scale. Secondly, it determines with great extension the nature of the eddies being generated there, such as their lifetime and propagation expectancy. Thirdly, it can provide valuable information about the biogeochemical characteristics of the water being transported in the interior of the eddies, which can have a significant impact in whatever comes in their way. Therefore, the far and the near-field eddies are further assessed.

5.1.1. Far-field Regions

Coastal areas have been largely associated with mesoscale variability (Chelton *et al.,* 2011), especially when characterised by an upwelling system (Barton *et al.,* 1998; 2004; Chaigneau *et al.,* 2008). Naturally, the northwest African coastal area is no exception (Mittelstaedt, 1983; Chaigneau *et al.,* 2009, Schütte *et al.*, 2016a).

From current results, it has been observed that the Cape Blanc promontory is marked by an important EKE signal all year round (Figure 4.1), being more pronounced during spring and summer (Figure 4.2). This location is characterised by intense along-slope flow convergence and has been often linked to the generation of a giant filaments and eddies, that promote the transport of cold, nutrient-rich upwelled water to offshore (Van Camp *et al.,* 1991; Gabric *et al.,* 1993; Pelegri *et al.,* 2006; Fischer *et al.,* 2009; Nieto *et al.,* 2012). The latter is further reinforced in Figure 4.26 and Figure 4.27, where a filament appears to give origin to enhanced Chl*a* patches that propagate offshore in the direction of Cape Verde Archipelago. In fact, this region has been recently recognized as a small eddy corridor (Sangrà *et al.,* 2009). The designation of a major eddy hotspot is also supported in Figure 4.4, as the adjacent area holds a considerable number of newly-generated eddies (~200 and ~100 for 1 and 7-day thresholds, respectively) – which in turn is in

good agreement with Schütte *et al.* (2016a). The latter authors detected (in the same region) the generation of at least 50 eddies with a minimum 7-day lifetime and 45-km radius, between 1995 and 2013. The difference in the number of eddy origins between the latter and current studies is very likely related with the eddy-detection method being used, as Schütte *et al.* (2016a) relied on the Okubo-Weiss technique (Okubo, 1970; Weiss, 1991) instead of the SLA-based method (Faghmous *et al.,* 2015a). It is important to note that this hotspot only exists when accounting for short-lived eddies (1 and 7-days thresholds), which leads to the conclusion that it is dominated by short-lived eddies. The latter also means that eddies originated here are very unlikely to reach the Cape Verde Islands, since a short lifetime implies a short propagation range (Figure 4.7). Considering that the archipelago is at a 600-km distance from Cape Blanc, eddies would need to be active for at least ~130 days to be able to reach the islands. This hypothesis is further validated in Figure 4.11, where very few of the represented far-field eddies originate near Cape Blanc.

Cape Blanc also marks the starting point of a very pronounced thermohaline frontal zone, known as the Cape Verde Frontal Zone (CVFZ, Figure 2.4), which separates the salty, warm, nutrient-poor and oxygen-rich NACW from the fresh, cold, nutrient-rich and oxygen-poor SACW (Zenk *et al.,* 1991; Stramma and Siedler, 1998; Zhang *et al.,* 2003; Pastor *et al.,* 2008). This front has been recognized as a major source of mesoscale eddies in the region (Onken and Klein, 1991), being also linked to the generation of the previously referred Cape Blanc filaments (Meunier *et al.,* 2012). Coincidently, it is the starting point of the transversal band of high EKE that goes across the entire zonal length of the tropical Atlantic Ocean, clearly depicted in Figure 4.1. The signal's orientation seems to follow very closely the positioning of the CFVZ – which also goes across the entire Atlantic Ocean (Emery and Meincke, 1986; Lozier *et al.,* 1995) – and the positioning of the westward propagating NEC, which is conversely related with the CVFZ (Zhang *et al.,* 2003). The latter is in good agreement with Reverdin *et al.* (2003), who state that major current systems are an important source of EKE – especially in regions less affected by topography – and are thus important sources of eddies (Pond and Pickard, 1983). This also explains the reason why the southernmost latitudes present extremely high EKE (to the point that a different colour scale had to be implemented, Figure 4.1 and Figure 4.2), directly linked to the presence of the NECC (Figure 2.4, Lázaro *et el.,* 2005).

In the area between Cape Vert and Cape Timiris promontories, the EKE increases significantly in summer (Figure 4.2), merging the Cape Blanc branch at higher latitudes. This happens

concurrently to the maximum intensification and extension of the MC (Figure 2.6, Mittelstaedt, 1991, Lázaro *et al.,* 2005). Schütte *et al*., 2016a strongly associated the latter current to the formation of eddies that propagate westward in the direction of Cape Verde. Furthermore, the latter authors designated this season as the period of maximum eddy generation at the coast, and linked the eddy generation mechanisms to the dynamic instabilities associated with MC. This is further confirmed in the seasonal eddies origins (≥ 30 days) representation (Figure 4.5). Hence, this area can be defined as a seasonal hotspot for medium and long-lived far-field eddies[9]. In fact, two of the selected far-field eddies approaching the archipelago (C1 and A5, Figure 4.15) originate during this season. According to Schütte *et al*., 2016a, coastal-generated eddies created in June normally intersect the archipelago between boreal winter and spring. The latter is in good agreement with Figure 4.13, as most of the eddy signatures are perceivable during that period, though some are perceivable earlier in late Autumn (as it is the case of the previously referred C1 and A5 eddies) – which in turn is related to the fact that the latitudinal cross-section is 2º (~222 km or ~40 days travel time – Figure 4.7) east from the easternmost islands.

Notwithstanding, an interesting EKE trail starting in the immediate vicinity of the Cape Vert headland is observed in winter – when the northwest African upwelling system reaches its southernmost extension (Van Camp *et al.,* 1991; Nykjær and Van Camp, 1994; Lázaro *et al.*, 2005) – possibly indicating an important far-field eddy pathway in the direction of the leeward group of islands (Figure 4.2). Several medium and long-lived eddies have been observed to originate in this location (Figure 4.4) – especially during winter (Figure 4.5) – being most of them of anticyclonic nature (Figure 4.6c)[10]. In this case, it is reasonable to assume that these eddies can transport nutrient and Chl*a*-enhanced water at their cores, which in turn must have a direct impact on the archipelago's biological realm. Alpers *et al.* (2013) documented the formation and evolution of a sub-mesoscale (not detectable on altimetry sensors) cyclonic eddy generated by the headland topographic effects on the wind. This eddy transported upwelled nutrient rich water through approximately 200 km offshore, causing a phytoplankton bloom in oligotrophic waters, until it disintegrated 31 days after being generated. Schütte *et al*., 2016a also documented a substantial number of eddies being generated near Cape Vert, in which cyclonic and anticyclonic eddies

---

[9] Coastal-generated far-field eddies can only be medium and long-lived eddies, since coastal-generated short-lived eddies do not reach the archipelago (Annex C.1 andAnnex C.2).

[10] In fact, all the 4 long-lived far-field eddies originated in this area are anticyclonic (Figure 4.11).

dominated the areas north and south/southwest of the headland, respectively. Having into account that the latter authors used a 7-day minimum lifetime threshold, their results are consistent with the current study, when applying an equal threshold (Annex E.1).

5.1.2. Near-field Regions

From the far-field to the near-field, the CV area is further discussed. Deep ocean islands have been reported to induce significant disturbances in the adjacent environment (e.g., Xie *et al.,* 2001; Chavanne *et al.,* 2002), ultimately resulting in the generation of mesoscale eddies (e.g., Sangrà *et al.,* 2005; 2007; 2009; Jia *et al.,* 2011; Caldeira *et al.,* 2014) and consequent nutrient injection and phytoplankton blooms in presumably oligotrophic environments (e.g., Simpson and Tett, 1986; Arístegui *et al.,* 1994; Basterretxea *et al.,* 2002; Hasegawa *et al.,* 2004; 2009). The occurrence of mesoscale eddies in the immediate proximity of the Cape Verde archipelago have seldom been documented (Lázaro *et al.,* 2005; Chaigneau *et al.,* 2009; Schütte *et al*., 2016a) and the mechanisms supporting such features remain to be investigated. By contrast, such mechanisms have been subject of intense studies in other regions, mainly in the Hawaii (Calil *et al.,* 2008; Yoshida *et al.,* 2010; Jia *et al.,* 2011), Canary Islands (Arístegui *et al.,* 1997; Sangrà *et al.,* 2007; Jiménez *et al.,* 2008) and Madeira Island (Couvelard *et al.,* 2012; Caldeira *et al.,* 2014). Curiously, remarkable similarities can be found between these archipelagos and Cape Verde, in the sense that all groups are characterised by high topography – which in turn is well above the local inversion layer (Chavanne *et al.,* 2002; Hafner and Xie, 2003) –, and are exposed to constant incident trade winds. Notwithstanding, the current case of Cape Verde differentiates from the previous studies in one particular – but extremely relevant – way. Such studies focused on the mechanisms and implications induced by the islands themselves – being by atmospheric or oceanic effects (or both) – but very few have considered the implications of the interaction between far-field eddies and island-induced eddies. Considering the archipelago's exposure to such incoming features, it is thus reasonable to expect that some of the near-field eddies may be a product of the inevitable interaction between incoming far-field eddies and the islands. In that sense, the Cape Verde archipelago represents an exceptional case study, which should be regarded with caution.

Considering the size of the delimited CV area in relation to the general study area, the number of medium and long-lived near-field eddies is quite remarkable (Figure 4.4; Table 4.1). The lee of Fogo and Santo Antão Islands – the highest of the archipelago, with 2829 and 1979 meters altitude,

respectively (Figure 2.2; Annex A.1) – are undoubtedly the most pronounced eddy hotspots (Figure 4.4c and Figure 4.4d). However, these regions were only distinguished from the surrounding environments when applying a 30 and 60 lifetime threshold. This may be evidence that many spurious features were identified by the eddy tracking algorithm, hence the need for filtering the dataset and analysing only the most robust eddies. Such pattern is also depicted in the near-field long-lived eddy trajectories and origins representation (Figure 4.17), where anticyclonic eddies appear to be dominant (Table 4.1) – which is in agreement with Chaingneau *et al.* (2009) observations in the lee of Cape Verde and is also a characteristic in other regions (e.g., Sangrà *et al.,* 2009; Chelton *et al.,* 2011). According to Cushman-Roisin *et al.* (1990), this dominance is related to the fact that anticyclonic eddies are generally more robust and merge more freely than cyclones, and cyclonic eddies show a higher tendency for self-destruction. These near-field eddy hotspots are in perfect agreement with Schütte *et al.* (2016a), in which the areas previously referred are defined as the most prominent eddy hotspots away from the African coast. Furthermore, near-field eddies have in general higher lifetime and translation distance than far-field eddies (Figure 4.3 and Annex G.1). On the other hand, far-field eddies are associated with higher values for the eddy translation speed, diameter and amplitude (Figure 4.8, Figure 4.9 and Figure 4.10). These patterns are very likely associated with the fact that far-field eddies can be found in lower latitudes, which in turn influences such kinematic parameters (further discussed in the following chapter).

Near-field eddies that are effectively generated by atmospheric effects should follow an identical seasonal behaviour as the wind. The prevailing northeast trade winds which affect the archipelago are under the direct influence of the seasonal migration of the ITCZ (DGA, 2003, Lázaro *et al.,* 2005). As such, strong and steady winds are recurrent between December and May, while the remaining months are characterised by low intensity winds (Figure 2.3; Varela-Lopes and Molion, 2014). Naturally, such seasonal variation must be reflected in the wind stress curl (Figure 5.1). Dipoles of positive (upwelling) and negative (downwelling) curl appear in the lee of all the major islands, being spring and winter the seasons with the highest extension and intensity. The long-lived near-field eddy origins and trajectories are also represented in Figure 5.1. Most eddies are clearly created during the periods of highest wind intensity – especially in the leeward islands, where the wind regime is more constant (DGA, 2003) – further reinforcing the possibility that atmospheric-effects are indeed a key factor in the generation of such features.
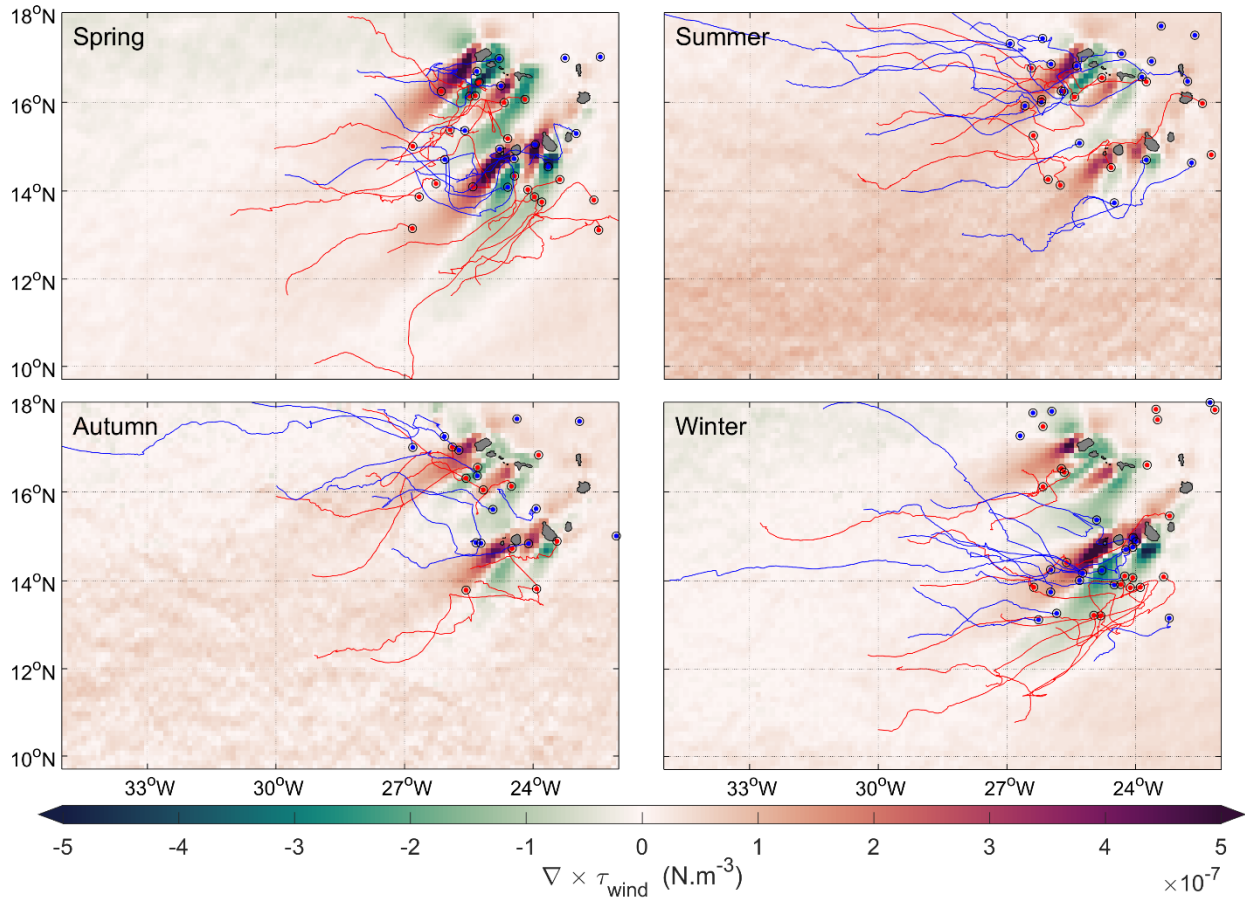
Figure 5.1 – Seasonal average wind stress curl in Cape Verde Archipelago, overlapped by the long-lived near-field cyclonic (blue) and anticyclonic (red) eddy trajectories. Circled points represent the place of origin, but only the ones generated in the lee of the islands have a trajectory.

Predictably, several very pronounced seasonal EKE signals are present in the immediate proximity of the leeward islands during spring and winter, though a less intense EKE signal is also perceivable during autumn (Figure 4.2). One remarkable EKE signal is perfectly depicted northwest of Fogo Island, with a circular and elongated shape in spring and winter, respectively (Figure 4.2). The almost perfectly circular shape may be evidence of a recurrent eddy generation signature in spring, while the elongated shape in winter is very likely to be an evidence of the previously described far-field eddy pathway which originates near the Cape Vert promontory. In fact, part of this far-field eddy pathway seems to merge the elongated EKE signal observed north off the leeward islands through the João Valente Bank (between Boa Vista and Maio Islands, Figure 2.1). Furthermore, the specific case of a far-field eddy interaction with the easternmost islands reinforces this theory (Figure 4.15 and Figure 4.16). Hence, the combination of an eddy hotspot and pathway is the most probable designation for the area, which in turn gives rise to the possibility

of a major pathway for far-field eddy transformation, merging and splitting. The same can also resonate for the second remarkable EKE signal perceivable south of the leeward islands during spring and winter (Figure 4.2), also characterised by a seasonal varying shape. In winter, the other part of the previously referred far-field eddy pathway merges this EKE signal from the south, which can in the same manner represent an important pathway for far-field eddies. However, island-induced eddies through atmospheric effects are also strongly associated with this region. Thus, the interaction between far-field and near-field eddies and possible island-induced forcing mechanisms is very likely to occur. In accordance with these findings, Lázaro *et el.* (2005) linked the presence of high EKE values in the lee of Fogo Island to a nearly permanent anticyclonic eddy, which reached maximum speeds in spring. More recently, García-Weil *et al.* (2014) observed a remarkable EKE signal in the same location while characterising the mesoscale dynamics in the Canary Islands. Curiously, this signal was significantly more pronounce than in the lee of Canary Islands, but did not receive any attention.

In the current study, the EKE signal downwind of the southernmost islands takes a very interesting shape in spring (Figure 4.2). With an initial southwest orientation, turning west in the final segment, this conspicuous structure follows very closely the long-lived anticyclonic eddy trajectories evident in Figure 4.17 (and in Annex C.4, where a threshold of 90 days is applied), which in turn resemble with great detail the Canary Eddy Corridor described by Sangrà *et al.* (2009). The latter authors presented strong evidences that the wind-shadow effect induced by the Canary Islands plays a key role in the generation of long-lived[11] eddies, which initially propagate southward and then deflect westward. Furthermore, the authors also suggested that similar long-lived eddy corridors could be present in other oceanic regions, referring to the Hawaiian case as an example (Calil *et al.,* 2008). Hence, there are strong possibilities that this major near-field long-lived eddy pathway identified south of Cape Verde can be an important long-lived eddy corridor. However, such assumption requires further investigation.

---

[11] The authors defined a 90 days minimum lifetime threshold for the designation of long-lived eddies.

5.2. Eddy Propagation Characteristics

Throughout the study it has been observed that all long-lived near and far-field eddies propagate westward, with small meridional deflections along the way (Figure 4.11, Figure 4.12, Figure 4.17 and Figure 4.18). It has also been observed that the propagation speeds and radius are highest at lower latitudes (Figure 4.6d), patterns which have been extensively documented in the past. The westward propagation speed for long-lived eddies was found to be remarkably close to the phase speeds of nondispersive baroclinic Rossby waves (Chaingneau *et al.,* 2009; Chelton *et al.,* 2011), which in turn increases towards the equator as a function of the planetary vorticity gradient effect (known as the β-effect, Cushman-Roisin *et al.,* 1990; Van Leeuwen, 2007). In fact, it was recently demonstrated that eddies often propagate westward in the crests and troughs of a planetary Rossby wave, mostly in lower latitudes (Polito and Sato, 2015). Furthermore, the influence of the local planetary rotation rate on the propagation of an eddy is directly proportional to the eddy's diameter (Cushman-Roisin *et al.,* 1990). Hence, the higher the eddy's size, the higher the influence of the β-effect.

Present results also indicate that cyclonic eddies tend to deflect northward, while anticyclonic eddies deflect equatorward (Figure 4.12 and Figure 4.21). This general behaviour has been globally (Chelton *et al.,* 2011), regionally (Morrow *et al.,* 2004; Chaigneau *et al.,* 2009; Cheng *et al.,* 2014) and locally (Calil *et al.,* 2008; Sangrà *et al.,* 2009) observed in past studies, and is strongly associated with the combination of the β-effect and self-advection by nonlinearity (Chassignet and Cushman-Roisin, 1991; Chelton *et al.,* 2011), in which by the metric of U/c, U is the maximum eddy swirl surface velocity and c is the respective translation speed (Chelton *et al.,* 2011; Schütte *et al.,* 2016a). The latter also provides information about the efficiency of an eddy to trap water in its interior. As such, $U/c > 1$ indicates that fluid is advected within its interior and the exchange of water with the surrounding environment is reduced (Chelton *et al.,* 2011). Although the computation of nonlinearity was considered in the current study, the latter was not possible to calculate. An issue regarding the eddy swirl speed – which the algorithm determines by estimating the geostrophic surface current through the SLA dataset (Faghmous *et al.,* 2015a) – was detected, as three bands of significantly high values were present in the region, while the remaining areas were characterised by values close to 0 (Annex N:). Such behaviour is not possible to occur in the real world, since an eddy with null rotational speed would rapidly disintegrate. Several attempts were performed in order to solve this issue, but no solution was found. Nevertheless, Chelton *et*

al. (2011) determined that almost 90% of the long-lived eddies (lifetime ≥ 16 weeks, or 112 days) within the tropical band (20ºS – 20ºN) were nonlinear, and all eddies outside this band were highly nonlinear. Furthermore, Schütte *et al.* (2016a) determined that all eddies (lifetime ≥ 7 days and radius ≥ 45 km) detected in the Cape Verde region were also nonlinear. Thus, considering the substantial similarities between the latter and the current study, it is assumed that all detected medium and long-lived far and near-field eddies are nonlinear, and thus it is suggested that the respective cyclonic and anticyclonic preference for poleward and equatorward meridional deflection is associated with such characteristic.

The propagation of mesoscale eddies can still be influenced by many other factors, especially in an eddying environment such as Cape Verde. The eddy-eddy interaction has been suggested to have a substantial influence on the propagations of such features (Calil *et al.,* 2008; Sangrà *et al.,* 2009). A remarkable example is observed in the specific case of near-field eddies evolution (Figure 4.23), where the C2 and C3 cyclonic eddies appear to propagate southward in the initial phase, following the same pattern as the nearby A1 and A2 anticyclonic eddies. As A1 and A2 propagate further away from the C2 and C3, the cyclonic eddies deflect westward and northward before terminating. Such behaviour in cyclonic eddies was also observed by Lumpkin (1998), where the advection by nearby anticyclonic eddies was attributed as the main cause.

The background flow in which an eddy propagates can also have important implications. Sangrà *et al.* (2009) suggested that the CC was responsible for the initial southward propagation of the anticyclonic eddies forming the Canary Eddy Corridor, which then drifted out of the CC and deflected westward as they became large enough for self-advection due to the β-effect. Furthermore, it has been demonstrated that the westward Pacific NEC can modify the propagation characteristics of island-induced eddies in the lee of Hawaii (Lumpkin, 2008; Calil *et al.,* 2008), being even able to increase their translation speeds in favourable conditions (Holland and Mitchum, 2001). Considering that eddies generated or modified by the Cape Verde Archipelago propagate in the direction of the Atlantic NEC, which has similar characteristics as the Pacific NEC, it is expected that the latter can also have an effect in the propagation of such features. Nevertheless, this is merely speculative and further investigation should be conducted regarding this issue.

The wind, besides having an important role on eddy generation, can also influence their propagation. As previously observed, the area downwind of the leeward islands is marked by an extensive dipole wind stress curl signal, reaching approximately 12ºN (~ 300 km distance from

Fogo Island) in spring and winter (Figure 5.1). Besides Chavanne *et al.* (2002), such far-reaching atmospheric effects were documented by Chelton *et al.* (2004) when revealing the existence of persistent small-scale features in the global ocean, arguing that these previously unresolved features could have a substantial impact on the ocean. Curiously, the trajectories within the major anticyclonic eddy pathway downwind of the leeward islands seem to follow very closely the wind stress curl bands, especially in the negative (green) wind stress curl area (Figure 5.1). This can be an indicator of wind-mediated eddy-confinement, first introduced by Coulevard *et al.* (2012). In an exceptional novel approach, the latter authors showed strong theoretical evidences that eddies generated by wind shear leeward of Madeira Island were "trapped" in the wind-wake region, as the cyclonic and anticyclonic eddies propagated through the positive and negative wind stress curl bands, respectively. This phenomenon also seems to occur in the lee of Cape Verde, especially when looking at the specific case of the near-field anticyclonic eddies propagation plotted against the wind stress curl (Annex P.1). The A1 and A2 anticyclonic eddies propagate south-westward following the same orientation as the negative wind stress curl (green), while the C2 and C3 cyclonic eddies show a different behaviour, which is very likely related with the interaction with A1 and A2 (discussed earlier). Therefore, it is strongly suggested that the wind-wake may be an important contributor to the containment of the oceanic eddies in the lee of Cape Verde Archipelago.

5.3. Far-Field Eddy-Island Interaction

The eddy propagation in the ocean is directly affected by topography, as the trajectory and structure of such features is prone to modifications driven by the interaction with a continental slope, a seamount or an island (Yang *et al.,* 2016). As previously discussed, many of the eddies generated at the African coast often intersect the archipelago while propagating westward to offshore waters. Such eddies have recently been subject of numerous studies, in which the hydrographic (Schütte *et al*., 2016a) and biogeochemical (Fischer *et al.,* 2016; Fiedler *et al.,* 2016; Hauss *et al.,* 2016; Karstensen *et al.,* 2015; Löscher *et al.,* 2015; Schütte *et al*., 2016b; Romero *et al.,* 2016) properties were extensively characterised. However, the implications of the interaction of such features with the Cape Verde Archipelago has, to present date, received no attention. To current knowledge, most studies regarding the eddy-island interaction were conducted under laboratory (e.g., Cenedese, 2002; Adduce and Cenedese, 2004; Cenedese *et al.,* 2005; Tanabe and

Cenedese, 2008; Andres and Cenedese, 2013) and model (e.g., Simmons and Nof, 2000; 2002; Stern, 2000) experiments, but empirical case studies are extremely rare (Chang *et al.,* 2012). In an idealized case, Stern (2000) was able to simulate the splitting of an eddy when colliding with an island, a phenomenon which is believed to result in the transfer of energy, momentum, salinity and temperature to the surrounding environment through small, dissipative scales (Simmons and Nof, 2000, Cenedese *et al.,* 2005). More recently, Chang *et al.* (2012) described the collision between two anticyclonic eddies with Dongsha atoll, which resulted in the weakening/termination of the stronger eddy and in the splitting of the weaker one. Nonetheless, Yang *et al.* (2016) argues that the phenomenon of eddy-splitting – such as the one previously reported by Chang *et al.* (2012) – lacks sufficient observational data to systematically describe such process, and suggests that further empirical investigation must be conducted to better comprehend such phenomenon.

From the previously observed far-field eddy trajectories (Figure 4.11), the Cape Verde Archipelago appears to act as an extremely effective barrier, as no far-field eddy trajectory is observed to overcome the islands. From these results, one may deceptively assume that all far-field eddies terminate when intersecting the archipelago. However, this is far from reality. From the analysis of the supplementary material, it is observed that most of these eddies undergo through complex transformation processes which give rise to (supposedly) new eddies in the opposite side. Thus, the most accurate way of perceiving such results is by assuming that no long-lived far-field eddy is able to keep its original form and kinematic properties when intersecting the archipelago. From the visual analysis of the sequential SLA maps and eddy trajectories (supplementary material), it was possible to determine that, for a total number of 74 long-lived far-field eddies: 45 (61 %) were terminated without interacting directly with the islands; 13 (18 %) underwent a transformation process which made the eddy tracking algorithm to falsely identify such features as newly-generated eddies; 7 (9 %) were destructed without leaving a trail; 5 (7 %) resulted in eddy splitting, giving rise to 11 new near-field eddies; and 4 (5 %) were deflected and kept propagating in a different direction. Some specific cases of such interaction were selected, where the transformation of two anticyclonic eddies and the splitting of one cyclonic eddy are presented (Figure 4.15 and Figure 4.16).

The case of the A2 far-field eddy is quite interesting. As the anticyclonic eddy intersects the windward islands from the northeast, another eddy of the same polarity forms on the opposite side. Consequently, a streamer appears to detach from the impinging A2 eddy and flows

counterclockwise around the islands, joining the body of the newly generated A4 eddy. However, it has been observed in laboratory experiments that, as a streamer detaches from the eddy when intersecting an island, it flows along the island's perimeter in the same direction as the eddy's flow (Andres and Cenedese, 2013). This means that, as an anticyclonic eddy rotates in the clockwise direction, it is expected that the resulting streamer flows around the island in the same clockwise direction. Hence, the specific case of A2 is contradictory to past studies.

Nevertheless, one most consider that this is far from an idealized case, as several other factors can influence such interaction. After a detailed analysis of the sequential SLA maps (supplementary material), a new hypothesis arises: The A4 is very likely to be a result of the atmospheric or oceanic shedding effects induced by the windward islands, as early signs of formation emerge before the A2 interaction with the islands. If this is the case, part of the impinging A2 far-field eddy merges the newly generate A4 eddy – a recurrent phenomenon between anticyclonic eddies (Cushman-Roisin *et al.*,1990) – giving the false impression that the A4 is a direct result of the A2 eddy-island interaction, though it may also be an important factor. As a cautionary note, such assumption should be regarded as speculative and – as Dong and McWilliams (2007) suggested – further studies should be conducted to better understand the physical processes occurring in a real oceanic island wake and thus better comprehend the implications of far-field eddies in the generation of island-induced eddies.

Another interesting case occurred approximately at the same location. The A3 anticyclonic far-field eddy approaches the windward islands and is considered terminated by the tracking algorithm after intersecting Santo Antão, though most of the SLA body remains present. It is very likely that the latter is related with the consequent modification of shape and associated kinematic properties. The A6 anticyclonic eddy arises a few kilometres southwest, which is undoubtedly a product of the A3 eddy-island interaction. In fact, the most appropriate designation of such feature should be A3.1. The cases of A2 (former) and A3 (latter) are very likely to be a recurrent phenomenon in the windward region, as a very pronounced EKE signal is observed exactly in the same location, especially in spring and summer (Figure 4.2), Hence, it is possible that the very pronounced eddy hotspot observed in the lee of Santo Antão (Figure 4.4c and 4.4d) might be a combination of island-induced eddies and the transformation of far-field incoming eddies.

However, the most remarkable eddy-island interaction case is associated with the C1 far-field cyclonic eddy which arises north of the Cape Vert promontory, along with the A5 anticyclonic

eddy. In contrast with A5 – which is deflected southward and terminates before intersecting the archipelago – C1 intersects the easternmost islands. Consequently, the eddy perimeter interacts with Boa Vista Island, drastically changing the propagation speed and trajectory of the latter – a behaviour which is consistent with past studies. Yang *et al.* (2016) demonstrated that the topographic effects on an eddy were felt at some distance away from an obstacle, which lead to a notable change in the eddy propagation. The latter was also observed by Chang *et al.* (2012), as an anticyclonic eddy weakened at a 30-120 km distance from the Dongsha atoll.

It is worth mentioning that the Cape Verde Archipelago is constituted by 2 main chains of islands with relatively shallow depths between them (except between Fogo and Santiago Islands, Figure 2.1). Such geomorphological disposition may lead the easternmost islands to act as a single attached edifice, obstructing the westward propagation of incoming eddies. The latter seems to be the case for C1, as the eddy is deflected southward when intersecting the João Valente bank between Boa Vista and Maio Islands (Ramalho, 2011) – a behaviour that was also observed in an idealised case (Andres and Cenedese, 2013). As the eddy stays approximately stationary, a streamer detaches from the eddy flowing in the counterclockwise direction along the northern side of the leeward islands, giving rise to the cyclonic eddy C2. According to Andres and Cenedese (2013), this kind of streamers are governed by the conservation of circulation momentum around the islands, which in turn results in a jet-like current between the island passage and the generation of other eddies downstream (Cenedese *et al.,* 2005).

As C2 increases in amplitude and size, a streamer is peeled off from the eddy, originating another cyclonic eddy southwest of Fogo Island (C3). Nevertheless, and following the same hypothesis as the previously discussed A4, the generation of C3 can also be influenced by atmospheric island-induced disturbances, since it occurs during the period of highest wind intensity (DGA, 2003; Varela-Lopes and Molion, 2014) at a location where positive wind stress curl (strongly associated with cyclonic eddies, Chavanne *et al.,* 2002) is often very pronounced (Figure 5.2). While strong evidences suggest that C2 is a direct product of the C1 intersection with the islands, it is likely that C3 arises from interaction of C2 with Fogo Island, which in turn is intensified by the wind shear effect provoked by same island. If this is in fact the case, this phenomenon further reinforces the idea that near-field eddy generation in Cape Verde is a rather complex phenomenon, which deserves special attention and should be regarded with caution – as a variety of factors, never documented elsewhere, are at work.
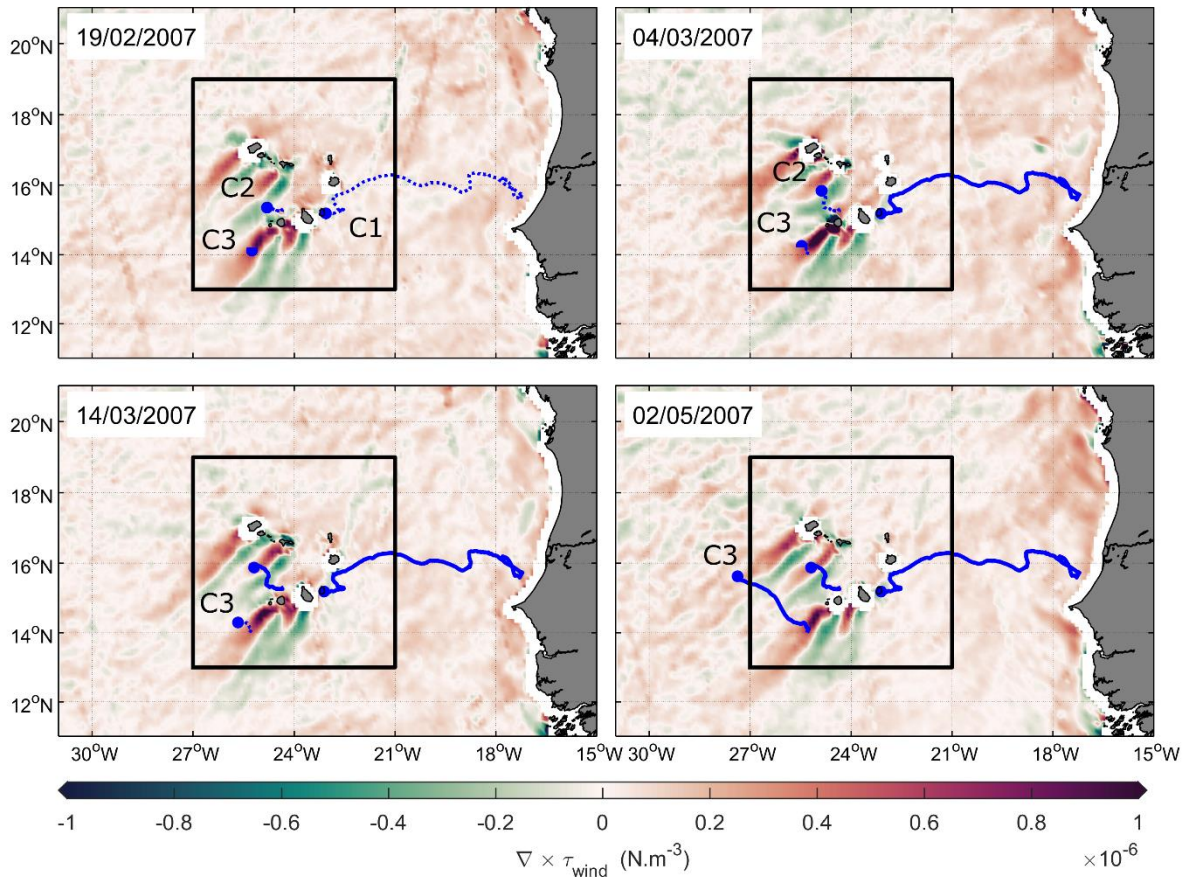
Figure 5.2 – Representation of the specific C3 eddy generation, plotted against wind stress curl (averaged from 8 days prior to respective date). Black square represents CV area. Doted and solid lines represent active and terminated eddy tracks, respectively.

5.4. Biological Implications

The enhancement of biological primary production – especially phytoplankton – is largely associated with the supply of nutrients into the euphotic zone (Arístegui *et al.,* 2007). According to past studies, such nutrient availability in the region is mostly regulated by 3 mechanisms. First, the seasonal coastal upwelling in the western African coast stimulates phytoplankton growth (Figure 4.24, Demarcq and Samoue, 2015), which sometimes reaches the Cape Verde Archipelago through ocean current or filament advection (Figure 4.25, Fernandes *et al.,* 2005; Lathuilière *et al.,* 2008). In fact, it has been estimated that half of the total upwelled water between 17-23ºN flows across the upwelling front in filaments (Kostianoy and Zatsepin, 1996). Second, atmospheric deposition of iron-rich Saharan dust can intensify phytoplankton growth, though with less pronounced implications (Lange *et al.,* 1998; Pradhan *et al.,* 2006; Ohde and Siegel, 2010; Fischer *et al.,* 2016). Finally, nutrient injection (advection) induced by cyclonic (anticyclonic) coastal-generated eddies can sustain enhanced levels of Chl*a* at its core, transporting such unique

87

environments (Alpers *et al.,* 2013, Fischer *et al.,* 2015; Löscher *et al.,* 2015; Karstensen *et al.,* 2015) and possibly impacting the archipelago in their transition to offshore waters. All these distinct mechanisms have one thing in common – the place of origin. Hence, their implication to the archipelago can be regarded as remote (far-field) biological enrichment. Notwithstanding, a new driving mechanism – which to present date has only been hypothesized in the region – is proposed: the island-induced biological enhancement through eddy-induced Ekman suction of deep nutrient-rich water to surface layers, a phenomenon often linked to the IME (Caldeira *et al.,* 2002). However, IME has often been regarded as an isolated mechanism, exclusively induced by the islands on the local environment (Gove *et al.,* 2016). The present study challenges this idea, as the combination of both remote and local mechanisms is the most accurate way of characterising the archipelago's biological realm.

The representation of surface Chl*a* concentration in two specific periods of time substantially supports this theory (Figure 4.26 and Figure 4.27). The main objective was to characterise isolated cases of remote and local enrichment, though it was virtually not possible since both mechanisms are detected in both periods and appear to work simultaneously. Nevertheless, some isolated features were identified, as it is the case of a large Chl*a* patch which detaches from the extensively studied "giant filament" of Cape Blanc (Figure 4.26). Despite the non-identification of an eddy by the tracking algorithm and the difficulty in assessing the structure's nature with the ocean currents representation (Annex M.1), Löscher *et al.* (2015) demonstrated that this feature was in fact an anticyclonic eddy, characterised by high Chl*a* concentrations at the surface and abnormally low dissolved oxygen (DO) concentrations at near-surface layers. The eddy then intersected the archipelago and a significant increase in Chl*a* concentration emerged in its vicinity. Another similar case is observed in Figure 4.27. The tracking algorithm identified this feature as an anticyclonic eddy generated near the Mauritanian coast, though its trajectory was interrupted as it propagated westward (Figure 5.3) – most likely due to eddy pulsation, as suggested by Sangrà *et al.* (2005). Following its trajectory, the eddy is diverted slightly to north as it interacts with the windward islands and continues propagating west. This anticyclonic eddy was documented by Karstensen *et al.* (2015), who also detected severe hypoxic conditions (20 μmol.kg^{-1}) at the ~120-m depth when it intersected the Cape Verde Ocean Observatory mooring, north of the leeward islands. Such DO depleted eddies are now thought to be recurrent in the region, and are very likely related with

phytoplankton blooms and subsequent sinking of detritus, which induces oxygen consumption at deeper layers (Karstensen *et al.,* 2015; Ficher *et al.,* 2016; Hauss *et al.,* 2016).
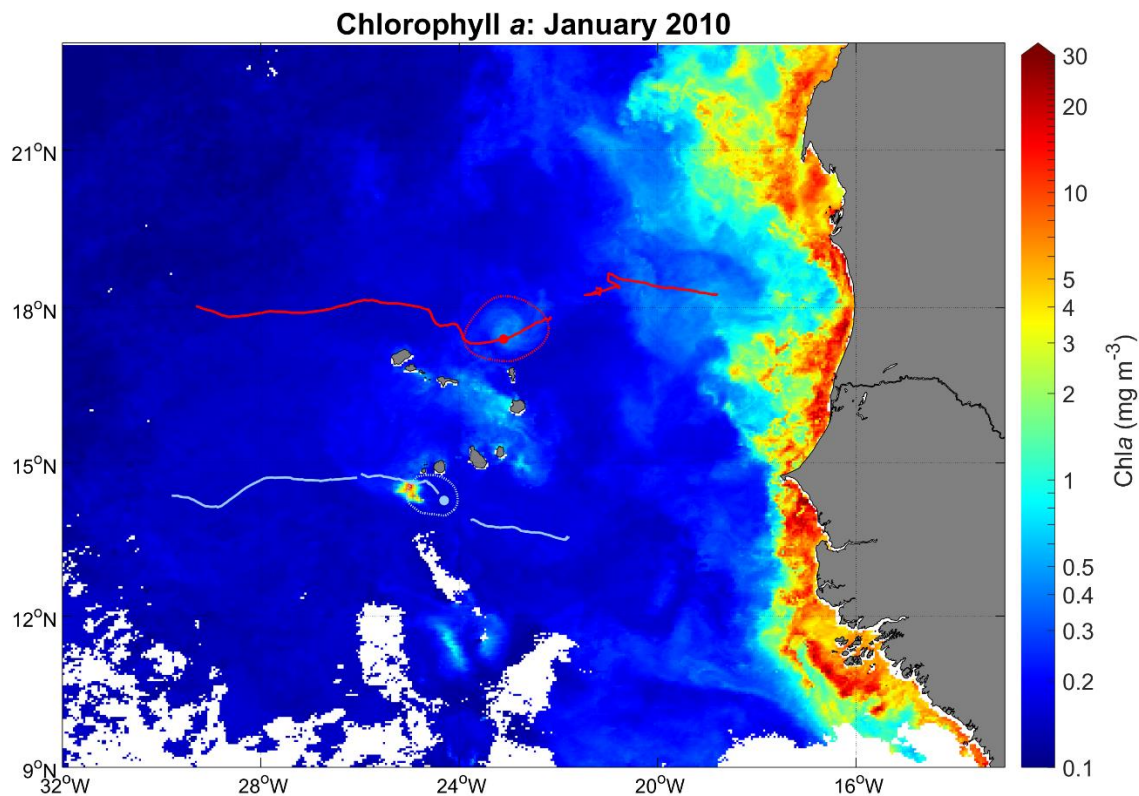
Figure 5.3 – Surface Chl*a* concentration in January, along with the respective anticyclonic (red) and cyclonic (light blue) trajectories. Doted area represents eddies perimeter.

Considering the nature of the previous anticyclonic far-field eddies, it is expected that the enhanced Chl*a* concentrations were most likely advected from the highly productive coastal area, since such features are not able to self-inject deep nutrient-rich water to the surface. On the contrary, the observed decrease in Chl*a* concentration is likely related with the deepening of the mixed layer by the downward self-induced Ekman-pumping mechanism (e.g., Sangrà *et al.,* 2009), along with the phytoplankton's nutrient-consumption and consequent depletion, and possible grazing by zooplankters (Hernández-León, 1991). Nonetheless, it has been documented that anticyclonic eddies have the potential to retain and support planktonic communities over many generations, being thus able to enhance larval survival for many invertebrate and fish species (Condie and Condie, 2016). Such finding implies that far-field eddies approaching the Cape Verde Archipelago might be a great medium for biological transportation, connecting this presumably isolated group of islands to the western African coast.

A very interesting case is the small patch of high Chl*a* values observed in February 2014 (circle in red, Figure 4.26). Although no eddy could be associated with this feature, it is reasonable to assume that such occurrence might be associated with a localised vertical advection of nutrients induced by a cyclonic eddy (Gaube *et al.,* 2013), since this region is remote and considered oligotrophic (Alpers *et al.,* 2013; Löscher et al., 2015, Fiedler *et al.,* 2016). Nevertheless, the lack of evidences hinders the association of such phenomenon to an island-induced mechanism. This kind of phenomenon has been documented in a variety of studies. In an idealized case study, Lévy *et al.* (2001) showed that sub-mesoscale physics associated with cyclonic eddies are responsible for more than 1/3 of the new production of phytoplankton in an oligotrophic regime, due to the increase of nutrient transport from the deeper layers within the surface layers. Similarly, Lin *et al.* (2010) investigated an unusual phytoplankton bloom in the south of China and suggested that the upward advection mechanisms associated with an observed cyclonic eddy were the main cause, further reinforcing current findings.

The most remarkable observation, however, is undoubtedly associated with the phytoplankton bloom southwest of Fogo Island in January 2010 (Figure 4.27 and Figure 5.3). Despite the localised and punctual nature of this phenomenon, this bloom is almost certainly associated with a far-field cyclonic eddy that approaches the windward islands from southeast (Figure 5.3). The iron-enrichment through island runoff was also considered, but since the bloom takes place in the dry season (DGA, 2003), such driving mechanism is unlikely to occur. The eddy's trajectory is interrupted as it interacts with a nearby anticyclonic eddy (supplementary material), but as soon as the latter moves away, the cyclonic eddy is reactivated and substantially intensified as it remains approximately stationary in the wake of Fogo Island, giving rise to a very pronounced Chl*a* signal. The eddy intensification may by driven by the input of energy induced by the wind in the lee of the island. Such occurrence has been documented in the lee of Hawaii, as Calil *et al.* (2008) observed the weakening and intensification of a cyclonic eddy as a causative effect induced by the wind. Furthermore, it is reasonable to expect that this mechanism can significantly stimulate phytoplankton growth at the surface, given the substantial amount of studies that demonstrated such phenomenon. In an idealized case, Hasegawa *et al.* (2009) investigated the development of phytoplankton blooms in the wake of an island and found that the upwelling of nutrients – especially nitrate – provoked by island-induced cyclonic eddies was a key factor.

Such findings have also been extensively reported in the Macaronesia islands, mainly in Madeira and Canary Islands, but never has this phenomenon been documented in the Cape Verde Archipelago. Using remote sensing tools and historical data, Caldeira *et al.* (2002) documented several episodes of sub-mesoscale cyclonic eddies generated in the western flanks of Madeira Island, accompanied by enhanced levels of Chl*a* at the centre. Further studies conducted in the same region were able to replicate similar observations (Caldeira and Sangrà, 2012, Caldeira *et al.,* 2014), further reinforcing the idea that this is a recurrent phenomenon. In Canary Islands, Hernandez-Leon, (1991) first documented the accumulation of mesozooplankton in the wake of Gran Canaria Island as a causative mechanism of the IME, but only until later could the enhanced Chl*a* surface concentrations – found in the wake of the islands – be associated with nutrient-enrichment driven by island-induced cyclonic eddies (Aristegui *et al.*, 1997, Basterretxea *et al.,* 2002). In the Azores, however, Caldeira and Jesus (2017) suggested that the ability of the islands to retain the incoming properties from the impinging flow was the main cause for the observed nutrient and/or biological local enrichment, being thus the remote enrichment though far-field features the principal driving mechanism for biological productivity in the archipelago.

Considering the substantial amount of evidences presented here, it is therefore proposed that the exposure of the Cape Verde Archipelago to far-field eddies and consequent remote-enrichment, combined with the ability to self-generate eddies and consequently enhance local biological productivity, are the main factors driving the local primary production. Nevertheless, more detailed investigation must be conducted in order to better comprehend and quantify the relation between the near and the far-field affecting the archipelago.

6. Conclusions

The current study focused on the regional and local characterisation of the oceanic processes which affect and are generated by the Cape Verde Archipelago, giving especial attention to the highly complex far-field and near-field mesoscale eddies, respectively. Although many studies have investigated the mechanisms and implications associated with eddy generation in the lee of islands, very few have considered the implications of far-field features in such near-field processes. In that sense, this study distinguishes from past studies in a very important way. As such, direct comparisons with other observations were always regarded with extreme caution.

In accordance with existing knowledge, current results have consistently demonstrated that the archipelago sits in a rather complex oceanic region, highly constrained by the atmospheric dynamics induced by the seasonal behaviour of the ITCZ. Such patterns regulate several large-scale processes, as it is the case of the oceanic surface currents and the upwelling system off the western African coast. Naturally, similar patterns are reflected at a local scale. In fact, it was observed that the wind punctual and seasonal behaviour can induce significant disturbances in the lee of the islands, followed by localised oceanic responses in the form of eddies. Several very pronounced medium and long-lived eddy hotspots were detected in the lee of the major islands of the Cape Verde Archipelago. Nevertheless, it was demonstrated that the archipelago is exposed to a remarkable number of far-field eddies, which interact with the islands and consequent island-induced processes. These far-field eddies are mostly generated in the western African coast in summer and autumn and are likely associated with the intensification of the MC. As they propagate westward, they intersect the archipelago between winter and spring, which also coincides with the periods of highest wind intensity and near-field eddy generation. This kind of interaction brings considerable implications not only for the near-field eddies, but also to the propagation and evolution of the far-field eddies. In that sense, it was observed that the far-field eddy-island interaction resulted in four different outcomes. The most recurrent scenario was eddy transformation, which made the eddy tracking algorithm to falsely identify transformed eddies as newly-generated near-field eddies. The second most often observed scenario was associated with eddy termination. Subsequently, eddy splitting was the third most observed scenario, which resulted in the termination of the impinging eddy and in the generation of several other near-field eddies. Finally, it was also observed that topographic effects induced by the islands can divert eddies and consequently change their propagation characteristics.

Considering the substantial amount of evidences that support the systematic occurrence of far-field eddy-island interactions, one may conclude that many near-field eddies are a direct product or by-product of such interaction. For this reason, it is very difficult to determine the nature of the eddies being generated in the archipelago, i.e. from island-induced mechanisms, far-field eddy-island interaction or even far-field – near-field eddy interaction. As such, it is demonstrated that the combination of near and far-field processes are the main causes in the generation of mesoscale eddies in the archipelago, making Cape Verde a perfect location for the study of such interaction.

Assuming that most medium and long-lived eddies in the region are very likely to be nonlinear (Chelton *et al.,* 2011; Schütte *et al.,* 2016a), it is suggested that the interactions between incoming far-field eddies and the archipelago can also have important implications in the local biological realm. In fact, several far-field eddies (October 2009 – January 2010 and October 2013 – December 2013) have been observed to transport Chl*a*-rich water in the direction of Cape Verde, enhancing Chl*a* concentrations in its vicinity. Nevertheless, island-induced processes can also favour local biological productivity, as it was the case of a remarkable Chl*a* signal (January 2010) strongly associated with the self-induced nutrient injection provoked by a cyclonic eddy. Curiously, this eddy was generated away from the islands, but further observations suggest that the latter was intensified by island-induced mechanisms (probably wind-shear effects) as it approached Fogo Island from the southwest, giving rise to a sudden phytoplankton bloom. This is another perfect example of the interaction between the far and the near-field, further reinforcing the idea that both fields are intertwined in such a way that hinders the distinction and quantification of individual mechanisms. It also challenges the idea that the IME is a phenomenon exclusively induced by an island (or group of islands), being thus proposed that IME can in fact be developed and sustained by the combination and interaction of local and remote processes.

One last note is regarded towards the efficiency of the eddy detection and tracking algorithm being used (Faghmous *et al.,* 2015a). It was possible to determine that a considerable number of eddy trajectories were prematurely interrupted and restarted as false newly-generated eddies (suplementary material). Such occurrence poses significant limitations and implications for the current study, in the sense that the estimated lifetime and propagation extension of some eddies may be inaccurate, which in turn can compromise the determination and characterisation of certain eddy hotspots – mainly in the western African coastal area –, as well as the number of far-field eddies intersecting CV. Taking into account past and recent literature regarding mesoscale

variability in the western African coast, it is expected that a larger number of far-field eddies – mainly originating near the Cape Vert and Cape Blanc headlands – would intersect the archipelago, but only a few cases are detected. Because of the premature termination of eddies, many of these trajectories do not reach the CV area, though their SLA signal is still observed to go beyond the eastern CV area delimitation (supplementary material), often being designated as (false) newly-generated near-field eddies as they are reactivated inside CV. Therefore, it is very likely that the number of far-field eddies interacting with the archipelago is underestimated, while the number of near-field eddies is conversely overestimated. Furthermore, the real implications of the near-field eddies at a regional scale are very likely to be underestimated. This is supported by the fact that very few near-field eddy trajectories are observed to reach longitudes farther than 35ºW, though in the sequential representations of the SLA field and eddies trajectories (supplementary material), many prematurely terminated near-field eddies often do. Such results demonstrate that, despite the considerable advances in eddy identification and tracking procedures, it is still necessary to improve current methods in order to better comprehend the physical mechanisms and real implications that such features represent to regional and local oceanography.

Summarizing the final conclusions of the study, the two initially proposed hypotheses are assessed. Can far-field features have considerable implications on oceanic islands and associated physical/biological processes, that have been neglected to present date? The answer is yes. Current results show that, despite being at ~ 600 km distance from the nearest coastal area, the interaction of far-field eddies with Cape Verde Archipelago is a recurrent phenomenon, which often hinders the distinction between local and remote-induced processes. Hence, to what extend can islands impact such far-field features? The impacts are quite remarkable. Results show that far-field eddies are always transformed when interacting with the archipelago, giving origin to new eddies through splitting, deflecting their trajectories or even terminating their existence.

Notwithstanding, new hypotheses emerged along the study: can the archipelago induce significant regional implications in the ocean, such as a long-lived eddy corridor or a zonal basin-wide countercurrent? Although the strong likelihood, further investigation must be conducted to fully elucidate such possibilities. Thus, this is proposed to be the starting point for futures studies.

References

Adduce, C. and Cenedese, C. (2004). An experimental study of a mesoscale vortex colliding with topography of varying geometry in a rotating fluid. *Journal of Marine Research*, *66*(December), 413–440.

Alpers, W., Dagorne, D., Brandt, P. (2014). Satellite observations of oceanic eddies around Africa. In *Remote Sensing of the African Seas* (pp. 205-229). Springer Netherlands.

Andrade, I., Sangrà, P., Hormazabal, S., Correa-Ramirez, M. (2014). Island mass effect in the Juan Fernández Archipelago (33ºS), Southeastern Pacific. *Deep-Sea Research Part I: Oceanographic Research Papers*, *84*, 86–99.

Andres, M. and Cenedese, C. (2013). Laboratory experiments and observations of cyclonic and anticyclonic eddies impinging on an island. *Journal of Geophysical Research: Oceans*, *118*(2), 762–773. https://doi.org/10.1002/jgrc.20081

Arístegui, J., Sangrá, P., Hernández-León, S., Cantón, M., Hernández-Guerra, A., Kerling, J. L. (1994). Island-induced eddies in the Canary Islands. *Deep-Sea Research Part I*, *41*(10), 1509–1525.

Arístegui, J., Tett, P., Hernández-Guerra, A., Basterretxea, G., Montero, M. F., Wild, K., … Barton, E. D. (1997). The influence of island-generated eddies on chlorophyll distribution: A study of mesoscale variation around Gran Canaria. *Deep-Sea Research Part I: Oceanographic Research Papers*, *44*(1), 71–96.

Arnault, S. (1987). Tropical Atlantic geostrophic currents and ship drifts. *Journal of Geophysical Research: Oceans, 92*(C5), 5076-5088.

AVISO (2015). SSALTO/DUACS User Handbook: (M)SLA and (M)ADT Near-Real Time and Delayed Time Products, CLS-DOS-NT-06-034, Issue 4.4, 1 pp. Retrieved from https://www.aviso.altimetry.fr/fileadmin/documents/data/tools/hdbk_duacs.pdf.

Barkley, R. A. (1972). Johnston Atoll's Wake'. *Journal of Marine Research*, *30*(2), 201–216.

Barton, E. D. (1987). Meanders, eddies and intrusions in the thermohaline front off Northwest Africa. *Oceanologica acta. Paris*, *10*(3), 267–283.

Barton, E. D. (2001). Island wakes. In *Encyclopedia of ocean sciences*. Edited by J. Steele, K. Turekian, and S. Thorpe. Academic Press, New York, Vol. 3, 1397–1403.

Barton, E. D., Aristegui, J., Tett, P., Canton, M., García-Braun, J., Hernández-León, S., … Wild, K. (1998). The transition zone of the Canary Current upwelling region. *Progress in Oceanography*, *41*(4), 455–504.

Barton, E. D., Arístegui, J., Tett, P., Navarro-Pérez, E. (2004). Variability in the Canary Islands area of filament-eddy exchanges. *Progress in Oceanography*, *62*(2–4), 71–94.

Barton, E. D., Basterretx, G., Flament, P., Mitchelson-jacob, E. G., Jone, B., Arístegui, J., Herrera, F. (2000). Lee region of Gran Canaria. *Journal of Geophysical Research*, *105*, 173–193.

Barton, E. D., Flament, P., Dodds, H., Mitchelson-Jacob, E. G. (2001). Mesoscale structure viewed by SAR and AVHRR near the Canary Islands. *Scientia Marina*, *65*, 167–175.

Bakun, A. (1973). Coastal Upwelling Indices, West Coast of North America, 1946–71, Tech. Rep. NMFS SSRF-671, Seattle, WA: National Oceanic and Atmospheric Administration, 103.

Batchelor, G. K. (1967). *An introduction to fluid dynamics*. Cambridge, UK: Cambridge University Press, pp 515.

Basterretxea, G., Barton, E. D., Tett, P., Sangrá, P., Navarro-Perez, E., Arístegui, J. (2002). Eddy and deep chlorophyl maximum response to wind-shear in the lee of Gran Canaria. *Deep-Sea Research Part I: Oceanographic Research Papers*, *49*(6), 1087–1101.

Bell, P. R. F. (1992). Eutrophication and coral reefs-some examples in the Great Barrier Reef lagoon. *Water Research*, *26*(5), 553–568.

Caldeira, R. M. A. and Marchesiello, P. (2002). Ocean response to wind sheltering in the Southern California Bight. *Geophysical Research Letters*, *29*(13), 1–4.

Caldeira, R. M. A., Groom, S., Miller, P., Pilgrim, D., Nezlin, N. P. (2002). Sea-surface signatures of the island mass effect phenomena around Madeira Island, Northeast Atlantic. *Remote Sensing of Environment*, *80*(2), 336–360.

Caldeira, R. M. A., Marchesiello, P., Nezlin, N. P., DiGiacomo, P. M., McWilliams, J. C. (2005). Island wakes in the Southern California Bight. *Journal of Geophysical Research: Oceans*, *110*(11), 1–20.

Caldeira, R. M. A., Stegner, A., Couvelard, X., Araújo, I. B., Testor, P., Lorenzo, A. (2014). Evolution of an oceanic anticyclone in the lee of Madeira Island: In situ and remote sensing survey. *Journal of Geophysical Research: Oceans*, *119*(2), 1195–1216.

Caldeira, R. M. A. and Reis, J. C. (2017). The Azores Confluence Zone. *Frontiers in Marine Science*, *4*, 37.

Calil, P. H. R., Richards, K. J., Jia, Y., Bidigare, R. R. (2008). Eddy activity in the lee of the Hawaiian Islands. *Deep-Sea Research Part II: Topical Studies in Oceanography*, *55*(10–13), 1179–1194.

Cenedese, C. (2002). Laboratory experiments on mesoscale vortices colliding with a seamount. *Journal of Geophysical Research: Oceans*, *107*(C6).

Cenedese, C., Adduce, C., Fratantoni, D. M. (2005). Laboratory experiments on mesoscale vortices interacting with two islands. *Journal of Geophysical Research C: Oceans*, *110*(9), 1–15.

Chaigneau, A., Gizolme, A., Grados, C. (2008). Mesoscale eddies off Peru in altimeter records: Identification algorithms and eddy spatio-temporal patterns. *Progress in Oceanography*, *79*(2–4), 106–119.

Chaigneau, A., Eldin, G., Dewitte, B. (2009). Eddy activity in the four major upwelling systems from satellite altimetry (1992-2007). *Progress in Oceanography*, *83*(1–4), 117–123.

Chang, Y. C., Chen, G. Y., Tseng, R. S., Chu, P. C. (2012). Effect of cylindrically shaped atoll on westward-propagating anticyclonic eddy- A case study. *IEEE Geoscience and Remote Sensing Letters*, *9*(1), 43–46.

Chavanne, C., Flament, P., Lumpkin, R., Dousset, B., Bentamy, A. (2002). Scatterometer observations of wind variations induced by oceanic islands: Implications for winddriven ocean circulation. *Canadian Journal of Remote Sensing*, *28*(3), 466–474.

Chassignet, E. P. and Cushman-Roisin, B. (1991). On the Influence of a Lower Layer on the Propagation of Nonlinear Oceanic Eddies. *Journal of Physical Oceanography*, , 21(7), 939-957.

Chelton, D. B., Schlax, M. G., Freilich, M. H., Milliff, R. F. (2004). Satellite Measurements Reveal Persistent Small-Scale Features in Ocean Winds. *Science*, *303*, 978–983.

Chelton, D. B., Schlax, M. G., Samelson, R. M. (2011). Global observations of nonlinear mesoscale eddies. *Progress in Oceanography*, *91*(2), 167–216.

Chelton, D., and Schlax, M. (2017). Mesoscale Eddies in Altimeter Observations of SSH. Retrieved from http://wombat.coas.oregonstate.edu/eddies/.

Cheng, Y. H., Ho, C. R., Zheng, Q., Kuo, N. J. (2014). Statistical characteristics of mesoscale eddies in the North Pacific derived from satellite altimetry. *Remote Sensing*, *6*(6), 5164-5183.

Chérubin, L. M. and Garavelli, L. (2016). Eastern caribbean circulation and island mass effect on St. Croix, US Virgin Islands: A mechanism for relatively consistent recruitment patterns. *PLoS ONE*, *11*(3), 1–28.

Chopra, K. P. and Hubert, L. F. (1964). Karman vortex-streets in Earth's atmosphere. Nature, 203(4952), 1341-1343.

Condie, S. and Condie, R. (2016). Retention of plankton within ocean eddies. *Global Ecology and Biogeography*, *25*(10), 1264–1277.

Coutis, P. F., and Middleton, J. H. (2002). The physical and biological impact of a small island wake in the deep ocean. *Deep-Sea Research Part I-Oceanographic Research Papers. 49*, 1341–1361

Couvelard, X., Caldeira, R. M. A., Araújo, I. B., Tomé, R. (2012). Wind mediated vorticity-generation and eddy-confinement, leeward of the Madeira Island: 2008 numerical case study. *Dynamics of Atmospheres and Oceans*, *58*, 128–149.

Cushman-Roisin, B., Tang, B., Chassignet, E. P. (1990). Westward motion of mesoscale eddies. *Journal of Physical Oceanography*, 20(5), 758-768.

Dandonneau, Y. and Charpy, L. (1985). An empirical approach to the Island Mass Effect in the south tropical Pacific based on sea surface chlorophyll concentrations. *Deep Sea Research*, *32*, 707–721.

Darwin, C. R. (1842). *The Structure and Distribution of Coral Reefs. Being the first part of the geology of the voyage of the Beagle, under the command of Capt. Fitzroy, R.N. during the years 1832 to 1836*. London: Smith Elder and Co. pp. 61–71.

Demarcq, H. and Somoue, L. (2015). Phytoplankton and primary productivity off Northwest Africa. In: *Oceanographic and biological features in the Canary Current Large Marine Ecosystem*. Valdés, L. and Déniz-González, I. (eds). IOC-UNESCO, Paris. IOC Technical Series, No. 115, pp. 161-174.

DGA - Direção Geral do Ambiente (2004). *Livro branco sobre o Estado do Ambiente em Cabo Verde*. Ministério do Ambiente Agricultura e Pescas, República de Cabo Verde. Available on-line at http://www.sia.cv/index.php/documentacao-mainmenu/ category/3-relatorios-e-estudos?download=13:1ivro-branco

Dong, C. and McWilliams, J. C. (2007). A numerical study of island wakes in the Southern California Bight. *Continental Shelf Research*, *27*(9), 1233–1248.

Dohan, K., and Maximenko, N. (2010). Monitoring ocean currents with satellite sensors. Oceanography 23(4):94–103.

Doty, M. S., and Oguri, M. (1956). The Island Mass Effect. *J. Conseil Perm. Int. Ex. Mer.*, *22*(1), 33–37

EC – European Comission (2017, 26th September). The Macaronesian Region. Retrieved from http://ec.europa.eu/environment/nature/natura2000/biogeog_regions/macaronesian/index_en.htm.

Emery, W. J. and Meincke, J. (1986). Global water masses: summary and review. *Oceanologica Acta*, *9*(4), 383–391.

Elken, J. (2016). Currents, in *Encyclopedia of Marine Geosciences*, Springer Netherlands.

Elliott J, Patterson M, Gleiber M. (2012). Detecting Island Mass Effect through remote sensing. *Proceedings of the 12th International Coral Reef Symposium*, 9-13th July 2012, Cairns, Queensland, Australia.

Ekman, V. W. (1905). On the influence of the earth's rotation on ocean-currents. Ark. Mat. Astron. Fys., 2 (11), 1-53.

ESA – European Space Agency (2015). GlobCurrent Product Data Handbook: The Combined Geostrophy+Ekman Currents version 2.0. Retrieved from ftp://ftp.ifremer.fr/ifremer/cersat/projects/globcurrent/documents/handbooks/GlobCurrent_D-280_Product_Handbook_L4_combined_v2-signed.pdf

ESR - Earth & Space Research (2017a, June 16th). OSCAR. Retrieved from http://www.esr.org/oscar_index.html.

ESR (2017b, June 16th). Direct Comparisons of Oscar To In Situ Data: Global Dataset. Retrieved from http://www.esr.org/~bonjean/oscar/global_validation/index.html.

EUMETSAT - European Organisation for the Exploitation of Meteorological Satellites (2015): ASCAT Product Guide V5, Doc. No. EUM/OPS-EPS/MAN/04/0028, Darmstadt, Germany, 164 pp. Available online at http://www.eumetsat.int.

Faghmous, J. H., Frenger, I., Yao, Y., Warmka, R., Lindell, A., Kumar, V. (2015a). A daily global mesoscale ocean eddy dataset from satellite altimetry. *Scientific Data*, *2*, 150028.

Faghmous J. H., Frenger I, Yao, Y., Warmka, R., Lindell, A., Kumar, V. (2015b). Data from: A daily global mesoscale ocean eddy dataset from satellite altimetry. Dryad Digital Repository. http://dx.doi.org/10.5061/dryad.gp40h

Faye, S., Lazar, A., Sow, B. A., Gaye, A. T. (2015). A model study of the seasonality of sea surface temperature and circulation in the Atlantic North-eastern Tropical Upwelling System. *Frontiers in Physics*, *3*(September), 1–20.

Fernandes, M. J., Lázaro, C., Santos, A. M. P., Oliveira, P. (2005). Oceanographic characterisation of the Cabo Verde region using multisensor data. *Proceedings of the ENVISAT and ERS Symposium, Salzburg, 6–10 September* 2004.

Fernandes, M. J., Marçal, A. R. S., Azevedo, J. C., Santos, A. M. P., Peliz, A. (2000). Fisheries monitoring in the CABO Verde region using ERS data. *Proceedings of the ERS-ENVISAT Symposium, Looking down to Earth in the New Millenium. ESA SP*, (461), 1896–1906.

Fore, A. G., Stiles, B. W., Chau, A. H., Williams, B. A., Dunbar, R. S., Rodríguez, E. (2014). Point-wise wind retrieval and ambiguity removal improvements for the QuikSCAT climatological data set. *IEEE Transactions on Geoscience and Remote Sensing*, *52*(1), 51–59.

Fiedler, B., Grundle, D. S., Schütte, F., Karstensen, J., Löscher, C. R., Hauss, H., … Körtzinger, A. (2016). Oxygen utilization and downward carbon flux in an oxygen-depleted eddy in the eastern tropical North Atlantic. *Biogeosciences*, *13*(19), 5633–5647.

Fischer, G., Reuter, C., Karakas, G., Nowald, N., Wefer, G. (2009). Offshore advection of particles within the Cape Blanc filament, Mauritania: Results from observational and modelling studies. *Progress in Oceanography*, *83*(1–4), 322–330.

Fischer, G., Karstensen, J., Romero, O., Donner, B., Hefter, J., Mollenhauer, G., … Körtzinger, A. (2016). Bathypelagic particle flux signatures from a suboxic eddy in the oligotrophic tropical North Atlantic: Production, sedimentation and preservation. *Biogeosciences*, *13*(11), 3203–3223.

Fu, L. L., and Holt, B. (1983). Some examples of detection of mesoscale eddies by the SEASAT Synthetic-Aperture Radar. *Journal of Geophysical Research.*, *88*(C3), 1844–1852.

Frantantoni, D.M. (2001). North Atlantic surface circulation during the 1990s observed with satellite-tracked drifters. *Journal of Geophysical Research* 106, 22067–22093.

Gabric, A. J., García, L., Van Camp, L., Nykjaer, L., Eifler, W., Schrimpf, W. (1993). Offshore export of shelf production in the Cap Blanc giant filament as derived from CZCS imagery. *Journal of Geophysical Research*, *98*(C3), 4697–4712.

Gaube, P., Chelton, D. B., Strutton, P. G., Behrenfeld, M. J. (2013). Satellite observations of chlorophyll, phytoplankton biomass, and Ekman pumping in nonlinear mesoscale eddies. *Journal of Geophysical Research: Oceans*, *118*(12), 6349–6370.

García-Weil, L., Ramos, A. G., Coca, J., Redondo, A. (2014). Mesoscale Dynamics in the Canary Islands Area as Observed Through Complementary Remote Sensing Techniques. In *Remote Sensing of the African Seas* (pp. 97-118). Springer Netherlands.

Gelado-Caballero, M. D. (2015). Saharan dust inputs to the Northeast Atlantic. In: *Oceanographic and biological features in the Canary Current Large Marine Ecosystem*. Valdés, L. and Déniz-González, I. (eds). IOC-UNESCO, Paris. IOC Technical Series, No. 115, pp. 53-61.

GHRSST - Global High Resolution Sea Surface Temperature (2017, January 17th). CEOS SST-VC. Retrieved from https://www.ghrsst.org/about-ghrsst/ceos-sst-vc/.

Gomes, N., Neves, R., Kenov, I. A., Campuzano, F. J., Pinto, L. (2015). Tide and Tidal Currents in the Cape Verde Archipelago. *Revista de Gestão Costeira Integrada*, *15*(3), 395–408.

Gove, J. M., McManus, M. A., Neuheimer, A. B., Polovina, J. J., Drazen, J. C., Smith, C. R., … Williams, G. J. (2016). Ocean Oases: near-island biological hotspots in barren ocean basins. *In Nature communications, 7, 10581*.

Gill, A. E. (1982). Atmosphere - Ocean dynamics, Vol. 30. New York, NY: Academic Press.

Hafner, J. and Xie, S. P. (2003). Far-Field Simulation of the Hawaiian Wake: Sea Surface Temperature and Orographic Effects. *Journal of the Atmospheric Sciences*, *60*(24), 3021–3032.

Hagen, E. (2001). Northwest African upwelling scenario. *Oceanologica Acta*, *24*(December 1999), 113–128.

Hamner, W. M., and Hauri, I. R. (1981). Effects of island mass: Water flow and plankton pattern around a reef in the Great Barrier Reef lagoon, Australia. *Limnology and Oceanography*, *26*(6), 1084–1102.

Hasegawa, D., Lewis, M. R., Gangopadhyay, A. (2009). How islands cause phytoplankton to bloom in their wakes. *Geophysical Research Letters*, *36*(20), 2–5. https://doi.org/10.1029/2009GL039743

Hasegawa, D., Yamazaki, H., Lueck, R. G., Seuront, L. (2004). How islands stir and fertilize the upper ocean. *Geophysical Research Letters*, *31*(16), 2–5.

Hausman, J., Bonjean, F., Dohan, K. (2009). Ocean Surface Current Analysis (OSCAR) Third Degree Resolution User's Handbook. California Institute of Technology, CA. Retrieved from http://apdrc.soest.hawaii.edu/doc/oscarthirdguide.pdf.

Hauss, H., Christiansen, S., Schütte, F., Kiko, R., Lima, M. E., Rodrigues, E., … Fiedler, B. (2016). Dead zone or oasis in the open ocean? Zooplankton distribution and migration in low-oxygen modewater eddies. *Biogeosciences*, *13*(6), 1977–1989.

Helmke, P., Romero, O., Fischer, G. (2005). Northwest African upwelling and its effect on offshore organic carbon export to the deep sea. *Global Biogeochemical Cycles*, *19*(4), 1–16.

Hernández-León, S. (1991). Accumulation of mesozooplankton in a wake area as a causative mechanism of the "island-mass effect." *Marine Biology*, *109*(1), 141–147.

Heywood, K. J., Barton, E. D., Simpson, J. H. (1990). The effects of flow disturbance by an oceanic island. *Journal of Marine Research*, *48*, 55–73.

Hoffman, R. N., and Leidner, S. M. (2005). An introduction to the near–real–time QuikSCAT data. *Weather and Forecasting*, *20*(4), 476-493.

Hogg, A. M. C., Meredith, M. P., Chambers, D. P., Abrahamsen, E. P., Hughes, C. W., Morrison, A. K. (2015). Recent trends in the Southern Ocean eddy field. *Journal of Geophysical Research: Oceans*, *120*(1), 257–267.

Holland, C. L. and Mitchum, G. T. (2001). Propagation of Big Island eddies. *Journal of Geophysical Research: Oceans*, *106*(C1), 935–944.

Hwang, D., Lee, Y. W., Kim, G. (2005). Large submarine groundwater discharge and benthic eutrophication in Bangdu Bay on volcanic Jeju Island, Korea. Limnology and Oceanography, 50(5), 1393-1403.

Jia, Y., Calil, P. H. R., Chassignet, E. P., Metzger, E. J., Potemra, J. T., Richards, K. J., Wallcraft, A. J. (2011). Generation of mesoscale eddies in the lee of the Hawaiian Islands. *Journal of Geophysical Research: Oceans*, *116*(11), 1–18.

Jiménez, B., Sangrà, P., Mason, E. (2008). A numerical study of the relative importance of wind and topographic forcing on oceanic eddy shedding by tall, deep water islands. *Ocean Modelling* (Vol. 22).

Jones, E. C. (1962). Evidence of an island effect upon the standing crop of zooplankton near the Marquesas Islands, Central Pacific. *ICES Journal of Marine Science*, *27*(3), 223-231.

Kaiser, A., Carroll, A. O., Beggs, H., & Beggs, H. (2012). GHRSST Strategy and Implementation Plan (GDIP), *1*(January), 93 pp.

Karimova, S. (2012). Spiral eddies in the Baltic, Black and Caspian seas as seen by satellite radar data. *Advances in Space Research*, *50*(8), 1107–1124.

Karstensen, J., Fiedler, B., Schütte, F., Brandt, P., Körtzinger, A., Fischer, G., ... Wallace, D. W. (2015). Open ocean dead-zone in the tropical North Atlantic Ocean. *Biogeosciences (BG)*, *12(8)*, 2597-2605.

Kostianoy, A. G. and Zatsepin, A. G. (1996). The West African coastal upwelling filaments and cross-frontal water exchange conditioned by them. *Journal of Marine Systems*, *7*(2–4), 349–359. https://doi.org/10.1016/0924-7963(95)00029-1

Lange, C. B., Romero, O. E., Wefer, G., Gabric, A. J. (1998). Offshore influence of coastal upwelling off Mauritania, NW Africa, as recorded by diatoms in sediment traps at 2195 m water depth. *Deep-Sea Research Part I: Oceanographic Research Papers*, *45*(6), 985–1013.

Large, W. G. and Pond, S. (1981). Open Ocean Momentum Flux Measurements in Moderate to Strong Winds. *Journal of Physical Oceanography*, *11*(3), 324-336.

Lathuilière, C., Echevin, V., Lévy, M. (2008). Seasonal and intraseasonal surface chlorophyll-a variability along the northwest African coast. *Journal of Geophysical Research: Oceans*, *113*(5), 2000–2004.

Lázaro, C., Fernandes, M. J., Santos, A. M. P., Oliveira, P. (2005). Seasonal and interannual variability of surface circulation in the Cabo Verde region from 8 years of merged T/P and ERS-2 altimeter data. *Remote Sensing of Environment*, *98*(1), 45–62.

Lévy, M., Klein, P., Treguier, A.-M. (2001). Impact of sub-mesoscale physics on production and subduction of phytoplankton in an oligotrophic regime. *Journal of Marine Research*, *59*(4), 535–565.

Lozier, M. S., Owens, W. B., Curry, R. G. (1995). The climatology of the North Atlantic. *Progress in Oceanography*, *36*(1), 1–44.

Löscher, C. R., Fischer, M. A., Neulinger, S. C., Fiedler, B., Philippi, M., Schütte, F., … Schmitz, R. A. (2015). Hidden biosphere in an oxygen-deficient Atlantic open-ocean eddy: Future implications of ocean deoxygenation on primary production in the eastern tropical North Atlantic. *Biogeosciences*, *12*(24), 7467–7482.

Lin, I. I., Lien, C. C., Wu, C. R., Wong, G. T. F., Huang, C. W., Chiang, T. L. (2010). Enhanced primary production in the oligotrophic South China Sea by eddy injection in spring. *Geophysical Research Letters*, *37*(16), 1–5.

Lumpkin, C. F., (1998). Eddies and currents of the Hawaiian Islands. Ph.D. dissertation, University of Hawaii, Manoa.

Lumpkin, R. and Garzoli, S. L. (2005). Near-surface circulation in the Tropical Atlantic Ocean. *Deep-Sea Research Part I: Oceanographic Research Papers*, *52*(3), 495–518.

Lumpkin, R. and Pazos, M. (2007). Measuring surface currents with Surface Velocity Program drifters: the instruments, its data and some recent results. *Lagrangian Analysis and Prediction of Coastal and Ocean Dynamics*, 1–56.

Lungu, T., Ed., (2001). QuikSCAT science data product user's manual: Overview & geophysical data products. JPL D-18053, Version 2.2, Jet Propulsion Laboratory, Pasadena, CA, pp. 95. Retrieved from ftp://podaac.jpl.nasa.gov/allData/quikscat/L2A/v2/docs/QSUG_v3.pdf.

Marcello, J., Hernández-Guerra, A., Eugenio, F., Fonte, A. (2011). Seasonal and temporal study of the northwest African upwelling system. *International Journal of Remote Sensing*, *32*(7), 1843–1859.

Martinez, E. and Maamaatuaiahutapu, K. (2004). Island mass effect in the Marquesas Islands: Time variation. *Geophysical Research Letters*, *31*(18), 1–4.

Martínez-Marrero, A., Rodríguez-Santana, A., Hernández-Guerra, A., Fraile-Nuez, E., López-Laatzen, F., Vélez-Belchí, P., Parrilla, G. (2008). Distribution of water masses and diapycnal mixing in the Cape Verde Frontal Zone. *Geophysical Research Letters*, *35*(7), 1–5.

Mertz, F., Rosmorduc, V., Maheu, C., Faugère,. Y. (2017). Product user manual For Sea Level SLA products version 3.0, CMEMS-SL-PUM-008-032-051, Issue 1.1, 8 pp. Retrieved from http://cmems-resources.cls.fr/documents/PUM/CMEMS-SL-PUM-008-032-051.pdf.

Meunier, T., Barton, E. D., Barreiro, B., Torres, R. (2012). Upwelling filaments off cap blanc: Interaction of the NW African upwelling current and the Cape Verde frontal zone eddy field? *Journal of Geophysical Research: Oceans*, *117*(8), 1–18.

Mittelstaedt, E. (1983). The upwelling area off Northwest Africa - A description of phenomena related to coastal upwelling. *Progress in Oceanography*, *12*(3), 307–331.

Mittelstaedt, E. (1991). The ocean boundary along the northwest African coast: Circulation and oceanographic properties at the sea surface. *Progress in Oceanography*, *26*(4), 307– 355.

Moosdorf, N., Stieglitz, T., Waska, H., Dürr, H. H., Hartmann, J. (2015). Submarine groundwater discharge from tropical islands: a review. Grundwasser, 20(1), 53-67.

Molinari, R. L., Garzoli, S. L., Katz, E. J., Harrison, D. E., Richardson, P. L. (1986). A Synthesis of the First GARP Global Experiment (FGGE) in the Equatorial Atlantic Ocean. *Progress in Oceanography*, *16*, 91–112.

Moroni, D., Stiles, B., Fore, A. (2013). QuikSCAT Level 2B Version 3: Guide Document. JPL 13-1408, Version 1.0, Jet Propulsion Laboratory, Pasadena, CA, 16 pp. Retrieved from ftp://podaac.jpl.nasa.gov/allData/quikscat/L2B12/docs/qscat_l2b_v3_ug_v1_0.pdf.

Morrow, R., Birol, F., Griffin, D., and Sudre, J. (2004). Divergent pathways of cylonic and anti-cyclonic ocean eddies. *Geophysical Research Letters*, *31*(24), 1–5.

Movable Type Scripts (31st May, 2017). Calculate distance, bearing and more between Latitude/Longitude points. Retrieved from http://www.movable-type.co.uk/scripts/latlong.html.

Munk, W., Armi, L., Fischer, K., & Zachariasen, F. (2000). Spirals on the sea. *Proceedings of the Royal Society A: Mathematical, Physical and Engineering Sciences*, *456*(1997), 1217–1280.

NCAS - National Center for Atmospheric Science (2017, July 10th). CVAO-Observatório Atmosferico de Cabo Verde Humberto Duarte Fonseca. Retrieved from https://www.ncas.ac.uk/index.php/en/cvao-home.

Nieto, K., Demarcq, H., McClatchie, S. (2012). Mesoscale frontal structures in the Canary Upwelling System: New front and filament detection algorithms applied to spatial and temporal patterns. *Remote Sensing of Environment*, *123*, 339–346.

Nykjær, L. and Van Camp, L. (1994). Seasonal and interannual variability of coastal upwelling along northwest Africa and Portugal from 1981 to 1991. *Journal of Geophysical Research*, *99*(C7), 14197.

Ohde, T. and Siegel, H. (2010). Biological response to coastal upwelling and dust deposition in the area off Northwest Africa. *Continental Shelf Research*, *30*(9), 1108–1119.

Okubo, A. (1970). Horizontal dispersion of floatable particles in the vicnity of velocity singularies such as convergences. *Deep-Sea Res.*, *17*(445–454), 445–454.

Onken, R., and Klein, B. (1991). A Model of Baroclinic Instability and Waves between the Ventilated Gyre and the Shadow Zone of the North Atlantic Ocean. *Journal of Physical Oceanography*.

Ould-dedah, S., Wiseman, W. J., Shaw, R. F., Recherches, N. De. (1999). Spatial and temporal trends of sea surface temperature in the northwest African region. *Oceanologica Acta*, *22*(3), 265–279.

OSI SAF (2016). ASCAT Wind Product User Manual version 1.14, SAF/OSI/CDOP/KNMI/TEC/MA/126. Retrieved from http://projects.knmi.nl/scatterometer/publications/pdf/ASCAT_Product_Manual.pdf.

Palacios, D. M. (2002). Factors influencing the island-mass effect of the Galápagos archipelago. *Geophysical Research Letters*, *29*(2), 1–4.

Palacios, D. M. (2004). Seasonal patterns of sea-surface temperature and ocean color around the Galápagos: Regional and local influences. *Deep-Sea Research Part II: Topical Studies in Oceanography*, *51*(1–3), 43–57.

Palacios, D. M., Bograd, S. J., Foley, D. G., Schwing, F. B. (2006). Oceanographic characteristics of biological hot spots in the North Pacific: A remote sensing perspective. *Deep-Sea Research Part II: Topical Studies in Oceanography*, *53*(3–4), 250–269.

Pascual, A., Faugère, Y., Larnicol, G., Le Traon, P. Y. (2006). Improved description of the ocean mesoscale variability by combining four satellite altimeters. *Geophysical Research Letters*, *33*(2), 3–7.

Pastor, M. V., Pelegrí, J. L., Hernández-Guerra, A., Font, J., Salat, J., Emelianov, M. (2008). Water and nutrient fluxes off Northwest Africa. *Continental Shelf Research*, *28*(7), 915–936.

Patzert W. C. (1969) Eddies in Hawaiian Waters, Report NO. HIG-698. Institute of Geophysics, University of Hawaii, 51 pp.

Pelegrí, J. L., Marrero-Díaz, A., Ratsimandresy, A. W. (2006). Nutrient irrigation of the North Atlantic. *Progress in Oceanography*, *70*(2–4), 366–406.

Pelegrí, J. L. and Peña-Izquierdo, J. (2015). Inorganic nutrients and dissolved oxygen in the Canary Current Large Marine Ecosystem. In *Oceanographic and biological features in the Canary Current Large Marine Ecosystem*. Valdés, L. and Déniz-González, I. (eds). IOC-UNESCO, Paris. IOC Technical Series, No. 115, pp. 133-142.

Pérez-Rodríguez, P., Pelegrí, J. L., Marrero-Díaz, A. (2001). Dynamical characteristics of the Cape Verde frontal zone. *Scientia Marina*, 65(S1), 241–250.

Perissinotto, R., Lutjeharms, J. R. E., Van Ballegooyen, R. C. (2000). Biological-physical interactions and pelagic productivity at the Prince Edward Islands, Southern Ocean. *Journal of Marine Systems*, *24*(3–4), 327–341.

Pingree, R. D. and Maddock, L. (1980). Tidally induced residual flows around an island due to both frictional and rotational effects. *Geophysical Journal of the Royal Astronomical Society*, *63*(2), 533–546.

Philander, S. G. H., Gu, D., Halpern, D., Lambert, G., Lau, N. C., Li, T., Pacanowski, R. C. (1996). Why the ITCZ is mostly north of the equator. *Journal of Climate*, 9(12), 2958-2972.

PO.DAAC (2017, July 14th). QuikSCAT Level 2B Ocean Wind Vectors in 12.5km Slice Composites Version 3.1. Retrieved from https://podaac.jpl.nasa.gov/dataset/QSCAT_LEVEL_2B_OWV_COMP_12_LCR_3.1.

Polito, P. S. and Sato, O. T. (2015). Do eddies ride on Rossby waves? *Journal of Geophysical Research: Oceans*, *120*(8), 5417–5435.

Pond, S., and Pickard, G. L. (1983). *Introductory Dynamical Oceanography (Second Edition).* Pergamon, New York. pp. 14.

Pradhan, Y., Lavender, S. J., Hardman-Mountford, N. J., Aiken, J. (2006). Seasonal and inter-annual variability of chlorophyll-a concentration in the Mauritanian upwelling: Observation of an anomalous event during 1998-1999. *Deep-Sea Research Part II: Topical Studies in Oceanography*, *53*(14–16), 1548–1559.

Qiu, B., Koh, D. A., Lumpkin, C., Flament, P. (1997). Existence and Formation Mechanism of the North Hawaiian Ridge Current. *Journal of Physical Oceanography*, *27*(3), 431–444.

Ramalho, R. A. S. (2011). The Cabo Verde archipelago. In *Building the Cabo Verde Islands*. Berlin, Heidelberg: Springer Berlin Heidelberg, pp. 13–26.

Reverdin, G., Niiler, P. P., Valdimarsson, H. (2003). North Atlantic Ocean surface currents. *Journal of Geophysical Research: Oceans*, *108*(C1), 2–21.

Richardson, P. L. (1983). Eddy kinetic energy in the North Atlantic from surface drifters. *Journal of Geophysical Research: Oceans*, *88*(C7), 4355-4367.

Richardson, P. L. and Walsh, D. (1986). Mapping climatological seasonal variations of surface currents in the tropical Atlantic using ship drifts. *Journal of Geophysical Research: Oceans*, *91*(C9), 10537–10550.

Ricciardulli, L. (2016). ASCAT on MetOp-A Data Product Update Notes (Technical Report No. 040416). Retrieved from http://images.remss.com/papers/rsstech/2016_040416_RSS_ASCAT_V2_update.pdf.

Ricciardulli, L. and Wentz, F.J. (2016). Remote Sensing Systems ASCAT C-2015 Orbital Ocean Vector Winds, Version 02.1. Remote Sensing Systems, Santa Rosa, CA. Dataset accessed 2017-05-02 at www.remss.com/missions/ascat.

Rissik, D., Suthers, I. M., & Taggart, C. T. (1997). Enhanced zooplankton abundance in the lee of an isolated reef in the south Coral Sea: the role of flow disturbance. *Journal of Plankton Research*, *19*(9), 1347–1368.

Robinson, I. S. (2010). *Discovering the ocean from space: The unique applications of satellite oceanography*. New York: Springer.

Rodrıguez, J. M., Hernández-León, S., & Barton, E. D. (1999). Mesoscale distribution of fish larvae in relation to an upwelling filament off Northwest Africa. *Deep Sea Research Part I: Oceanographic Research Papers*, *46*(11), 1969-1984.

Romero, O. E., Fischer, G., Karstensen, J., Cermeño, P. (2016). Eddies as trigger for diatom productivity in the open-ocean Northeast Atlantic. *Progress in Oceanography*, *147*, 38–48.

RSS – Remote Sensing System (2017, July 14th). ASCAT. Retrieved from http://www.remss.com/missions/ascat.

Sander, F. and Steven, D. M. (1973). Organic productivity of inshore and offshore waters of Barbados: a study of the island mass effect. *Bulletin of Marine Science*, 23:771-792

Sangrà, P., Auladell, M., Marrero-Díaz, A., Pelegrí, J. L., Fraile-Nuez, E., Rodríguez-Santana, A., … Hernández-Guerra, A. (2007). On the nature of oceanic eddies shed by the Island of Gran Canaria. *Deep-Sea Research Part I: Oceanographic Research Papers*, *54*(5), 687–709.

Sangrà, P., Pelegrí, J. L., Hernández-Guerra, A., Arregui, I., Martín, J. M., Marrero-Díaz, A., … Rodríguez-Santana, A. (2005). Life history of an anticyclonic eddy. *Journal of Geophysical Research C: Oceans*, *110*(3), 1–19.

Sangrà, P., Pascual, A., Rodríguez-Santana, Á., Machín, F., Mason, E., McWilliams, J. C., … Auladell, M. (2009). The Canary Eddy Corridor: A major pathway for long-lived eddies in the subtropical North Atlantic. *Deep-Sea Research Part I: Oceanographic Research Papers*, *56*(12), 2100–2114.

Saraiva, A. C. (1961). "Conspectus" da entomofauna cabo-verdiana (Vol. 83). Lisboa, Junta de Investigações do Ultramar, pp 28.

Sasaki, H., Xie, S. P., Taguchi, B., Nonaka, M., Masumoto, Y. (2010). Seasonal variations of the Hawaiian Lee Countercurrent induced by the meridional migration of the trade winds. *Ocean Dynamics*, *60*(3), 705–715.

Savtchenko, A., Ouzounov, D., Ahmad, S., Acker, J., Leptoukh, G., Koziana, J., Nickless, D. (2004). Terra and Aqua MODIS products available from NASA GES DAAC. *Advances in Space Research*, *34*(4), 710–714.

Schneider, T., Bischoff, T., Haug, G. H. (2014). Migrations and dynamics of the intertropical convergence zone. *Nature*, *513*(7516), 45–53.

Schlax, M. G., and Chelton, D. B. (2016). The "Growing Method" of Eddy Identification and Tracking in Two and Three Dimensions.

Schott, F. A., Mccreary, J. P., Johnson, G. C. (2004). Shallow Overturning Circulations of the Tropical-Subtropical Oceans. *Earth's Climate*, 261–304.

Schütte, F., Brandt, P., Karstensen, J. (2016a). Occurrence and characteristics of mesoscale eddies in the tropical northeastern Atlantic Ocean. *Ocean Science*, *12*(3), 663–685.

Schütte, F., Karstensen, J., Krahmann, G., Hauss, H., Fiedler, B., Brandt, P., … Körtzinger, A. (2016b). Characterization of "dead-zone" eddies in the eastern tropical North Atlantic. *Biogeosciences*, *13*(20), 5865–5881.

SeaPAC (2016). QuikSCAT Level 2B Ocean Wind Vectors in 12.5km Slice Composites Version 3.1. Ver. 3.1. PO.DAAC, CA, USA. Dataset accessed 2017-03-02 at http://dx.doi.org/10.5067/QSX12-L2B31.

Seki, M. P., Polovina, J. J., Brainard, R. E., Bidigare, R. R., Leonard, C. L., Foley, D. G. (2001). Biological enhancement at cyclonic eddies tracked with GEOS thermal imagery in Hawaiian waters. *Geophysical Research Letters*, *28*(8), 1583–1586.

Siedler, G., Zangenberg, N., Onken, R. (1992). Seasonal changes in the tropical Atlantic circulation - observation and simulation of the Guinea Dome. *Journal of Geophysical Research-Oceans*, *97*(C1), 703–715.

Signorini, S. R., McClain, C. R., Dandonneau, Y. (1999). Mixing and phytoplankton bloom in the wake of the Marquesas Islands. *Geophysical Research Letters*, *26*(20), 3121–3124.

Simmons, H. L. and Nof, D. (2000). Islands as eddy splitters. *Journal of Marine Research*, *58*(6), 919–956. https://doi.org/10.1357/002224000763485755

Simmons, H. L. and Nof, D. (2002). The Squeezing of Eddies through Gaps. *Journal of Physical Oceanography*, *32*(1), 314–335.

Simpson, J. H. and Tett, P. B. (1986). Island stirring effects on phytoplankton growth. In *Tidal mixing and plankton dynamics* (pp. 41-76). Springer New York.

Small, R. J., Xie, S. P., O'Neill, L., Seo, H., Song, Q., Cornillon, P., ... Minobe, S. (2008). Air–sea interaction over ocean fronts and eddies. *Dynamics of Atmospheres and Oceans, 45*(3), 274-319.

Soares, E. (2015). Regional weather dynamics and forcing in tropical and subtropical Northwest Africa. In: *Oceanographic and biological features in the Canary Current Large Marine Ecosystem*. Valdés, L. and Déniz-González, I. (eds). IOC-UNESCO, Paris. IOC Technical Series, No. 115, pp. 63-72.

Smith, R. L. (1968). Upwelling, Oceanogr. Mar. Biol. Ann. Rev. 6, 11–46.

Spedding, G. R. (2014). Wake Signature Detection. *Annual Review of Fluid Mechanics*, *46*(1), 273–302.

Spencer, M. W., Wu, C., Long, D. G., Member, S. (2000). Improved Resolution Backscatter Measurements with the SeaWinds Pencil-Beam Scatterometer, *38*(1), 89–104.

Stern, M. E. (2000). Scattering of an eddy advected by a current towards a topographic obstacle. *Journal of Fluid Mechanics*, *402*, 211–223.

Stewart, R. H. (2008). *Introduction to physical oceanography*. Texas: Texas A & M University.

Stramma, L. and Schott, F. (1999). The mean flow field of the tropical Atlantic Ocean. *Deep Sea Research. II*, *46*(1–2), 279–303.

Stramma, L. and Siedler, G. (1988). Seasonal changes in the North Atlantic subtropical gyre. *Journal of Geophysical Research*, *93*(C7), 8111.

Stramma, L., Hüttl, S., Schafstall, J. (2005). Water masses and currents in the upper tropical northeast Atlantic off northwest Africa. *Journal of Geophysical Research: Oceans*, *110*(12), 1–18.

Tait, D. R., Erler, D. V., Santos, I. R., Cyronak, T. J., Morgenstern, U., Eyre, B. D. (2014). The influence of groundwater inputs and age on nutrient dynamics in a coral reef lagoon. *Marine Chemistry*, *166*, 36–47.

Talley, L. D., Pickard, G.E., Emery, W.J., Swift, J.H. (2011). *Descriptive Physical Oceanography: An Introduction (Sixth Edition)*. Elsevier, Burlingham, MA.

Tanabe, A. and Cenedese, C. (2008). Laboratory experiments on mesoscale vortices colliding with an island chain. *Journal of Geophysical Research: Oceans*, *113*(4), 1–12.

Tilstone, G. H., Angel-Benavides, I. M., Pradhan, Y., Shutler, J. D., Groom, S., & Sathyendranath, S. (2011). An assessment of chlorophyll-a algorithms available for SeaWiFS in coastal and open areas of the Bay of Bengal and Arabian Sea. *Remote Sensing of Environment*, *115*(9), 2277–2291.

Tomczak, M. (1998). *Shelf and Coastal Zone*, Lecture Notes, Version 1.0. Retrieved from http://www.mt-oceanography.info/ShelfCoast/.

Tomczak, M., and Godfrey, J. S. (1994). *Regional Oceanography: An Introduction*. Pergamon, New York.

Thyng, K.M., C.A. Greene, R.D. Hetland, H.M. Zimmerle, S.F. DiMarco (2016). True colors of oceanography: Guidelines for effective and accurate colormap selection. *Oceanography 29(3)*:9–13

Trenberth, K. E., Large, W. G., Olson, J. G. (1990). The mean annual cycle in global ocean wind stress. *Journal of Physical Oceanography*, *20*(11), 1742-1760.

Van Camp, L., Nykjaer, L., Mittelstaedt, E., Schlittenhardt, P. (1991). Upwelling and boundary circulation off Northwest Africa as depicted by infrared and visible satellite observations. *Progress in Oceanography*, *26*(4), 357–402.

Van Leeuwen, P. J. (2007). The propagation mechanism of a vortex on the β plane. *Journal of Physical Oceanography*, *37*(1997), 2316–2330.

Varela-Lopes, G. E. and Molion, L. C. B. (2014). Precipitation Patterns in Cabo Verde Islands: Santiago Island Case Study. *Atmospheric and Climate Sciences*, *4*(December), 854–865.

Wallace, A. R. (1892). *Island Life; Or the Phenomena and Causes of Insular Faunas and Floras: Including a Revision and Attempted Solution of the Problem of Geological Climates, Second Edition,* pp243-244. New York, NY: Macmillan and Company.

Waliser, D. E. and Gautier, C. (1993). A satellite-derived climatology of the ITCZ. *Journal of Climate*, 6(11), 2162-2174.

Weiss, J. (1991). The dynamics of entropy transfer in 2-dimensional hydrodynamics. *Physica D*, *48*, 273.

Williams, S., M. Petersen, P.-T. Bremer, M. Hecht, V. Pascucci, J. Ahrens, M. Hlawitschka, B. Hamann (2011). Adaptive extraction and quantification of geophysical vortices, *IEEE T. Vis. Comput. Gr.*, 17, 2088-2095.

Yang, S., Xing, J., Chen, D., Chen, S. (2016). A modelling study of eddy-splitting by an Island/Seamount. *Ocean Science Discussions*, (December), 1–25.

Yamagata, T. and Iizuka, S. (1995). Simulation of the tropical thermal domes in the Atlantic. A seasonal cycle. *Journal of Physical Oceanography*, 25(9), 2129-2140.

Yamaguchi, S. and Kawamura, H. (2009). SAR-imaged spiral eddies in Mutsu Bay and their dynamic and kinematic models. *Journal of Oceanography*, *65*(4), 525–539.

Yoshida, S., Qiu, B., Hacker, P. (2010). Wind-generated eddy characteristics in the lee of the island of Hawaii. *Journal of Geophysical Research: Oceans*, *115*(3), 1–15.

Xie, S. P., Liu, W. T., Liu, Q., Nonaka, M. (2001). Far-reaching effects of the Hawaiian Islands on the Pacific Ocean-atmosphere system. *Science (New York, N.Y.)*, *292*(5524), 2057–2060.

Zhang, D., McPhaden, M. J., Johns, W. E. (2003). Observational Evidence for Flow between the Subtropical and Tropical Atlantic: The Atlantic Subtropical Cells. *Journal of Physical Oceanography*, *33*, 1783–1797.

Zenk, W., Klein, B., Schroder, M. (1991). Cape Verde Frontal Zone. *Deep Sea Research Part A. Oceanographic Research Papers*, *38*, S505–S530.

Annexes

Annex A: Area and Maximum Altitude of the Cape Verde Islands

Annex A.1 – Area and maximum altitude of each island of the Cabo Verde islands.

Windward				Leeward					
S. Antão	S. Vicente	S. Luzia	S. Nicolau	Sal	Boa Vista	Maio	Santiago	Fogo	Brava
Area (km^2)									
779	227	35	388	216	620	269	991	476	67
Maximum Altitude (m)									
1979	750	395	1340	406	387	436	1395	2829	976

Annex B: OSCAR Validation
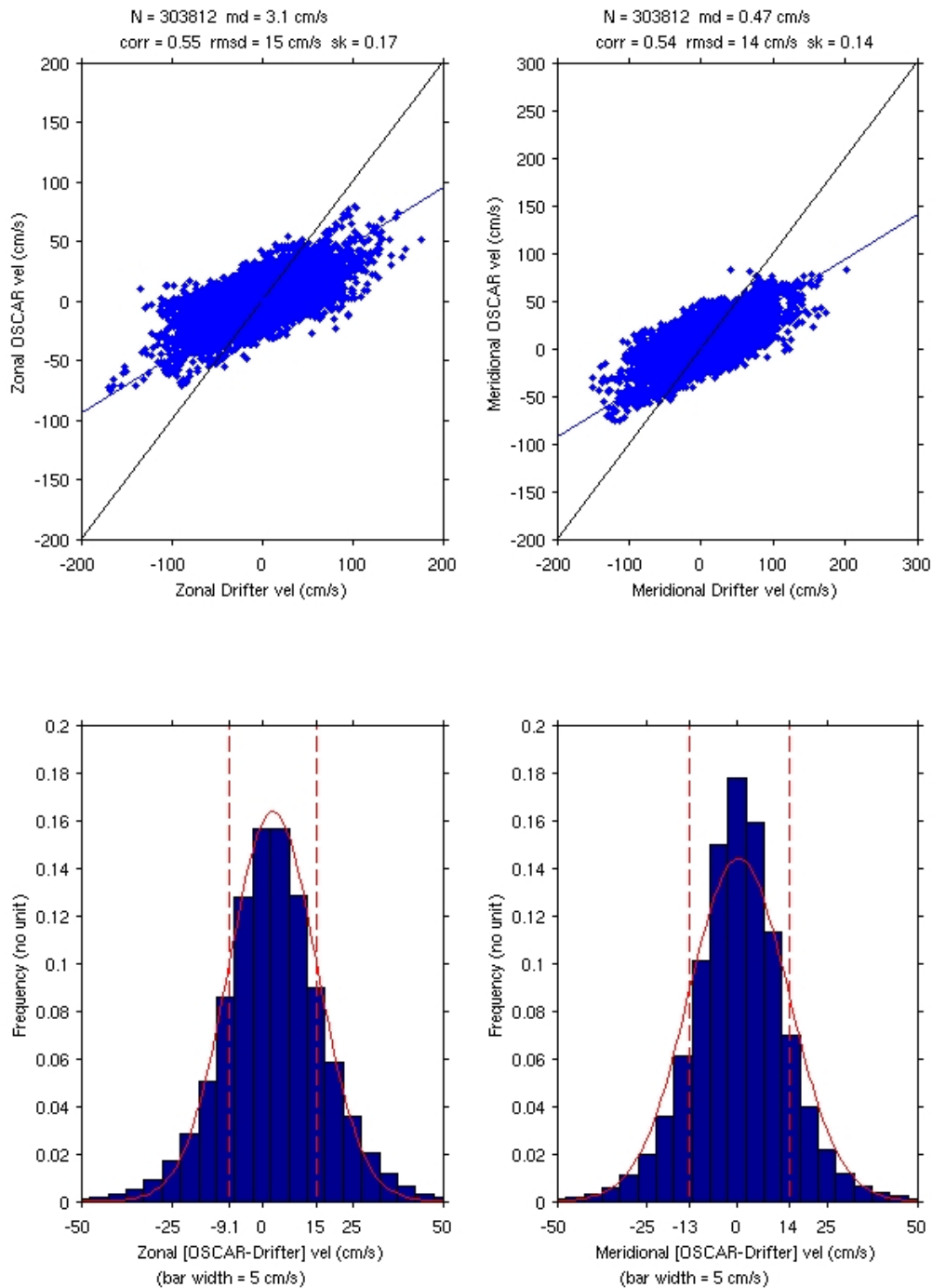
Annex B.1 – OSCAR validation plots. Upper panels represent the scatter plots of In-situ drifter data (x-axis) versus OSCAR model data (y-axis). Lower panels represent the OSCAR data distribution. Only data from 2005 to present is accounted. Source: ESR. Retrieved from http://www.esr.org/~bonjean/oscar/global_validation/index_files/AtlanticN1.htm
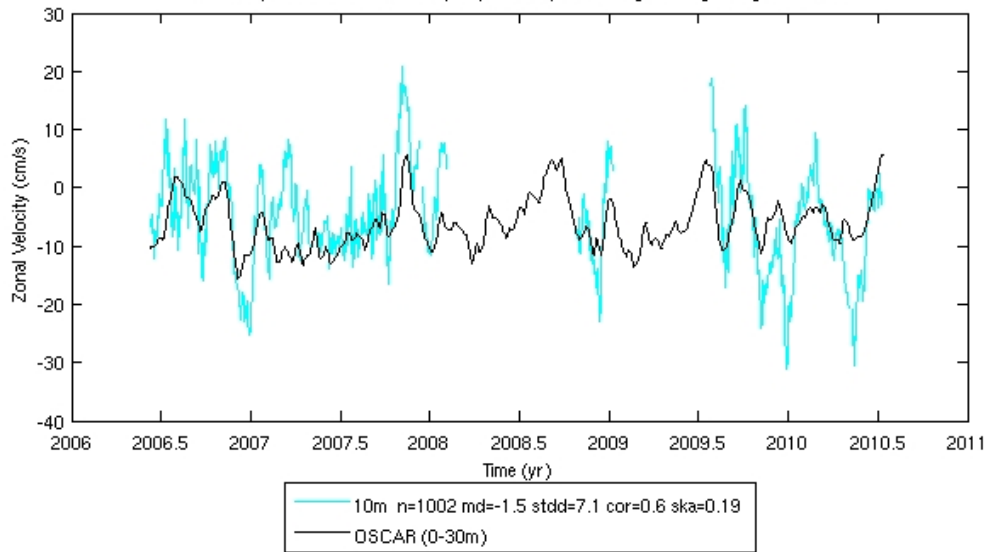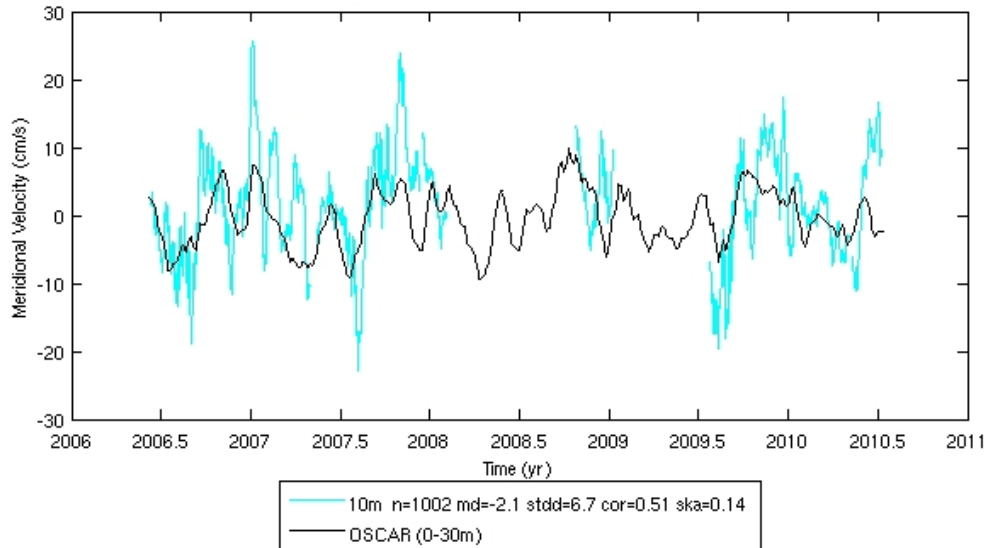
Annex B.2 - OSCAR data vs In-situ mooring data at 12ºN 23ºW. Source: ESR. Retrieved from: http://www.esr.org/~bonjean/oscar/global_validation/moorings/adcpcur12n23w_uv_5d.jpg

Annex C: Far-Field Eddies Trajectories

Far-field Eddies: 2003 - 2014
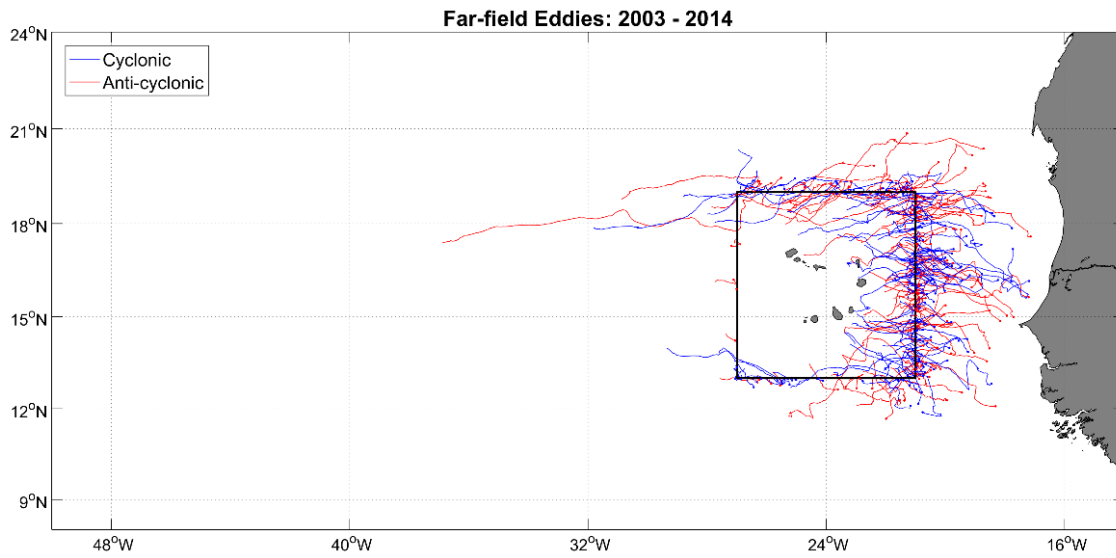
Annex C.1 – Far-field eddy trajectories: 1 day minimum lifetime.

Far-field Eddies: 2003 - 2014
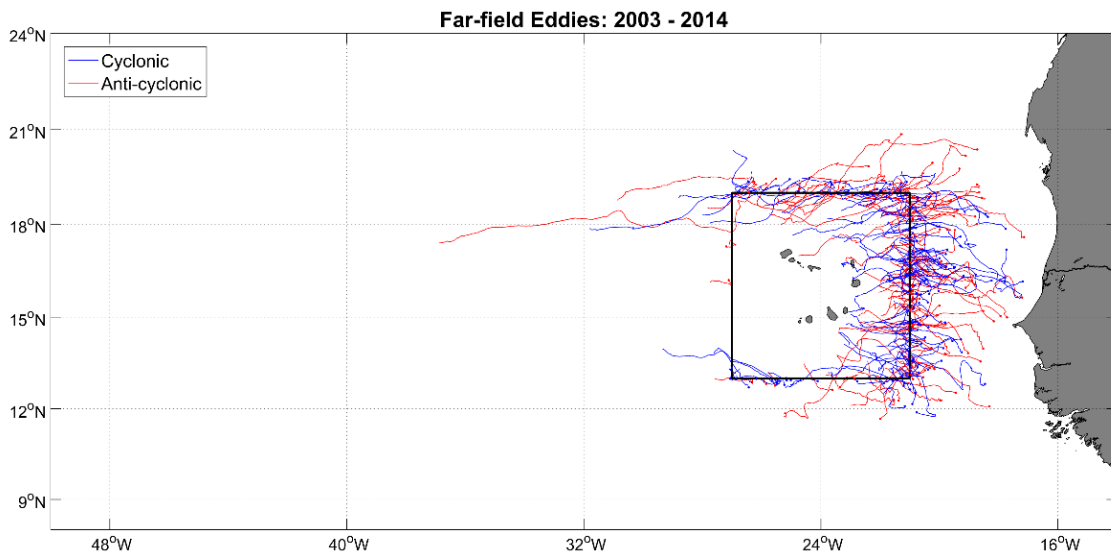
Annex C.2 – Far-field eddy trajectories: 7 days minimum lifetime.
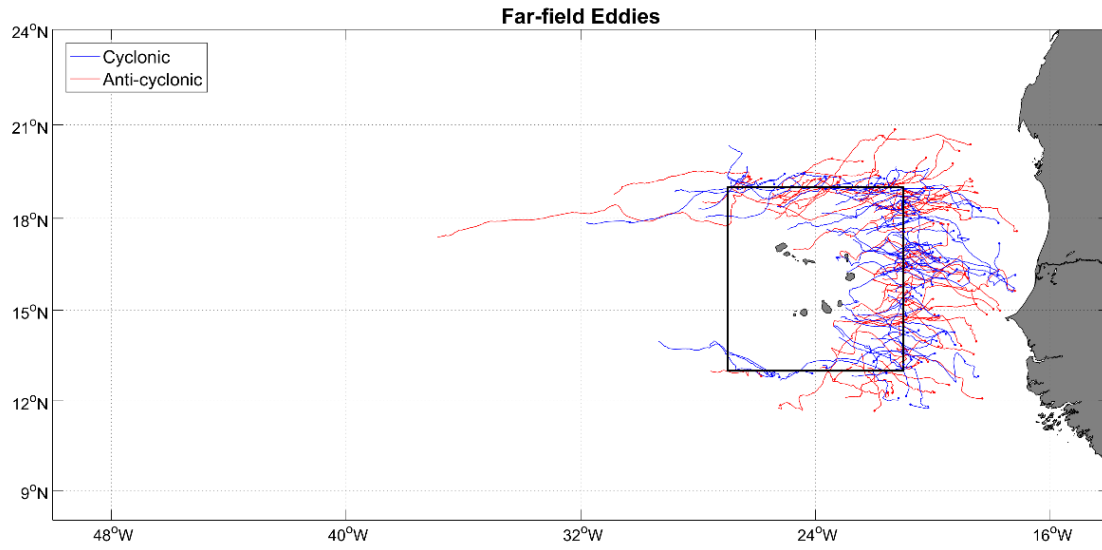
Annex C.3 – Far-field eddy trajectories: 30 days minimum lifetime.
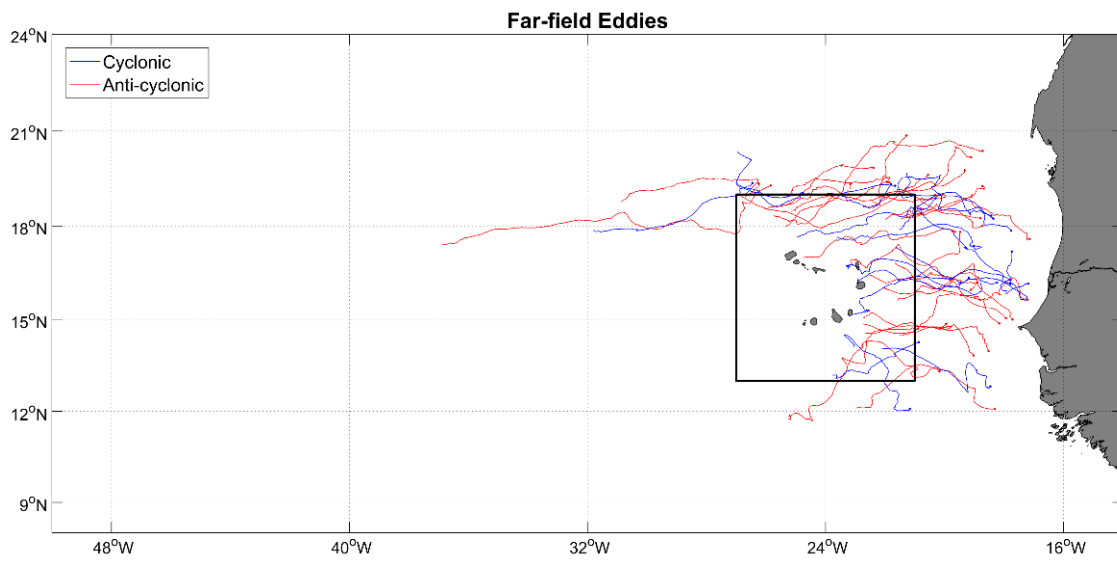
Annex C.4 – Far-field eddy trajectories: 90 days minimum lifetime.

Annex D: Near-field Eddies Trajectories
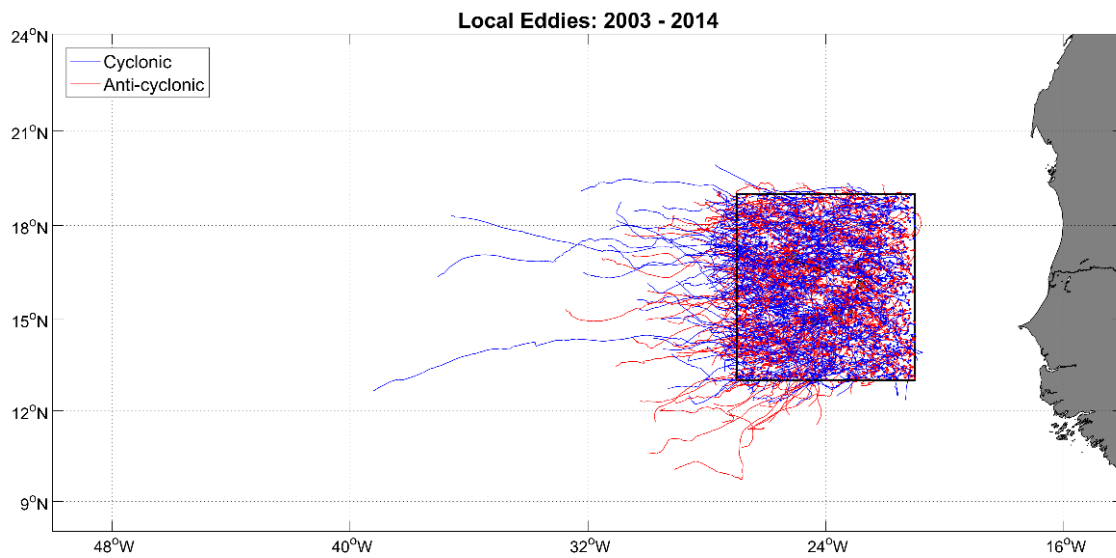
Annex D.1 - Near-field eddy trajectories: 1 day minimum lifetime.
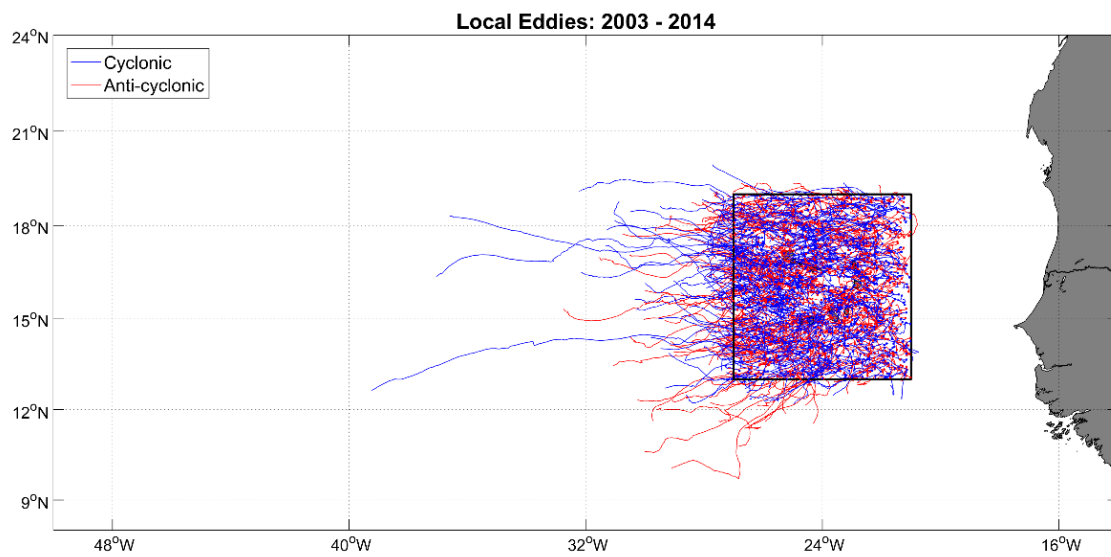
Annex D.2 – Near-field eddy trajectories: 7 days minimum lifetime.
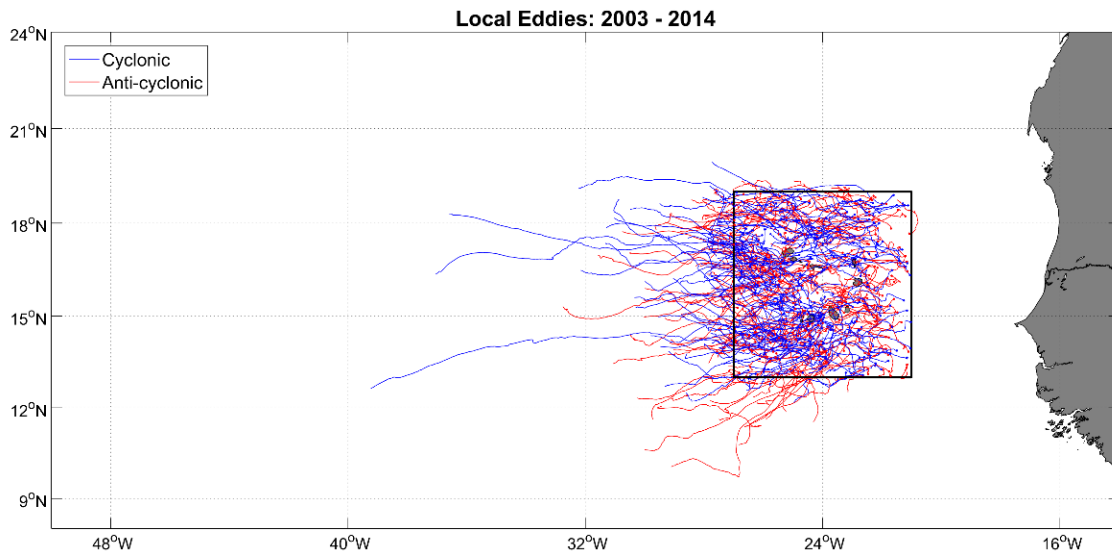
Annex D.3 – Near-field eddy trajectories: 30 days minimum lifetime.
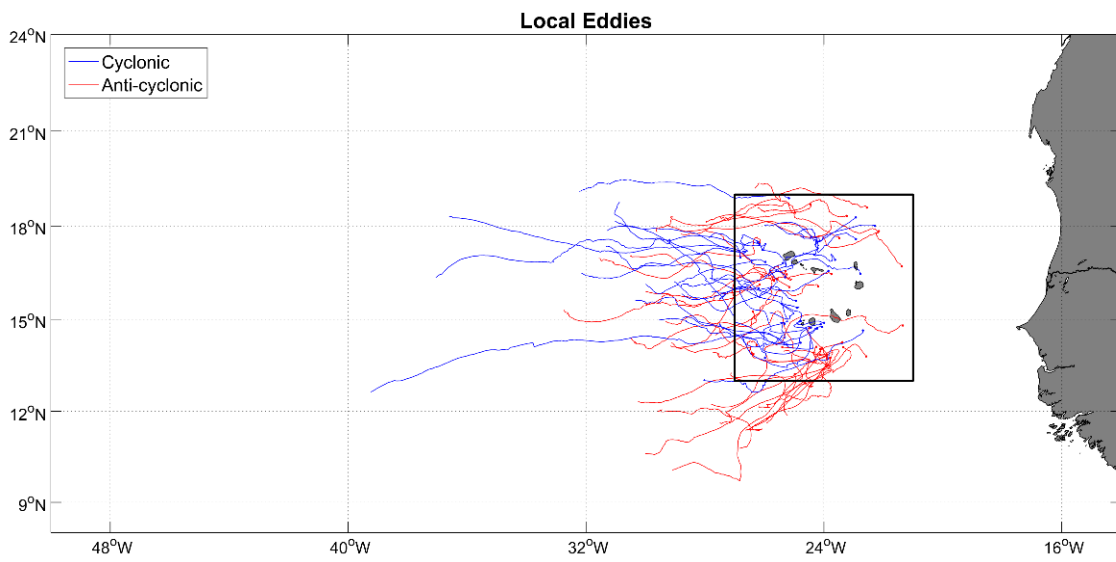
Annex D.4 – Near-field eddy trajectories: 90 days minimum lifetime.

119

Annex E: Eddy Geographical Distribution – Kinematic Properties
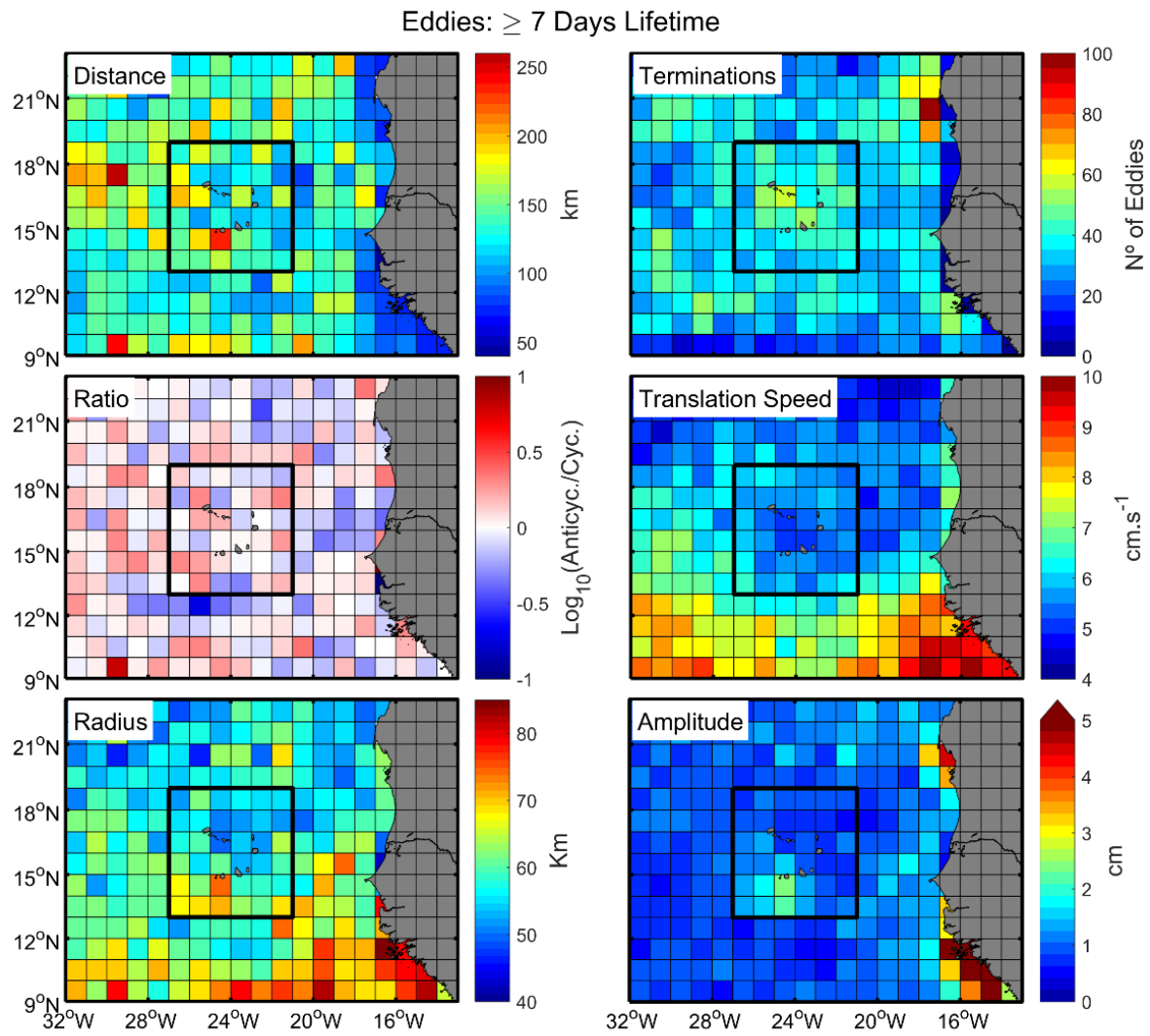
Annex E.1 – Geographical distribution of the mean eddy kinematic properties, considering medium-lived (≥ 7 days) eddies generated in every 1º × 1º box.
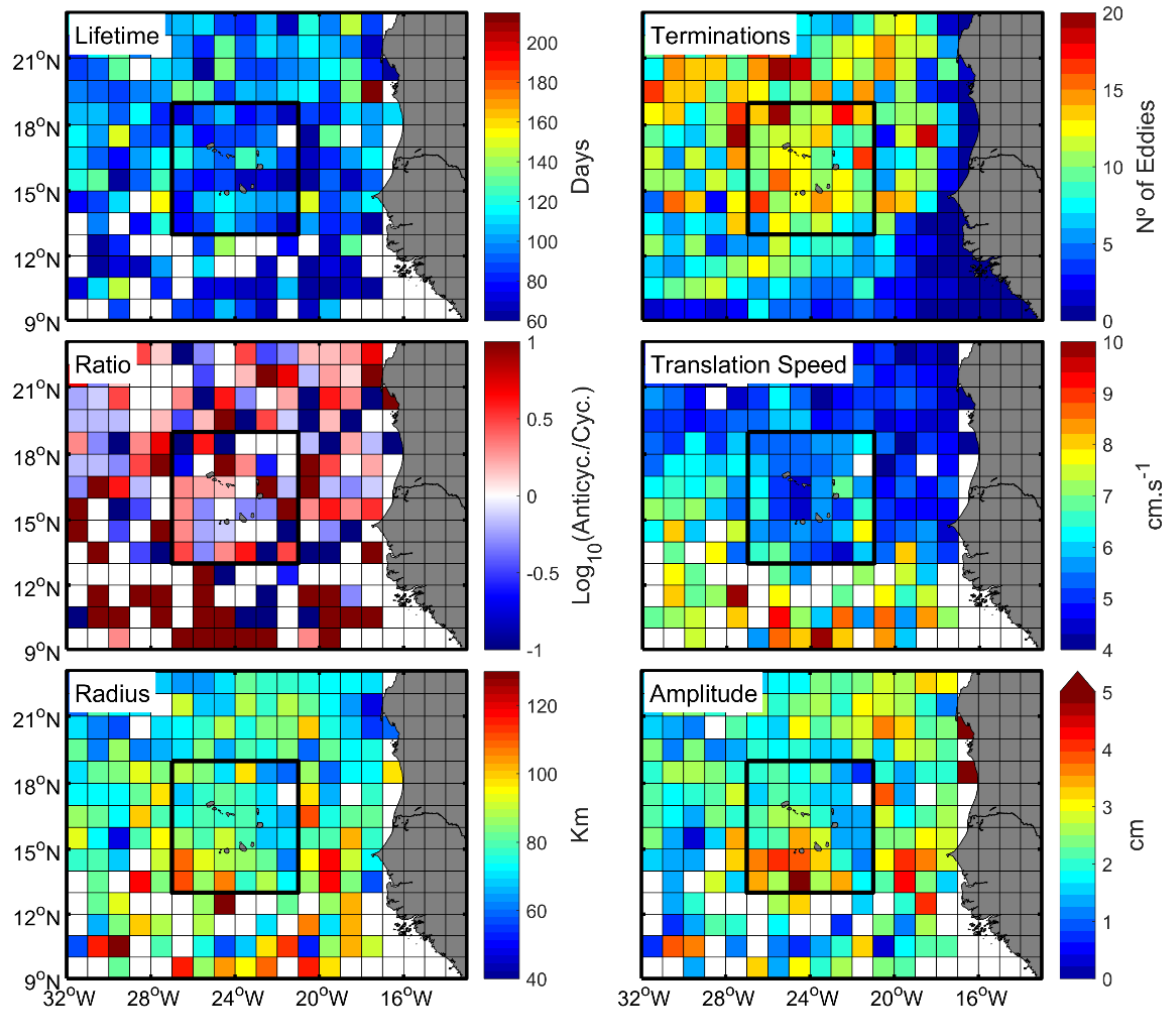
Annex E.2 – Geographical distribution of the mean eddy kinematic properties, considering medium-lived (≥ 60 days) eddies generated in every 1° × 1° box.

Annex F: Eddy Geographical Distribution – Seasonality
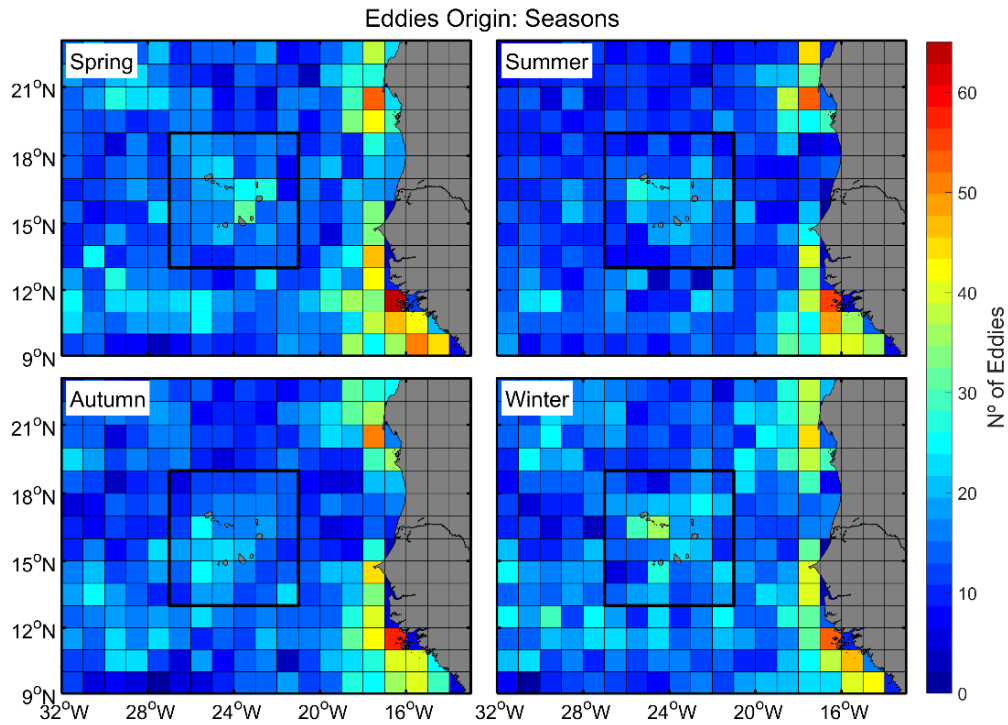
Annex F.1 – Geographical distribution of the number of medium-lived eddies ($\geq$ 1 day lifetime) generated in every $1º \times 1º$ box, filtered per boreal seasons. Black thick lines represent the CV. Eddy generation distributed along the boreal seasons.
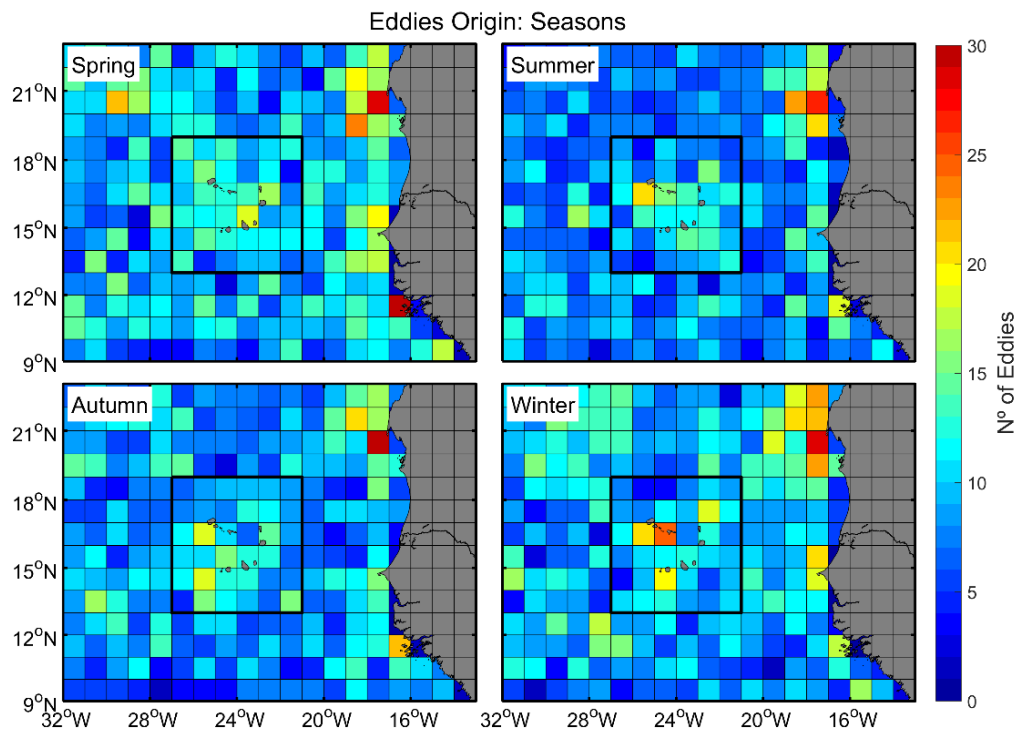

Annex F.2 – Geographical distribution of the number of medium-lived eddies ($\geq$ 7 days lifetime) generated in every $1º \times 1º$ box, filtered per boreal seasons. Black thick lines represent the CV. Eddy generation distributed along the boreal seasons.
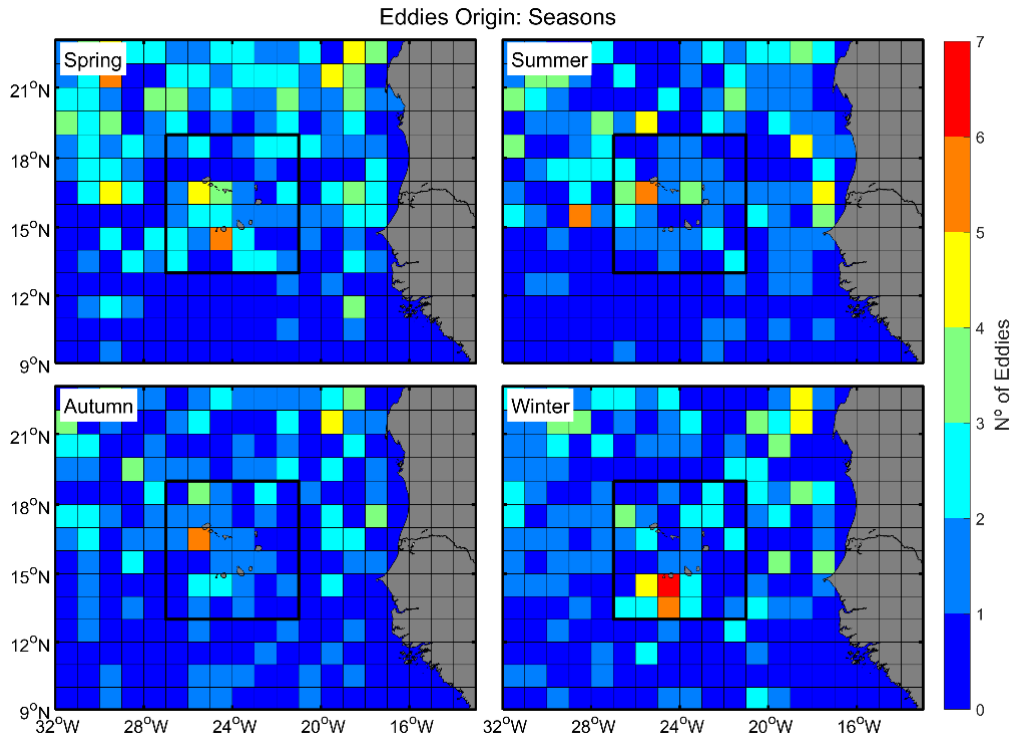
Annex F.3 – Geographical distribution of the number of medium-lived eddies (≥ 60 days lifetime) generated in every 1º × 1º box, filtered per boreal seasons. Black thick lines represent the CV. Eddy generation distributed along the boreal seasons.

Annex G: Eddy Statistics
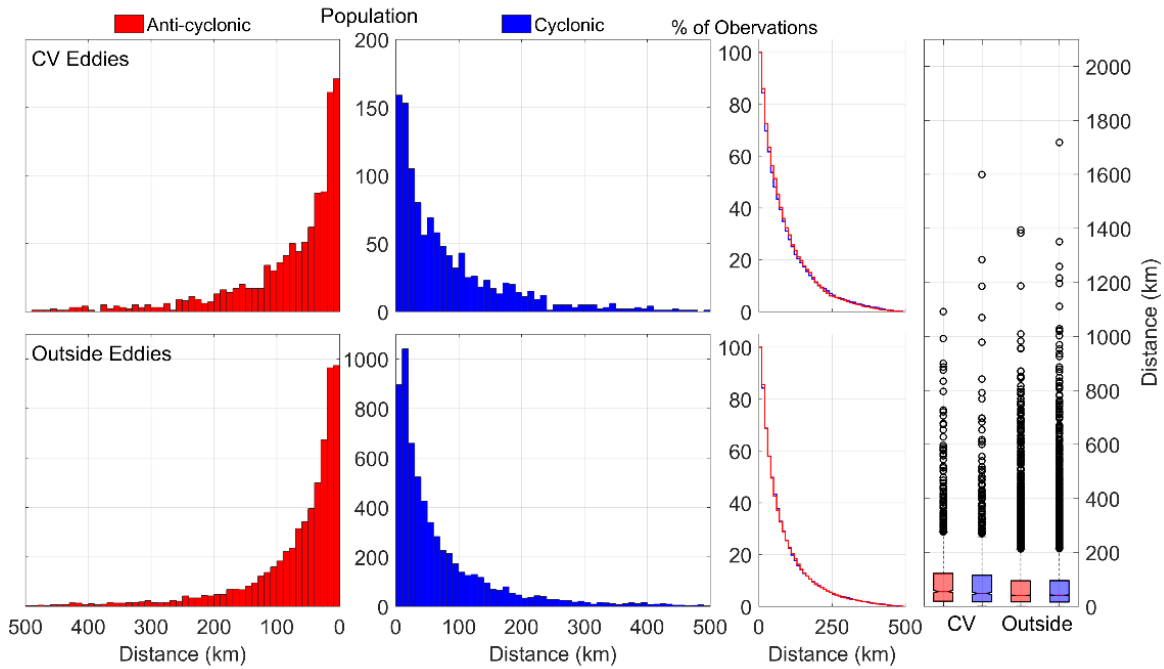
Annex G.1 – Statistical distribution for the eddies travelled distance. From left to right: Histograms, representing the number of eddies (two left panels); upper-tail cumulative histograms, representing the percentage of observations (third panel); and boxplots (forth panel).
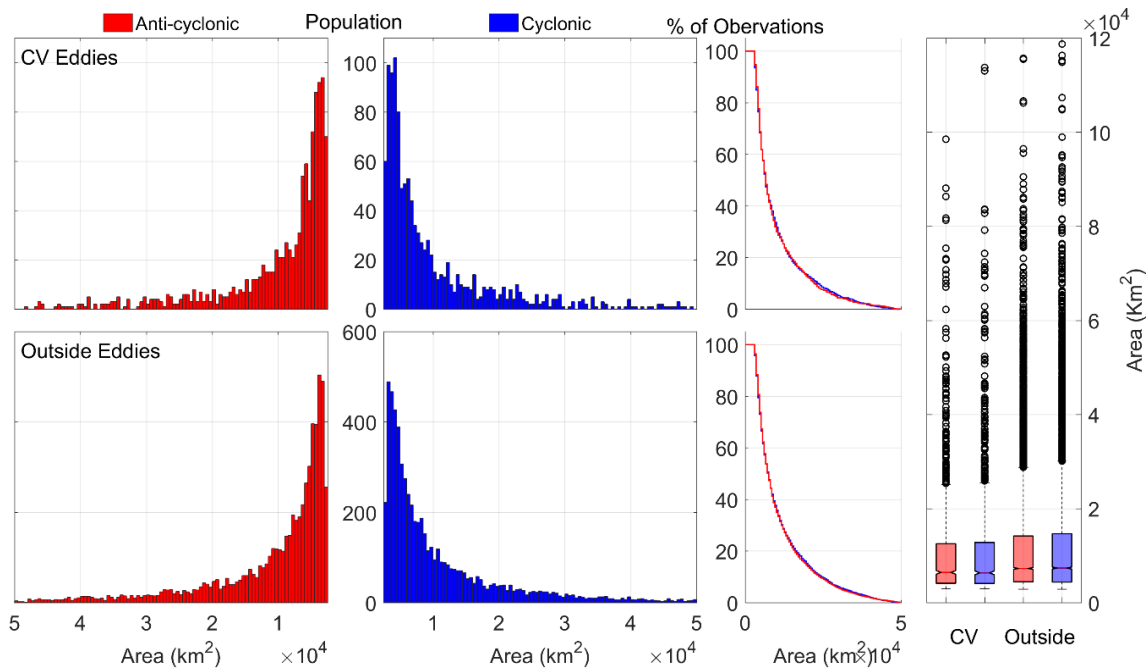

Annex G.2 – Statistical distribution for the eddies area. From left to right: Histograms, representing the number of eddies (two left panels); upper-tail cumulative histograms, representing the percentage of observations (third panel); and boxplots (forth panel).

124
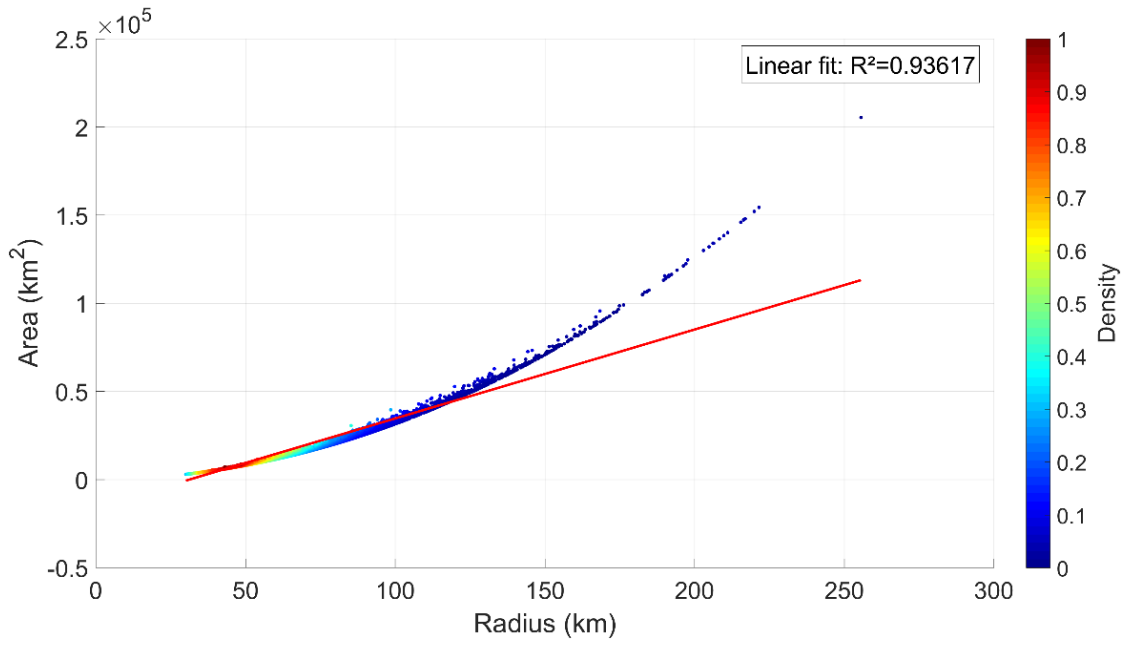
Annex G.3 – Scatter plot and linear correlation between eddy radius and area. Colour scale represents the data density.

Annex H: Far-Field Eddy Kinematic Properties

Annex H.1 – Descriptive statistics of the far-field eddy kinematic properties (≥ 1 and ≥ 60 days lifetime).

		Far-field Eddies (≥ 1 day)		Far-field Eddies (≥ 60 days)	
		Cyclonic	Anticyclonic	Cyclonic	Anticyclonic
Number of Eddies		133	130	30	44
Lifetime (days)	Max	230	286	230	286
	Min	2	2	60	60
	Mean	44.74	54.92	109.70	116.27
Travel Distance (km)	Max	1019	1394	1019	1394
	Min	3.87	11.98	174.05	203.57
	Mean	223.59	255.71	519.65	508.43
Translation Speed (cm.s^{-1})	Max	17.08	14.70	7.87	7.96
	Min	2.24	3.43	3.25	3.56
	Mean	6.04	6.00	5.64	5.11
Radius (km)	Max	148.07	131.88	147.23	126.38
	Min	30.75	30.63	58.94	36.72
	Mean	67.01	66.64	88.42	80.73
Amplitude (cm)	Max	5.76	5.24	5.76	5.09
	Min	0.09	0.05	0.71	0.26
	Mean	1.40	1.32	2.64	2.35

## Annex I: Latitudinal Averaged SLA at 21ºW Cross-section
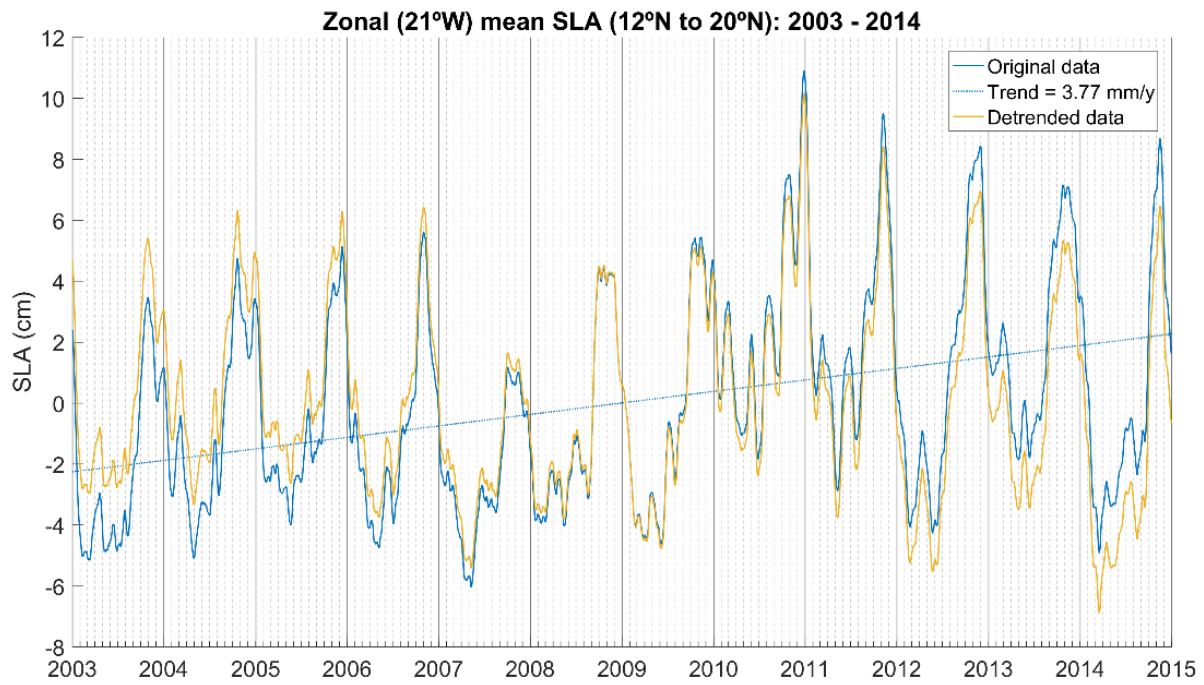
Annex I.1 – Latitudinal averaged SLA at 21ºW cross-section. Solid blue and yellow lines represent the original and detrended data, respectively. Dashed blue line represents the linear trend from the original data.

Annex J: Near-Field Eddy Kinematic Properties

Annex J.1 – Descriptive statistics of the near-field eddy kinematic properties (≥ 1 and ≥ 60 days lifetime).

		CV Eddies (≥1 day)		CV Eddies (≥60 days)	
		Cyclonic	Anticyclonic	Cyclonic	Anticyclonic
Number of Eddies		1118	1164	71	80
Lifetime (days)	Max	243	210	243	210
	Min	2	2	60	60
	Mean	19.36	19.88	97.72	94.67
Travel Distance (km)	Max	1599.33	1091.59	1599.33	1091.59
	Min	0.34	0.1	196.14	163.79
	Mean	93.85	96.11	479.52	454.18
Translation Speed (cm.s^{-1})	Max	14.23	14.83	8.25	7.88
	Min	0.2	0.05	3.11	2.92
	Mean	5.46	5.55	5.62	5.53
Radius (km)	Max	190.24	174.95	132.03	174.95
	Min	30.52	30.5	48.99	43.62
	Mean	53.84	52.95	80.36	82.50
Amplitude (cm)	Max	9.71	6.97	7.78	6.97
	Min	0.03	0.03	0.69	0.45
	Mean	0.89	0.81	2.60	2.61

**Annex K: Latitudinal Averaged SLA at 26ºW Cross-section**
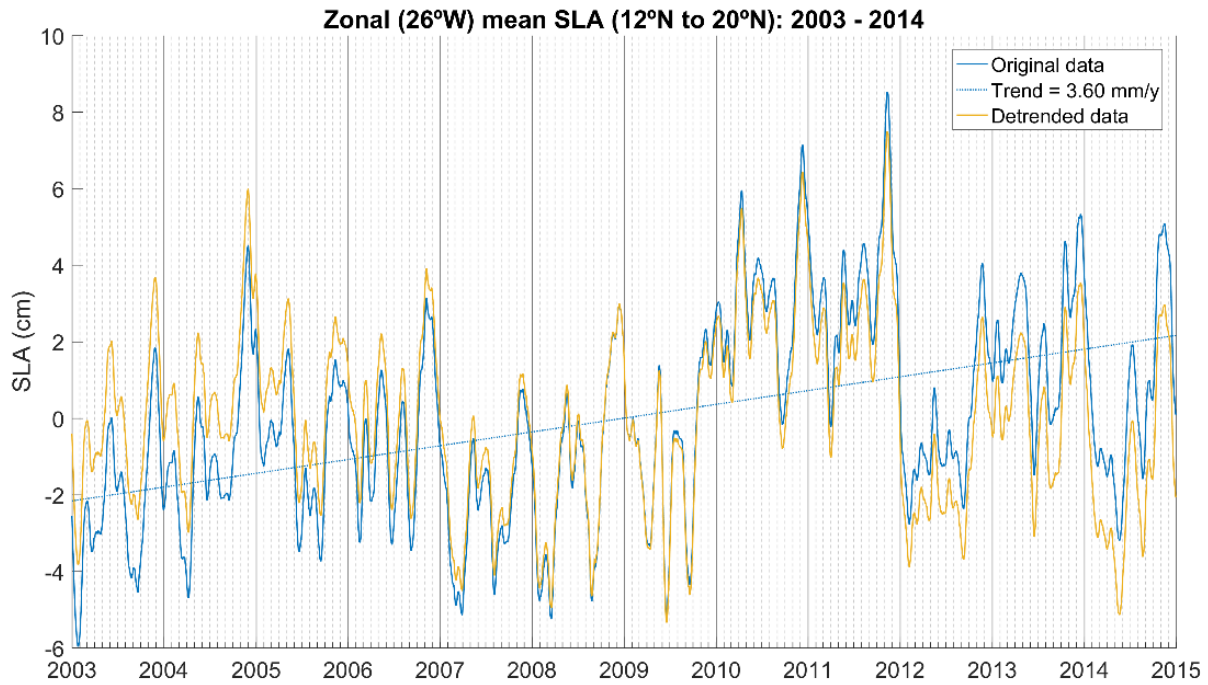
Annex K.1 – Latitudinal averaged SLA at 26ºW cross-section. Solid blue and yellow lines represent the original and detrended data, respectively. Dashed blue line represents the linear trend from the original data.

**Annex L: Meridional Averaged SLA at 13ºN Cross-section**
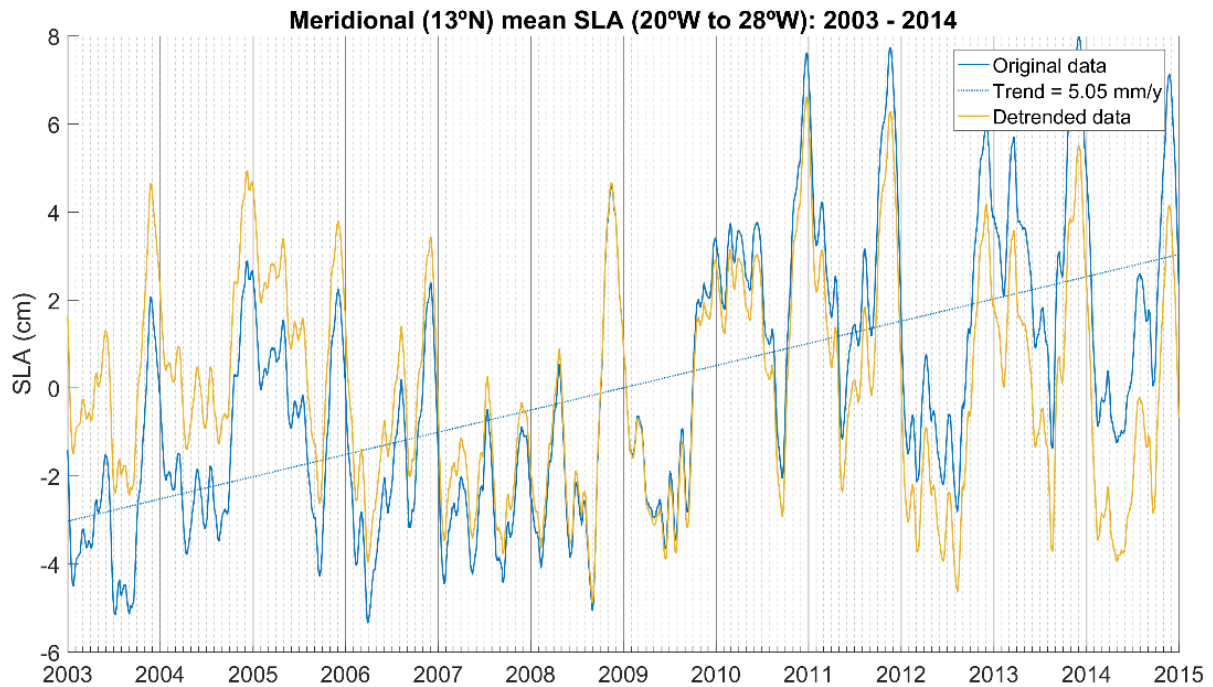
Annex L.1 – Longitudinal averaged SLA at 13ºN cross-section. Solid blue and yellow lines represent the original and detrended data, respectively. Dashed blue line represents the linear trend from the original data.

Annex M: Primary Productivity
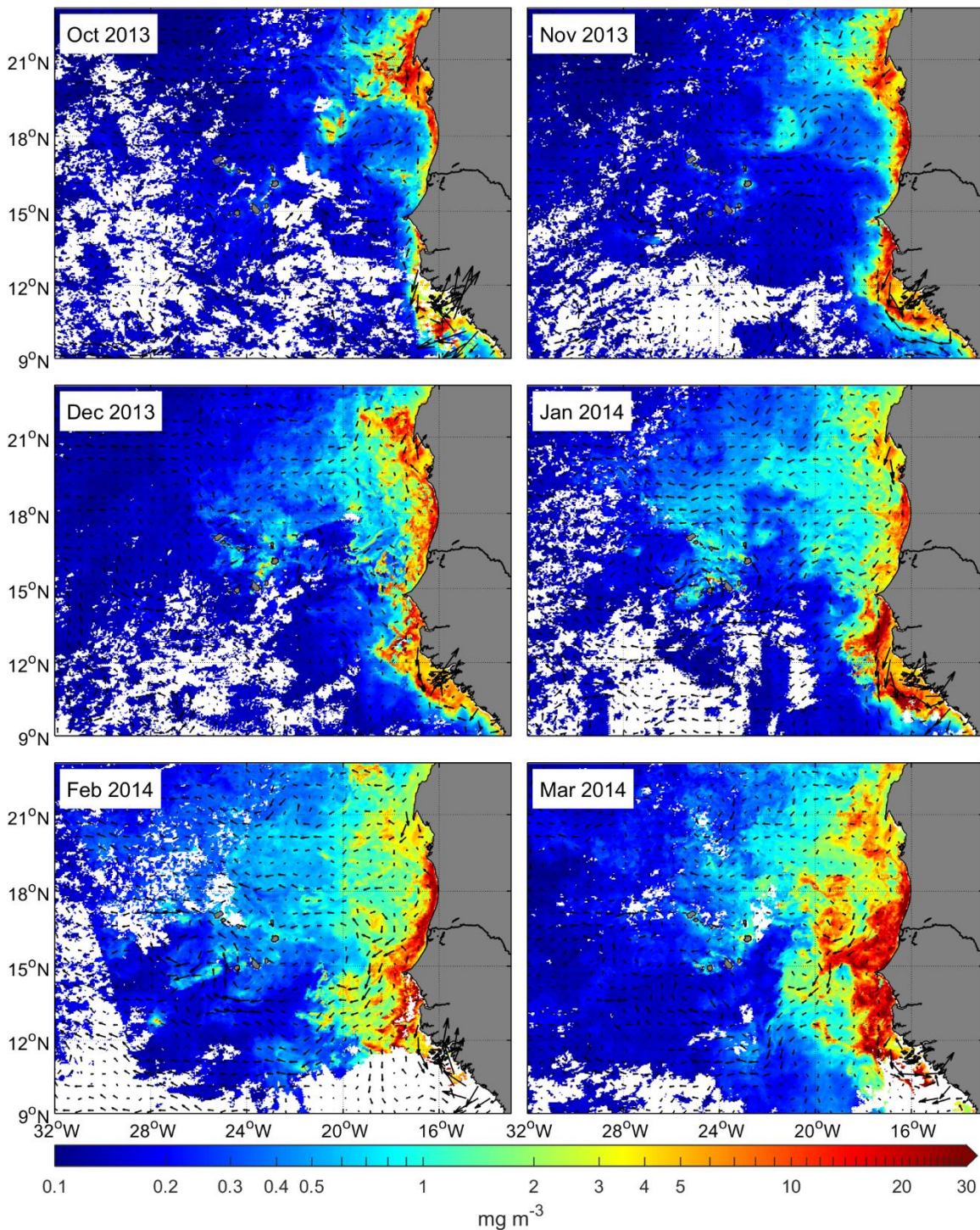
Annex M.1 – Remote enrichment scenario. Monthly Chl*a* (colour) and surface currents (quiver) means from October 2013 to March 2014.
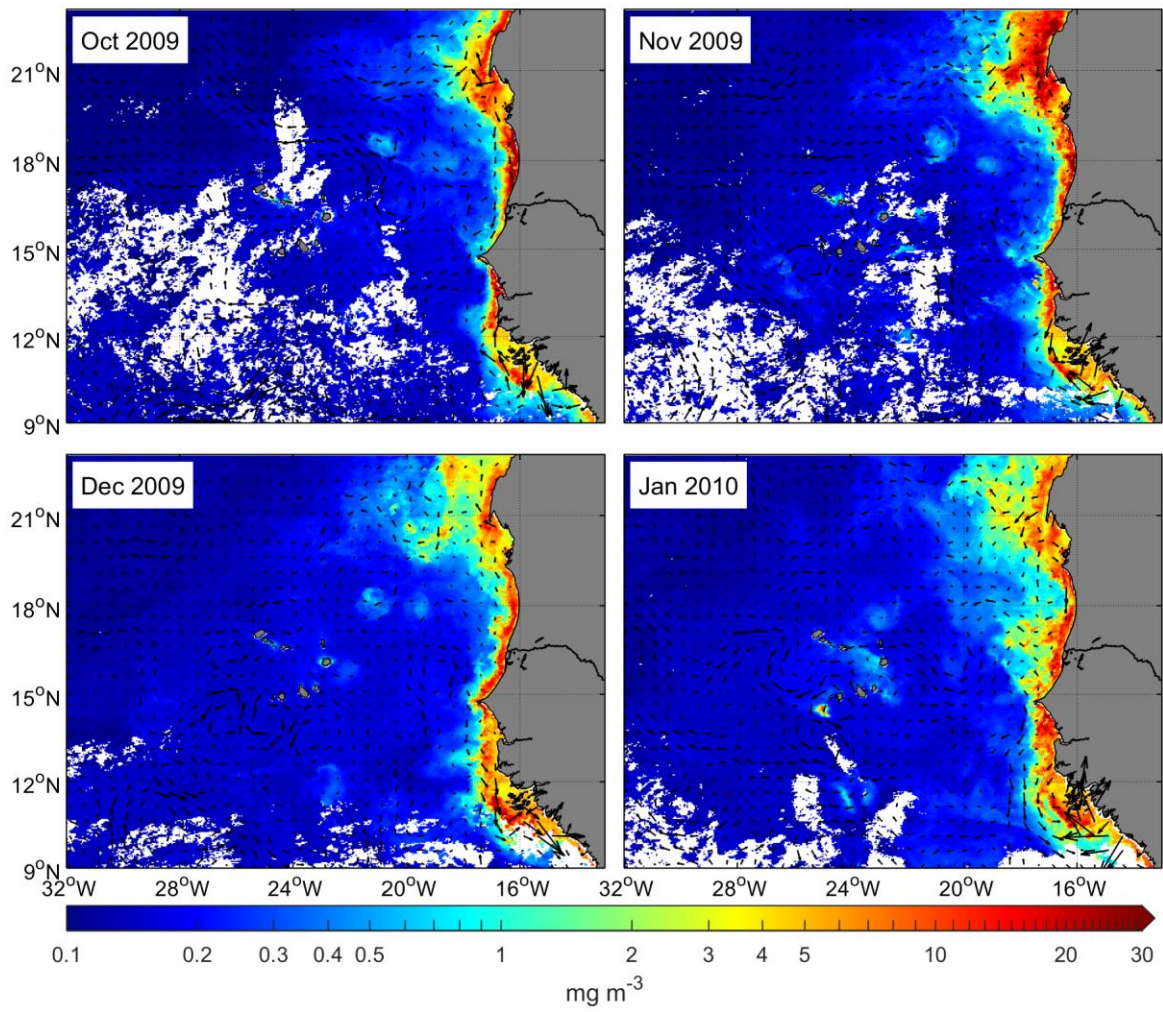
Annex M.2 – Local enrichment scenario. Monthly Chl*a* (colour) and surface currents (quiver) means from October 2009 to January 2010.

# Annex N: Eddy Swirl Speed
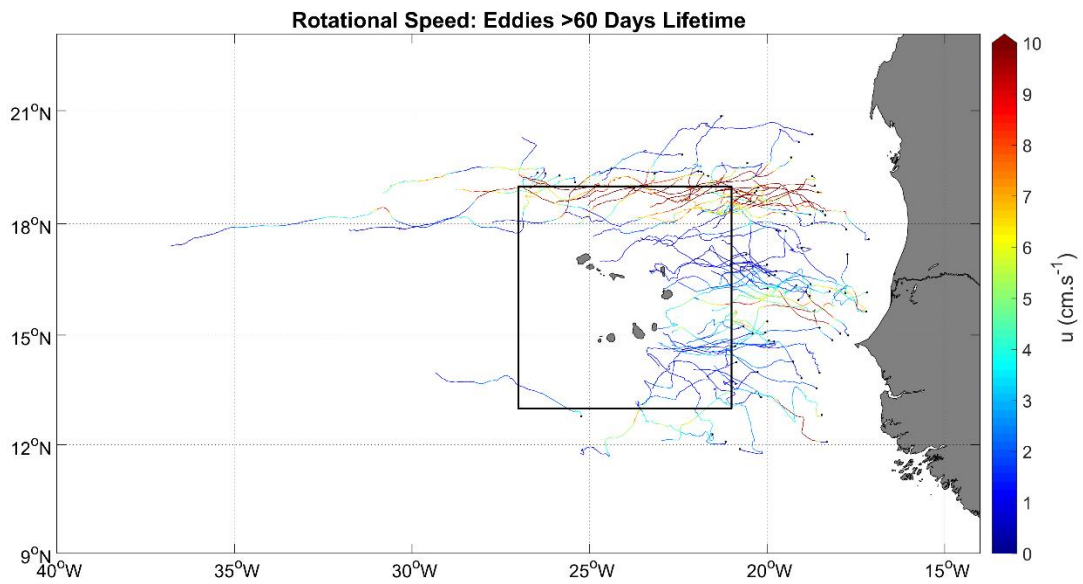
Annex N.1 – Far-field long-lived eddy swirl speed along track.
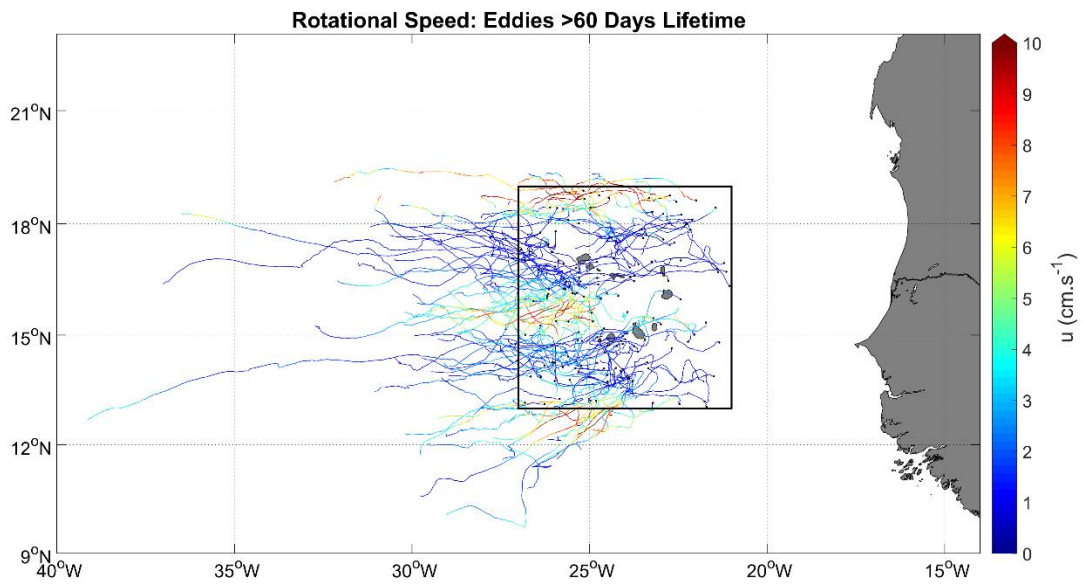
Annex N.2 – Near-field long-lived eddy swirl speed along track.

Annex O: Meridional Deflections of Long-lived CV and Outside Eddie

Considering the small number of cyclonic and anticyclonic eddies being accounted for far and near-field long-lived eddies (30 and 44 for far-field, 71 and 80 for near-field, respectively), the meridional deflection representation was computed for all long-lived eddies in the general study region (CV and Outside eddies). A total number of 330 cyclonic and 346 anticyclonic eddies were included, making the statistical analysis more robust. An identical behaviour as the ones observed for far and near-field eddies is observed, with a dominant poleward deflection (58%) and mean azimuth of 0.20ºN for cyclonic eddies, and a dominant equatorward deflection (61%) and mean azimuth of 0.33ºS for anticyclonic eddies.
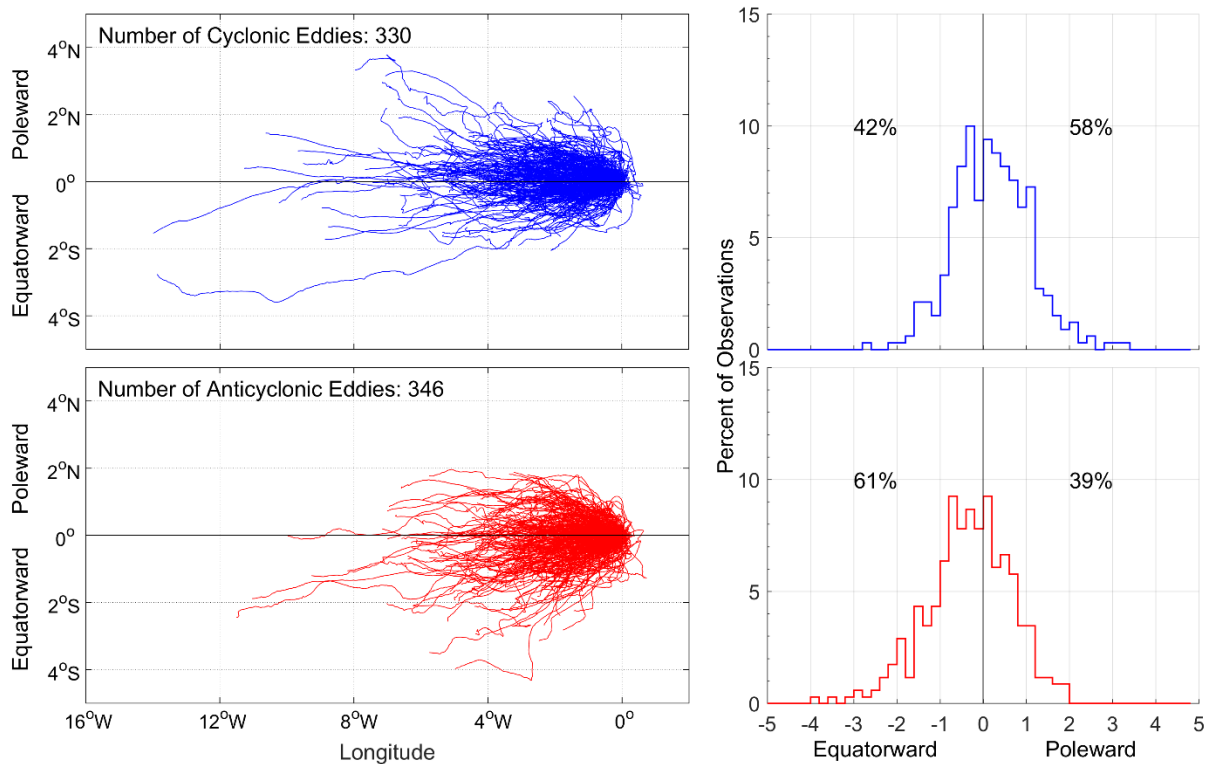
Annex O.1 – Meridional deflections of the cyclonic (upper panels) and anticyclonic (lower panels) long-lived (≥ 60 days) eddies in the general study area. The left panels show the changes in longitude and latitude relative to the initial location of each eddy. The right panels show histograms of the average azimuth of each eddy trajectory.

Annex P: Near-field Specific Case – Wind Stress Curl
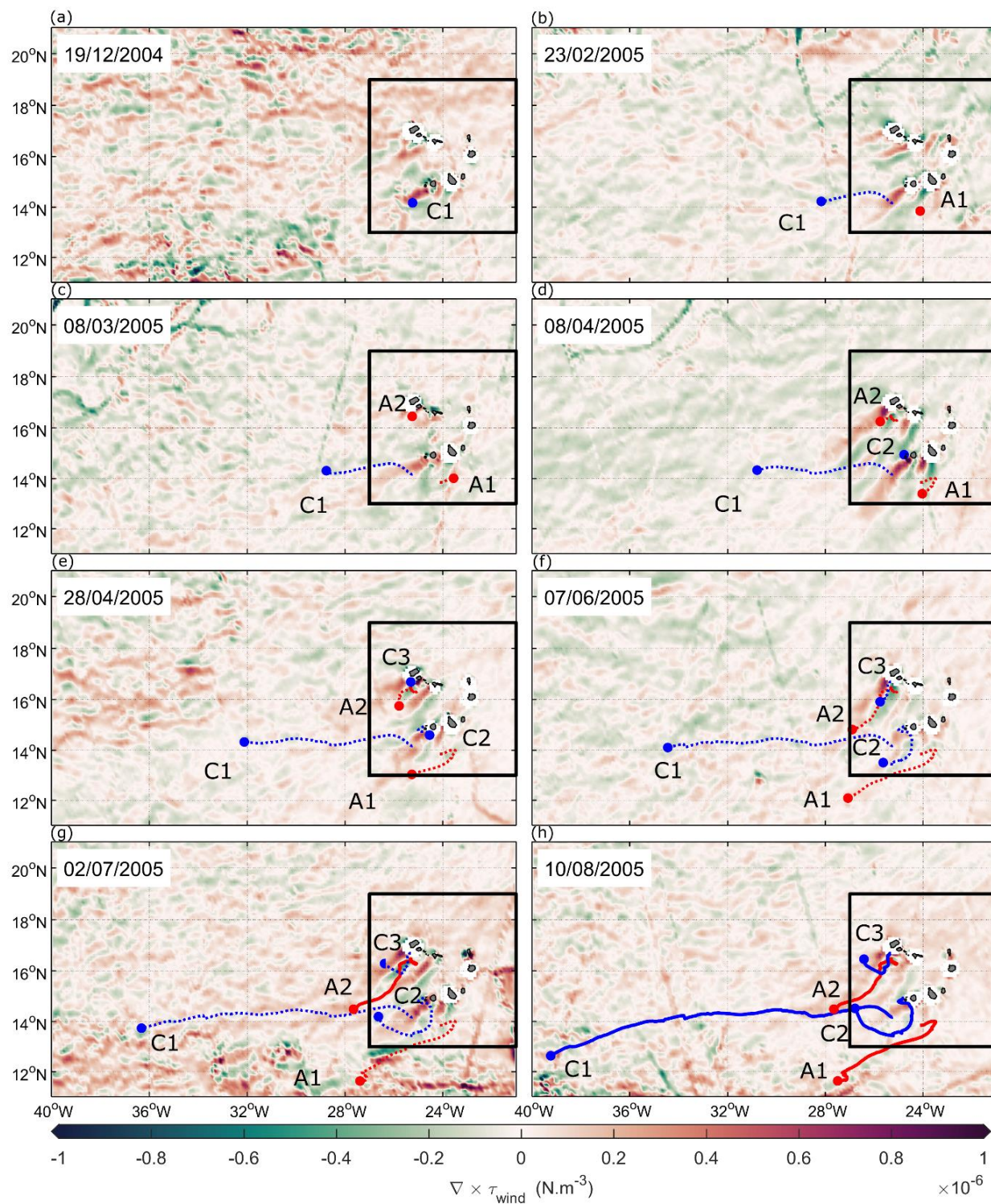
Annex P.1 – Near-field eddies evolution from 24th December 2004 to 10th August 2005, plotted against wind stress curl maps (averaged from 8 days prior to respective date). Black square represents CV area. Blue and red colours represent cyclonic and anticyclonic eddies, respectively. Doted and solid lines represent active and terminated eddy tracks, respectively.